Aalen University

Design and Analysis of a Lithography System for NIL Master Manufacturing Using Inkjet-Printed Photomasks

Master Thesis

In Partial Fulfillment for the Degree of

Master of Science

(M.Sc.)

Author:	Selina Burkert
Matriculation number:	82445
Completion period:	12/01/2021 - 03/28/2022
First auditor:	Prof. Dr. Andreas Heinrich
Second auditor:	Prof. Dr. Rainer Börret
University:	University Aalen
Major:	Advanced Systems Design (ASD)

Affidavit

I affirm that I have produced the work independently and without the use of any aids other than those specified. All passages that are taken literally or in spirit from publications or other sources are marked as such. The paper has not yet been submitted to any examination office in the same or similar form and has not yet been published.

Aalen, 03/28/2022
(Selina Burkert)

Abstract

This thesis presents the design and the analysis of a lithography system for inkjet-printed photomasks in the context of NIL stamp manufacturing. Thereby, an inkjet-printed photomask is profitable since its manufacturing process is fast. The system is based on two functional system units and a camera system, which is used to adjust the lithography system. The first functional unit does not resolve the photomask's identifiable ink dots to avoid its imaging. Subsequently, the modified image is reduced onto a substrate by the second unit. The blurred exposure results in steep slopes of the photoresist structure due to its non-linear development. According to the printing system's analysis, the lithography system's resolution must be less than 83.33 lp/mm. This requirement is met with respect to the lithography system's image-sided resolution of 22.1 lp/mm. Therefore, the lithography system improves the lithographic NIL stamp manufacturing by letting the photomask's identifiable ink dots vanish.

Table of Contents

Affidavit **I**

Abstract **II**

List of Equations **V**

List of Figures **V**

List of Tables **IX**

Glossary **XIII**

1 Introduction **1**

1.1 State of the Art 1

1.2 Goals and Research Questions 4

2 Fundamentals **5**

2.1 Optical Fundamentals 5

2.1.1 Ray Optics 6

2.1.2 Wave Optics 14

2.1.3 Abbe Theory and Resolution 19

2.1.4 Distortion 26

2.2 Conventional Lithography 28

2.2.1 Photolithography 28

2.2.2 Photomask 32

2.3 Inkjet Printing 34

2.3.1 Digital Layout and Software 34

2.3.2 Print head 35

3 Methodology **38**

3.1 Analysis of the Printing Systems 38

3.2 Setup and Analysis of the Lithography System 39

4 Experimental results **42**

4.1 Printing Systems 42

4.1.1 Canon iX6850 42

4.1.2 Dimatix 2850 50

4.1.3 Printer Comparison and Determination of the Lithography System's Resolution Limit 52

4.2 Photolithography System 53

4.2.1 Determination of the Most Optimal Macro Lens Setting . 56

4.2.2 Adjustment of the System Units 60

4.2.3 Illumination Power 78

5 Discussion **81**

5.1 Printing System 81

5.2 Photolithography System 82

6 Conclusion and Outlook **87**

Bibliography **XIX**

Appendices **XXVI**

A Visual Comparison of BK- and PGBK-Printed Structures **XXVII**

B MTF Analysis Results of the Applied Macro Lens Settings **XLII**

C WFS Measurement of the Tube Lens' Positioning **XLIX**

D Captured Spot Areas of Different Applied LED Distances **LI**

E Spot Areas Using a Kepler Illumination **LVIII**

F Illumination Check After the Movement of the Tube Lens **LXV**

G Power Measurement of Different LED Settings **LXVII**

H Look-up Table of Possible Exposure Power And Time Settings **LXIX**

List of Figures

1.1 Inkjet printed transistor 2
1.2 Applied grayscale lithography. 2
1.3 The original lithography system is based on a microscope. 3
1.4 Identifiable ink dots in the developed photoresist structure. . . . 4

2.1 Reflection on a plane mirror. 6
2.2 Reflection on a plane mirror. 7
2.3 Main parameters of a thin lens. 9
2.4 Depth of field and depth of focus 10
2.5 Angular magnification of an afocal system 10
2.6 KEPLER telescope 11
2.7 GALILEI telescope 12
2.8 Microscope's principle 13
2.9 Two-dimensional illustration of a plane wave. 14
2.10 Two-dimensional illustration of a spherical wave. 15
2.11 Two-dimensional illustration of interference. 16
2.12 Constructive interference 17
2.13 Destructive interference 17
2.14 HUYGENS principle at a diffraction grating 18
2.15 Geometrical relations of the FRAUNHOFER diffraction and the resulting diffraction pattern. 19
2.16 Visualization of a microscope's imaging which is based on ABBE's theory. 20
2.17 Geometrical correlations of a system's numerical aperture. . . . 22
2.18 MTF of two systems. 24
2.19 USAF chart 1951. 25
2.20 Contrast threshold based on RAYLEIGH criterion 26
2.21 Positive(a) and negative(b) distortion. 27
2.22 Geometrical relations of the measured distortion. 28

2.23 Basic setup of a lithography system. 30
2.24 Photolithography processes' workflow 31
2.25 Phase shifting photomask based on MoSi. 33
2.26 Basic components of a inkjet print head 35
2.27 Print heads based on thermal (a) and piezoelectric (b) actuators. . 36
2.28 Visualization of parameters which have an significant impact on the drop volume (a) and the spot size (b). 37

3.1 Extracted digital layout of the printed bars (a) and the negative bars (b). 38
3.2 Theory of the lithography system's effects on an imaged mask structure and the developed photoresist structure. 40
3.3 Setup of the lithography system based on two functional units. . 41

4.1 Structures' grid of the printed test patterns. 42
4.2 Measured bars are printed by a Canon iX6850 with BK ink (a) and PGBK ink (b). 44
4.3 Impact of the structure printing type on the resulting structure size: Printed bars (a), negative bars (b) 45
4.4 Background printed structures of 132.5 µm which are printed using a Canon iX6850 with BK ink (a) and PGBK ink (b) 46
4.5 Background printed structures of a 67.5 µm reference structure size based on BK ink (a) and PGBK ink (b). 47
4.6 Analysis of the Canon iX6850 printed edges which are based on BK ink (a) and PGBK ink (b). 48
4.7 Images of PGBK printed structures with a bar size of 97.5 µm (negative structures) (a), 97.5 µm (printed bars) and 150 µm (printed bars) (c). 49
4.8 Measured bar sizes of the DMP 2850 printed structures using the Dimatix test ink. 51
4.9 Analysis of the DMP 2850 printed edges. 52
4.10 Normal distribution 53
4.11 Scaled and labeled setup of the lithography system. 55
4.12 Experimental setup the macro lens' analysis with respect to resolution and FOV. 56

4.13 Results of the macro lens' analysis with respect to the FOV and the resolution of the respective macro lens' setting. 57
4.14 Setup of the distortion measurement (a) and the automatized evaluation (b). 58
4.15 Analysis of the measured radial distortion with respect to the macro lens' setting. 58
4.16 Comparison all pre-chosen macro lens settings to evaluate the most optimal setting for the lithography system's setup. 60
4.17 Visualization of the macro lens focusing on the mask plane. . . . 60
4.18 Visualization of the tube lens adjustment. 61
4.19 Visualization of the illumination adjustment by determining the LED chip position: principle illustration (a) and photography of the setup (b). 62
4.20 Visualization of the precise illumination adjustment by moving the LED chip. 63
4.21 The illumination homogeneity in the substrate plane is not acceptable due to the imaged LED chip (a). Although, the light source is imaged in the microscope lens' aperture plane (b). . . . 64
4.22 The distance between the mask plane and the LED is increased in 5 mm steps to analyze the intensity distribution in the substrate plane. 65
4.23 The analysis of the illumination homogeneity and the usable area is based on the relative intensity (a) and the increasing distance from the LED housing to the mask plane (b). 66
4.24 The lithography system is modified using a KEPLER telescope to improve the illumination in the substrate plane. 67
4.25 The analysis of the illumination homogeneity and the usable area using a KEPLER telescope is based on the relative intensity (a) and the FWHM of the fitted GAUSSIAN intensity distribution (b). 68
4.26 In the assembly of the lithography and camera systems, the lithography system's image plane and the camera system's focal plane are positioned at the same location. 69

4.27 The assembly of the vertical camera system and the horizontal lithography system is conducted by moving the tube lens. 70
4.28 Analysis setup of the camera system's magnification and resolution. 71
4.29 Captured image of USAF chart which is positioned in the substrate plane. 72
4.30 Analysis setup of the lithography system's magnification and resolution. 72
4.31 MTF analysis of the total system using imaged USAF charts as displayed in (a) and the fitted MTF graphs of (b). 74
4.32 Visualization of the lithography system's resulting magnification which is based on the macro lens magnification m_{L1} (a) and the microscope lens' magnification m_{L2} (b). 75
4.33 MTF analysis of the macro lens using imaged USAF charts as displayed in (a) and the fitted MTF graphs of (b). 76
4.34 Setup of the lithography system by applying the printed photomask in the mask plane and capturing the image of the substrate plane. 77
4.35 Captured images of the substrate plane which display the mage of the printed photomask. 78
4.36 Lithography system's setup of the power measurement 79
4.37 The exposure power under different conditions is measured by a power meter. 80

5.1 The minimal structure size is limited by the ink dot diameter and the resulting edge inaccuracy. 82
5.2 The focal offset Δf in the substrate plane is calculated to quantify the system error. 83
5.3 The magnification factor of the microscope lens is defined by the tube lens' focal length and the microscope lens' assumed focal length. 84
5.4 KÖHLER integrators are based on two lens arrays. 86

6.1 Theory of the lithography system's effects on an imaged grayscale mask structure and the developed photoresist structure. 89

List of Tables

4.1 Comparison of the printing systems' analysis results. 52
4.2 Preset optem settings based on resolution, FOV, and distortion. . 59

List of Equations

2.1.1 Speed of electromagnetic waves in vacuum 5
2.1.2 Speed of electromagnetic waves in a medium 5
2.1.3 Refractive index 6
2.1.4 Incidents and reflection angle 6
2.1.5 Reflectivity 6
2.1.6 Optical path length 7
2.1.7 Total optical path length OPL_t 7
2.1.8 FERMAT's principle 8
2.1.9 Applied FERMAT's principle on OPL_t 8
2.1.10 Geometrical relation of the incident and refractive path 8
2.1.11 SNELL's law 8
2.1.12 Lens equation 9
2.1.13 Transversal magnification factor 9
2.1.14 Axial magnification factor 10
2.1.15 Angular magnification 11
2.1.16 Angular magnification of KEPLER telescope 12
2.1.17 Angular magnification of GALILEI telescope 13
2.1.18 Angular magnification of a microscope 13
2.1.19 Wave equation 14
2.1.20 Plane wave equation 14
2.1.21 Phase of a plane wave 15
2.1.22 Spherical wave equation 15
2.1.23 Superposition of waves 16
2.1.24 Interference of two waves 16
2.1.25 Measured intensity of a wave 16
2.1.26 Constructive interference of two waves 17
2.1.27 Destructive interference of two waves 17
2.1.28 Difference between the intensity maxima of a diffraction pattern 19
2.1.29 Image in the FOURIER plane 20

2.1.30 System-affected image in the FOURIER plane 21
2.1.31 System-affected image on the detector 21
2.1.32 Minimal resolved structure size using a coherent illumination in the microscope. 21
2.1.33 Minimal resolved structure size using an incoherent or angled illumination in the microscope. 22
2.1.34 Numerical aperture 22
2.1.35 Modualtion Transfer Function based on the OTF and the PTF . 23
2.1.36 Contrast 23
2.1.37 MTF based on the contrast ratio of object and image 23
2.1.38 Cut off frequency of a ideal MTF 24
2.1.39 Ideal MTF as a function of the spatial frequency 24
2.1.40 MTF based on the subsystem's MTF 24
2.1.41 The spatial resolution based on the RAYLEIGH criterion 26
2.1.42 Absolute radial distortion 28
2.2.1 Lithography systems' minimal feature size 30
2.2.2 Lithography systems' depth of focus 31
2.3.1 Drop volume of an inkjet drop 36
4.1.1 Determination of the lithography system's resolution limit . . 53
4.1.2 Determination of the lithography system's resolution limit . . 53
4.2.1 Determination of the WFS's RMS error 61
4.2.2 STREHL criteria 65
4.2.3 Magnification factor of the camera system 71
4.2.4 Magnification factor of the lithography system 73
4.2.5 Resulting FOV 73
4.2.6 Magnification factor of the lithography system's macro lens . . 75
4.2.7 Magnification factor of the lithography system's microscope lens 76
4.2.8 Imaged edge inaccuracy in the camera sensor plane 77
4.2.9 Calculation of the required exposure time due to the set relative LED intensity 80
5.2.1 Calculation of the microscope lens' focal length to determine the focal offset 83
5.2.2 Calculation of the microscopes focal difference 83

5.2.3 Calculation of the microscopes focal length 84
5.2.4 Calculation of the required focal length 85

Glossary

B | C | D | E | F | M | N | O | P | R | S | T | U | W

B

BK Black Ink
BMP Windows Bitmap

C

CMYK Cyan, Magenta, Yellow, Key Black color code

D

DMP Dimatix Material Printer
DPI Dots per Inch

E

EBL Electron Beam Lithography
EUV Extreme Ultraviolet

F

FIB Focused Ion Beam
FOV Field of View
FWHM Full Width Half Maximum

M

MTF Modulation Transfer Function

N

NA Numerical Aperture
NIL Nanoimprint Lithography

O

OPD Optical Path Difference
OPL Optical Path Length
OTF Complex Optical Transfer Function

P

PET Polyethylenterephthalat
PGBK Pigment-added Black Ink
PNG Portable Network Graphics
PTF Phase Transfer Function
PWM Pulse Width Modulation

R

RIP Raster Image Process
RMS Root Mean Square

S

SVG Scalable Vector Graphics

T

TIFF Tagged Image File Format

U

UV Ultra Violet

W

WFS Wavefront Sensor
WLI White Light Interferometer

Symbols

Symbol	Unit	Description
a	m	Object distance
a'	m	Image distance
α	rad	Incidence angle
α_m	rad	Diffraction angle of order m
α'	rad	Reflection angle, exit angle
β	rad	Refractive angle
β'		Transversal magnification factor
β'^2		Axial magnification factor
c_0	$\frac{m}{s}$	Light speed
c_m	$\frac{m}{s}$	Light speed in a medium m
C		Contrast
d	m	Distance
D	m	Object-sided distance of the marginal rays
D'	m	Image-sided distance of the marginal rays
D_i	m	Distortion of point i
d_m	m	Distance between diffraction orders
E	$\frac{V}{m}$	Electric field
e	$\frac{V}{m}$	Complex electric field
ε_0	$\frac{A\,s}{V\,m}$	Electric constant
ε_r	$\frac{A\,s}{V\,m}$	Relative electric constant
f	m	Object-sided focal length
F	m	Object-sided focal point
f'	m	Image-sided focal length
F'	m	Image-sided focal point
F_s	m	Surface tension's fore
F_p	m	Penetration force

Symbol	Unit	Description
f_w	m	Working distance
F_w	m	Wetting fore
g	m	Grating constant
γ	rad	contact angle
Γ		Angular magnification factor
I	$\frac{W}{m^2}$	Intensity
$I_{t,c}$	m	Total inaccuracy
$\vec{k}$	$\frac{1}{m}$	Wave vector
k_i		Application factor
l	m	Length
λ	m	Wavelength
m		Magnification factor
μ_0	$\frac{N}{A^{-2}}$	Magnetic constant
μ_r	$\frac{N}{A^{-2}}$	Relative magnetic constant
n_m		Refractive index of a medium m
n_{px}		Number of pixels
ν	$\frac{1}{m}$	Spatial frequencies
ω	$\frac{1}{s}$	Wave frequency
ϕ_0	$\frac{kg}{m^3}$	Density
$\vec{r}$	m	Position vector
R		Reflectivity
R_i	m	Distance of point i to the center
r_p	$\frac{1}{m}$	Resolution
ρ	m	Position vector
σ	rad	Incident angle of the chief ray
σ'	rad	Refractive angle of the chief ray
S	m	Bar size
s_m	m	Metric path length in a medium m
t	s	Time
V	m^3	Drop volume
y	m	Object height
y'	m	Image height

1 Introduction

Technical applications, such as augmented reality, are in continuous development and integrated increasingly by people into their living environment [43]. Consequently, technologies such as integrated photonics, waveguides, or diffraction elements for holography are becoming increasingly complex [22], [47], [68]. Due to this complexity the structure density increases. It is required that the optical structures can be precisely manufactured [73]. Furthermore, the manufacturing time of optical structures should be decreased in response to the increasing demand [43]. Nanoimprint Lithography (NIL) is one possible replication process to fulfill these requirements. Hereby, a master structure determines the structure of the optical components and can be replicated several times [40], [7], [32]. Commonly, the NIL master structures are written into a silicon (Si)-substrate, using Focused Ion Beam (FIB) Lithography, Electron Beam Lithography (EBL) or photolithography [29]. In this research, an individual lithography system is set up to optimize a NIL master manufacturing process using an inkjet photomask.

1.1 State of the Art

Inkjet printing is a common technique in additive manufacturing processes of biological [24], optical [50] and electronic devices [19], since the manufacturing is individual and precise. Negative structures below a minimum line width of 10 to 30 µm can be printed using a Dimatix Material Printer (DMP) [19], [46]. According to [19], a transistor channel size between source and drain of 1 µm is realized by a DMP 2831 with a 15 µm drop spacing as shown in Figure 1.1. The transistor and its gate *G*, source *S*, and drain *D* are imaged in Figure 1.1 (a). The respective schematic cross section in Figure 1.1 (b) specifies the channel size between source and drain.

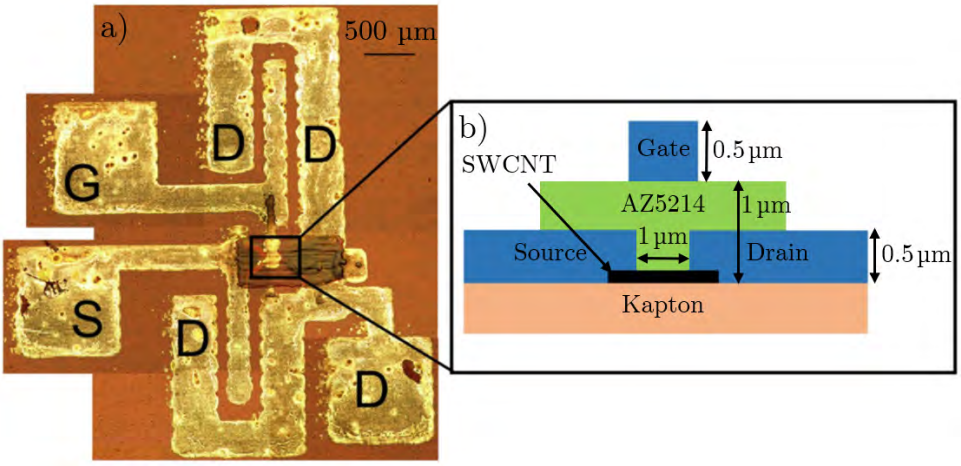

Figure 1.1: The inkjet transistor is printed by a DMP 2831 with a nanoparticle silver solution. The transistor is based on a gate electrode *G*, a source electrode *S*, and a drain electrode *D* (a). The slice in (b) shows the channel between the source and the drain which have a size of 1 µm. [19]

In general, the printing speed of $1.5 \cdot 10^{-1}$ m/s at 10 kHz jetting frequency and 15 µm drop spacing is much faster than the writing speed of FIB Lithography or EBL which are up to 10^6 times slower [15]. Furthermore, grayscale lithography can be applied to realize free-form structures in the photoresist substrate [67]. A multi-level exposure intensity can be applied onto the photoresist's surface via a printed photomask. The applied exposure intensity determines the development depth as shown in Figure 1.2. The digital grayscale mask layout in (a), which is printed on the used photomask, defines the photoresist structure (b). The photoresist structure is measured by a White Light Interferometer (WLI). The respective structure height is plotted in (c). [5], [10]

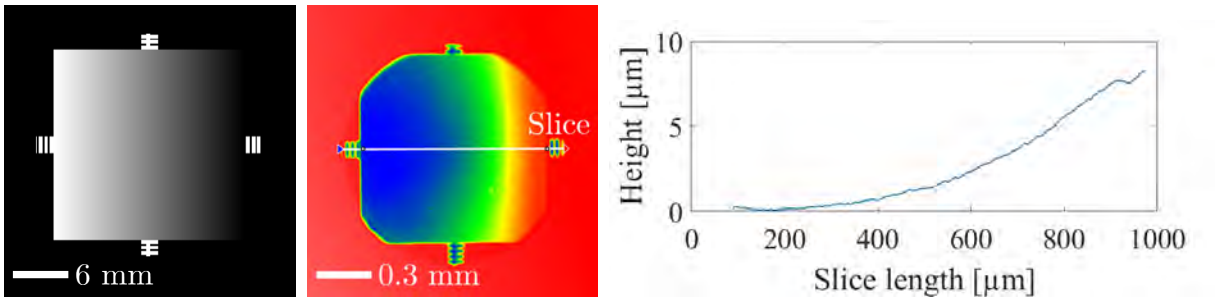

(a) (b) (c)

Figure 1.2: The digital layout (a) defines the ink distribution on the inkjet grayscale photomask. The development height of the photoresist structure (b) depends on the mask-transmitted exposure intensity. The respective slice of the photoresist structure is shown in (c). [5]

In previous experiments, photolithographic NIL master manufacturing processes were executed using inkjet-printed photomasks. The resolution of the applied photomasks was between 5.52 lp/mm and 6.62 lp/mm. They were printed by a commercial high Dots Per Inch (DPI) printer (Canon iX6850, 9600x2400 DPI). In these experiments, a photolithography system based on a Zeiss Axioskop 50 was used for the NIL master manufacturing. As imaged in Figure 1.3, the mask is located perpendicular to a UV LED. The displayed LED and mask holder is mounted on a c-mount adapter on top of the microscope. During the exposure, the mask is captured by the microscope's tube lens and a Zeiss EC Plan-NEOFLUAR lens. The mask structure is reduced by a magnification factor of 0.05 and imaged onto the substrate plane. [6]

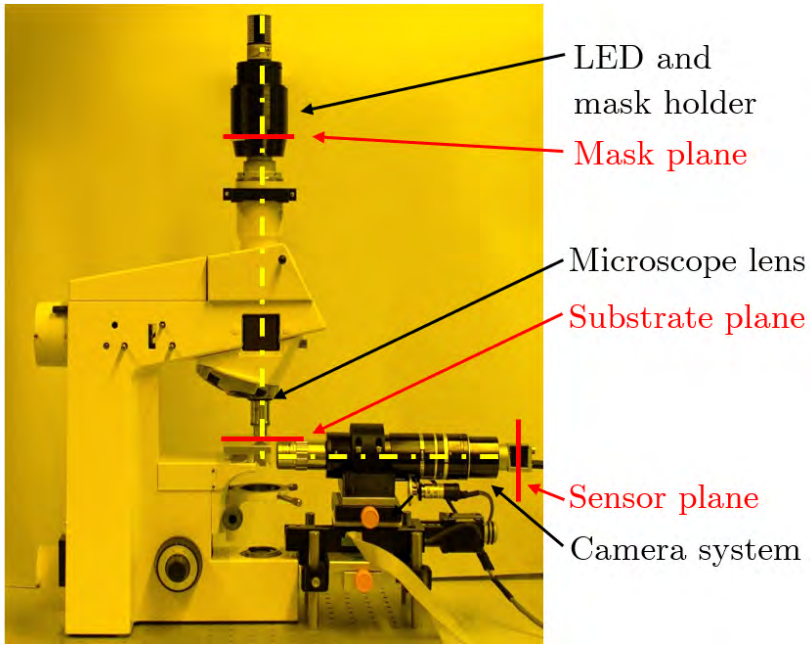

Figure 1.3: The original lithography system is based on a microscope, a LED and mask holder, as well as a camera system. The mask plane is captured by the microscope lens and is imaged onto the substrate plane. The lithography system is adjusted using the camera system. [6]

A NIL master structure of 38.48 lp/mm in average was exposed by an inkjet-printed photomask with a grating of 1.96 lp/mm. According to this and further experiments, the photomask's ink dots are identifiable in the master structure. This is especially visible in grayscale structures as shown in Figure 1.4. The printer's software determines the ink dot density of the photomask (b) based on the digital gray values (a). Single ink dots are identifiable in the photoresist structure according to the WLI image (c). This is an undesirable side effect of an inkjet-printed photomask. [5]

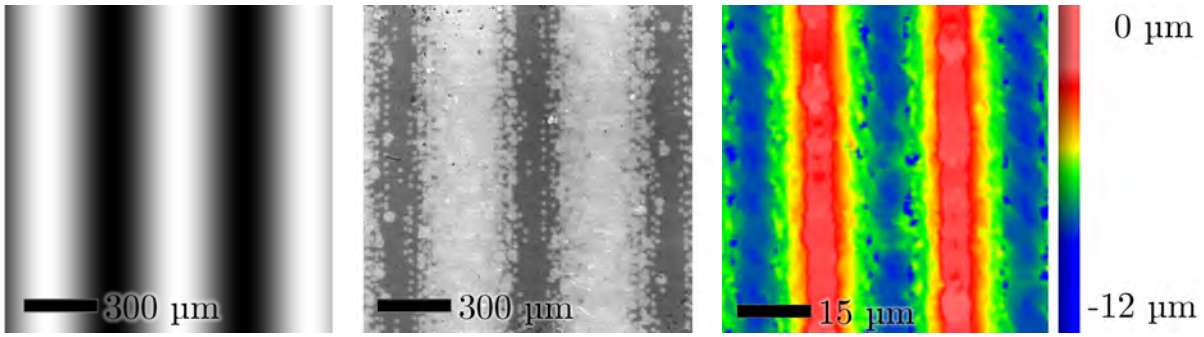

(a) (b) (c)

Figure 1.4: In the shown example, the printed photomask is determined by the digital layout of a sine structure in a size of 600 µm/lp (a). The dot density of the printed mask is determined based on the gray values of the digital layout (b). The mask structure is exposed onto the photoresist by a magnification factor of 0.05. After the development, the mask's ink dots are identifiable in the developed structure of the photoresist (c). [5]

1.2 Goals and Research Questions

The main goal is to design a new lithography system with an additional and adaptive pre-magnification to avoid the imaging of single identifiable ink dots. There are three main questions about the lithography system's setup and its application that should be answered by the research within this thesis. The first question is: Are there specific combinations of settings that let the mask's identifiable ink dots vanish? If there are suitable combinations of settings: Which combination of settings is the most optimal one, by taking the resolution, the FOV, and the distortion into account? Furthermore, the deliberate vanishing of the mask's identifiable ink dots will modify the image and the question arises: Is it possible to develop steep edges in a photoresist and simultaneously keep the contrast of the original mask image by manipulating the imaging?

The methodology and the applied principle of letting the mask's identifiable ink dots vanish are dealt with in detail in Chapter 3. In general, the construction of the lithography system is based on the printing system's analysis and takes the photomask's resolution as well as the edge quality into account. The assembled lithography system is parameterized with respect to the resolution and the magnification of each system unit, the spot diameter, and the resulting exposure power.

2 Fundamentals

2.1 Optical Fundamentals

Ray and wave optics are dealt with within the optical fundamentals. Both models are based on the propagation principles of electromagnetic radiation. The visualized rays in ray optics point in the propagation direction of a wavefront element in isotropic media and simplify the physical behavior of the propagating electromagnetic waves. Physical phenomena such as reflection and refraction are explainable using ray optics. Wave optics are applied to wave-based phenomena such as diffraction, interference, and polarization. [20]

In classical physics, electromagnetic radiation propagates in vacuum with light speed c_0. The speed of light is derived from the MAXWELL'S equations and depends on the electric constant ε_0 and magnetic constant μ_0 as shown in Equation 2.1.1. [20], [45]

$$c_0 = \frac{1}{\sqrt{\varepsilon_0 \cdot \mu_0}} = 299792458 \, \frac{m}{s} \tag{2.1.1}$$

In a medium m, the electric constant ε_0 and the magnetic constant μ_0 are chancing with respect to the wave frequency ω. According to Equation 2.1.2, the electric constant ε_0 and the magnetic constant μ_0 are multiplied by the relative electric constant ε_r and the relative magnetic constant μ_r of the medium. [45]

$$c_m(\omega) = \frac{1}{\sqrt{\varepsilon_0 \varepsilon_r(\omega) \cdot \mu_0 \mu_r(\omega)}} \tag{2.1.2}$$

The refractive index n of a medium m is the ratio between the speed of electromagnetic waves in a vacuum c_0 and medium c_m based on Equation 2.1.3. The refractive index n_m depends on the wave frequency ω as much as a the wave speed c_m of Equation 2.1.2. Since the refractive index n is a parameter of the

propagation speed, it quantifies the optical density of media. [20], [45]

$$n_m(\omega) = \frac{c_0}{c_m(\omega)} \tag{2.1.3}$$

2.1.1 Ray Optics

2.1.1.1 Reflection

Reflection occurs whenever a ray hits an optically denser medium. The effect of reflection is demonstrated on a plane mirror example in Figure 2.1. The incidence angle α and reflection angle α' refers to the surface normal and both angles are equal as given in Equation 2.1.4. [20], [45]

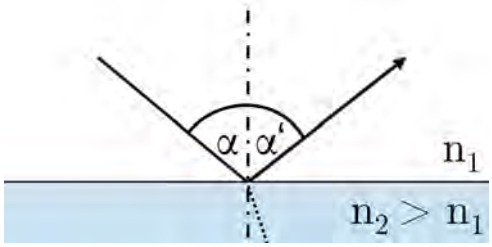

Figure 2.1: Reflection on a plane mirror. T he incidence and reflection angle between the surface normal and the ray are equal.

$$\alpha = \alpha' \tag{2.1.4}$$

Plane mirrors are a common example for reflection due to their great reflectivity R. Mirrors are polished metals or coated with a metal layer, which causes a great optical density difference between the mirror surface and atmosphere. According to Equation 2.1.5, the difference of the reflective indices Δn_m determines the reflectivity at a boundary surface. [20]

$$R = \frac{(n_m - n_{m+1})^2}{(n_m + n_{m+1})^2} \tag{2.1.5}$$

2.1.1.2 Refraction

An incidents ray is refracted at the boundary surface of two media as shown in Figure 2.2. This Figure is used to derive SNELL's refraction law. [20], [45]

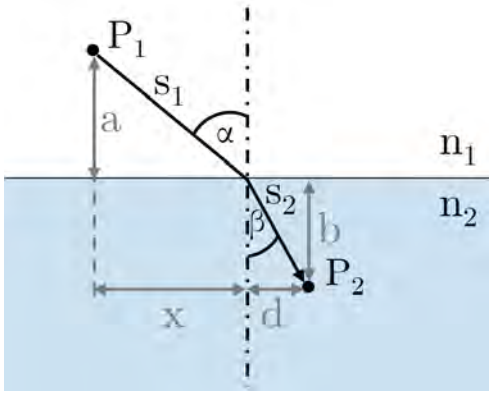

Figure 2.2: Reflection on a plane mirror. The incidence and reflection angle between the perpendicular line and the ray are equal.

The refraction at a boundary surface depends on the Optical Path Length (*OPL*), which is the metric path length s_m weighted by the optical density of the respective media n_m. The resulting *OPL* is the sum of all weighted metric path lengths which occur in the propagated media m as described in Equation 2.1.7. [20], [45]

$$OPL = \sum_{m=1}^{N} n_m s_m \tag{2.1.6}$$

In Figure 2.2, the total optical path length OPL_t from P_1 to P_2 is defined in Equation 2.1.7.

$$OPL_t = \sum_{m=1}^{2} n_m s_m = n_1 s_1 + n_2 s_2$$

$$OPL_t = n_1 \sqrt{a^2 + x^2} + n_2 \sqrt{b^2 + d^2} \tag{2.1.7}$$

According to the FERMAT's principle, a ray propagates on the fastest path, even if this is longer than the direct path. The minimum of the OPL defined by the zero of the first derivation as shown in Equation 2.1.8. [45]

$$\frac{\delta OPL}{\delta x} = 0 \tag{2.1.8}$$

The Equation 2.1.8 can applied on the total optical path length OPL_t from P_1 to P_2. Thereby, the optical path length is derived by the distance x. [45]

$$\frac{\delta OPL}{\delta x} = \frac{n_1 x}{\sqrt{a^2+x^2}} - \frac{n_2 d}{\sqrt{b^2+d^2}} = 0 \tag{2.1.9}$$

Based on Figure 2.2, the geometrical relations are determined by Equation 2.1.10.

$$sin(\alpha) = \frac{x}{\sqrt{a^2+x^2}};\ sin(\beta) = \frac{d}{\sqrt{b^2+d^2}} \tag{2.1.10}$$

The geometrical terms of Equation 2.1.9 can be replaced by the Equation's (2.1.10) sine terms of the incident angle α and refractive angle β. Restructuring the new equation, SNELL's law is derived as shown in Equation 2.1.11. [45]

$$n_1\, sin(\alpha) = n_2\, sin(\beta) \tag{2.1.11}$$

2.1.1.3 Paraxial Optics and Lenses

Paraxial optics is a section of the geometrical optics and is based on paraxial approximations. Synonyms of paraxial optics are GAUSSIAN optics or first-order optics. In the following, thin lenses are discussed based on paraxial optics. Thin lenses are optical elements approximated by a single boundary surface as shown in Figure 2.3. The Optical Path Difference (OPD) within the lens is ignored. The parameter such as a object or image-sided focal length f, focal point F, height y, and distance a refer to the lens' center. The image-sided parameters are flagged with $'$. The index indicates the mathematical sign. Left and down pointing parameters are negative. The given parameters can also be applied to other lens shapes such as concave or concave-convex shapes. [16], [20]

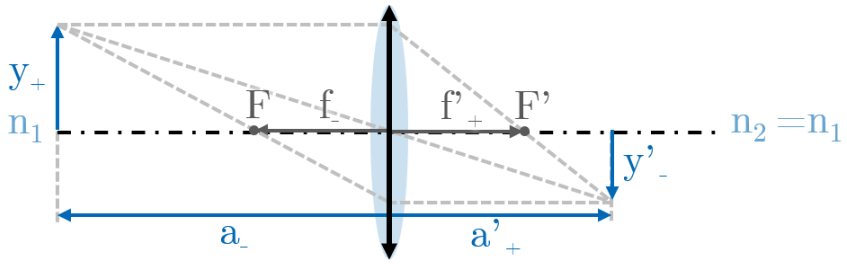

Figure 2.3: The main parameters of a thin lens are the object height y, the image height y', the object distance a, the image distance a', the object-sided focal point F, the image-sided focal point F', the object-sided focal length f, the image-sided focal length f', and the refractive index n_m of the medium m.

Based on the geometrical relation, the lens equation of Equation 2.1.12 can be derived from Figure 2.3 (a). In case of paraxial approximation, the lens equation is reliable for thin lenses. [16], [45]

$$\frac{f'}{a'} + \frac{f}{a} = 1 \tag{2.1.12}$$

The transversal magnification factor β of the imaging is the ratio between the image height y' and object height y' or image distance a' and the object distance a weighted by the refractive index of media n_m as shown in Equation 2.1.13. [16]

$$\beta' = \frac{y'}{y} = \frac{a' n_1}{a n_2} \tag{2.1.13}$$

The ratio of the object-sided depth of field Δa and image-sided depth of focus $\Delta a'$ is the axial magnification as demonstrated in Figure 2.4. The axial magnification equals the transversal magnification to a power of two according to Equation 2.1.14. [16]

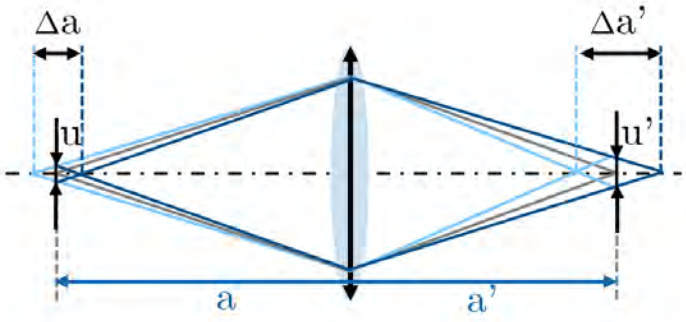

Figure 2.4: The depth of field $\Delta a'$ is the object-sided tolerable distance between the farthest and the nearest object plane which is imaged sharply in the image plane. The depth of focus $\Delta a'$ is the image-sided distance between the farthest and the nearest image plane. If the image plane is captured by a sensor or eye, the minimal feature size u' determines the depth of field $\Delta a'$.

$$\beta'^2 = \frac{\Delta a'}{\Delta a} \tag{2.1.14}$$

The angular magnification Γ is used in case of afocal lens systems. In afocal systems the object and image is at infinity, as illustrated in Figure 2.5. The lateral magnification of y is undefined. Therefore, the angular magnification is calculated based on the incident angle σ and refractive angle σ' of the chief ray[1]. The definition of the angular magnification is given in Equation 2.1.15. [16]

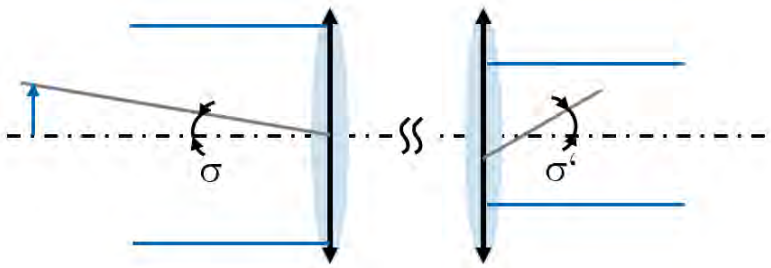

Figure 2.5: The angular magnification is calculated with respect to the incident angle σ and refractive angle σ' of the gray chief ray.

[1]The chief ray passes an off-axis object point and the center of the entrance pupil.

$$\Gamma = \frac{\sigma'}{\sigma} \tag{2.1.15}$$

2.1.1.4 Telescope and Microscope

Common examples for two lens systems are the KEPLER telescope, GALILEI telescope and microscope. In the following, those three optical systems will be explained, since these lens systems are basics for the lithography system's setup. [16], [20]

Astronomic telescopes image far objects on the retina of the observer. In addition, the telescopes are used for further fields of application such as beam widening or reduction and magnification devices for precise tasks. The KEPLER telescope is based on two convex lenses as illustrated in Figure 2.6. The objective captures the object height y and creates a real intermediate image of the object. The eyepiece magnifies the real intermediate image and images it into the observer's eye. The KEPLER telescope has two advantages in comparison to the GALILEI telescope due to the real imaging in the focal points and the spacious setup. Using a KEPLER telescope instead of a GALILEI telescope, greater magnifications can be realized and a field lens[2] can be applied to improve homogeneous illumination of the imaging.[20], [45]

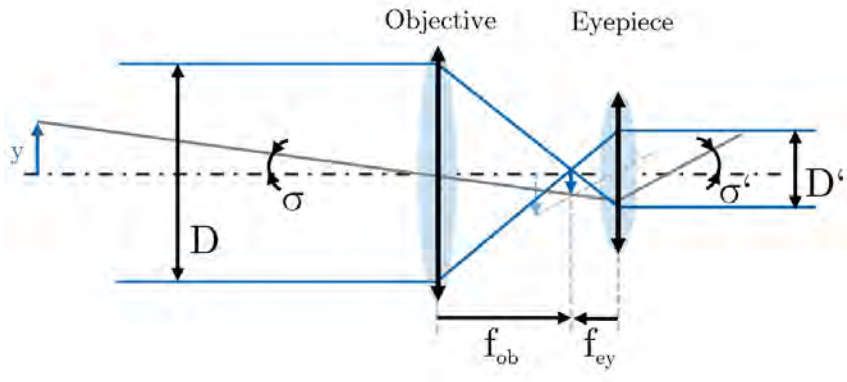

Figure 2.6: The KEPLER telescope is based on two convex lenses. The objective lens captures the object y. The eyepiece magnifies the real intermediate image as illustrated by the transparent arrow.

[2] A field lens images the entrance pupil to the exit pupil. It captures the marginal rays and avoids their radiation out of the system.

If the KEPLER telescope is used for beam size modification, the ratio of the marginal rays D to D' are determined by angular magnification Γ. According to the Equation 2.1.15, the angular magnification Γ of the KEPLER telescope can calculated by the chief ray and the ratio of the focal lengths f_{ob} and f_{ey} as given in Equation 2.1.16. [20], [45]

$$\Gamma = \frac{\sigma'}{\sigma} = \frac{f_{ob}}{f_{ey}} = \frac{D}{D'} \tag{2.1.16}$$

The GALILEI telescope is comparable to the KEPLER telescope as shown in Figure 2.7. It has also an objective and an eyepiece but the setup is different, since a concave eyepiece is applied instead of the convex one. This causes a virtual imaging in the joint focal points of f_{ob} and f_{ey}. In comparison to the KEPLER telescope, the GALILEI is more compact using the concave lens. Another advantage is the lower energy density in the system due to the virtual imaging instead of the real imaging. This is useful in laser beam modifications for example, since thermal effects can be minimized.[20], [21]

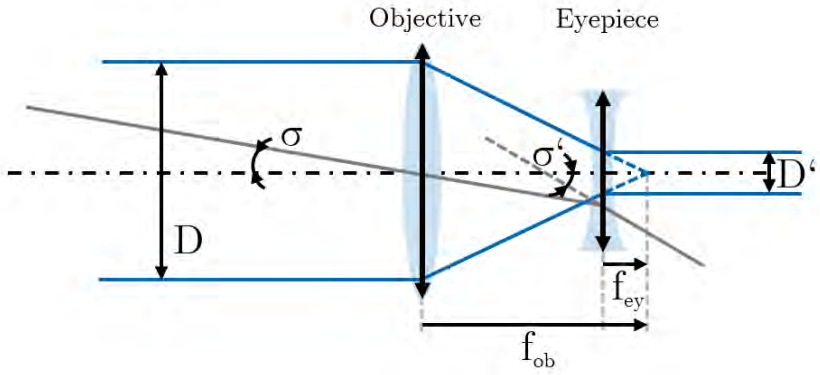

Figure 2.7: The GALILEI telescope is based on a convex and concave lens. The objective lens captures the object and the concave eyepiece in front of the objective's focal point f_{ob} causes a virtual image at the joint focal points of f_{ob} and f_{ey}.

According to Figure 2.7, the angular magnification Γ can be calculated by the ratio of the chief ray angles σ and σ', focal lengths f_{ob} and f_{ey}, or beam widths D and D'. The respective mathematical definition is given in Equation 2.1.17.

It is equal to Equation 2.1.16 of the KEPLER telescope. [20]

$$\Gamma = \frac{\sigma'}{\sigma} = \frac{f_{ob}}{f_{ey}} = \frac{D}{D'} \tag{2.1.17}$$

A microscope is used to capture small objects and magnify them by an increased refractive angle on the retina or measurement device. Two convex lenses are used to capture the object y as demonstrated in Figure 2.8. The short focusing objective causes a magnified real intermediate image in an image distance that is significantly greater than the objective's focal length f_{ob}. The real intermediate image is magnified a second time by the eyepiece. The focal lengths of the objective f_{ob} and eyepiece f_{ey} are positioned in the tube distance t. In commercial systems, the tube distance t is specified to change the objective or eyepiece lenses for further magnification settings. [20], [45]

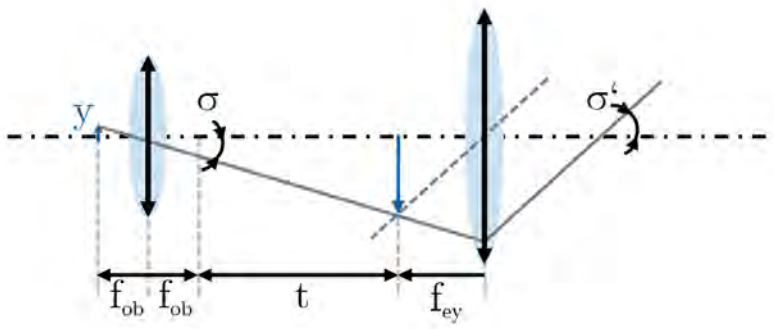

Figure 2.8: The microscope is based on two convex lenses. The objective imaged the magnified object far behind its focal point. The eyepiece captures the real intermediate image and magnifies it again. The distance between the focal lengths of the objective f_{ob} and eyepiece f_{ey} is the tube distance t.

The resulting angular magnification is defined by the object distance a, the tube length t and the focal lengths f_{ob} and f_{ey} as given in Equation 2.1.18. [45]

$$\Gamma = \frac{a\,t}{f_{ob}\,f_{ey}} \tag{2.1.18}$$

2.1.2 Wave Optics

Wave optics are based on the physical principles of electromagnetic waves which are defined by the four MAXWELL's equations of GAUSS's, FARADAY's and AMPERE's laws. These equations describe the interaction of electric and magnetic fields as well as the electromagnetic radiation in matter. The resulting wave equation is describable by the electric field $\vec{E}$, and its change $\Delta\vec{E}$, the phase velocity of different matter c, and time t as given in Equation 2.1.19. [20], [21]

$$\Delta\vec{E} - \frac{1}{c^2}\frac{\partial^2}{\partial t^2}\vec{E} = 0 \tag{2.1.19}$$

There are several solutions to the wave equations. The plane and spherical wave solution will be described. A plane wave propagates perpendicular to the normal $\vec{k}$ and has a wavelength of λ as illustrated in Figure 2.9. [20], [21]

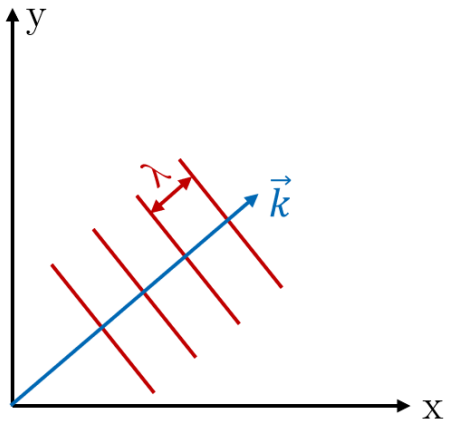

Figure 2.9: Two-dimensional illustration of a plane wave with a certain wavelength λ. The vector $\vec{k}$ is the normal of the wavefront.

The electrical field amplitude of a plane wave depends on the position $\vec{r}$ and time t. It is defined by Equation 2.1.20. The main parameters of the resulting electric field E are the amplitude E_0, angular frequency ω, time t, wave vector $\vec{k}$, position vector $\vec{r}$ and unit vector $\vec{e}$. [20]

$$E(\vec{r},t) = E_0 e^{i(\omega t - \vec{k}\vec{r})};\ \text{with}\ \omega = \frac{2\pi}{\lambda}\cdot c,\ \vec{k} = \frac{2\pi}{\lambda}\cdot\vec{e},\ \vec{r} = \begin{pmatrix} x \\ y \\ z \end{pmatrix} \tag{2.1.20}$$

If all points of a wavefront have the same wave vector $\vec{k}$, the Equation 2.1.21 is true and the wavefront is plane. [20]

$$\omega t - \vec{k}\vec{r} = const \tag{2.1.21}$$

In contrast to the plane wave, a spherical wave propagates in all directions from its origin. A two-dimensional illustration of a spherical wave with a radius r and the wavelength λ is shown in Figure 2.10. [20], [71]

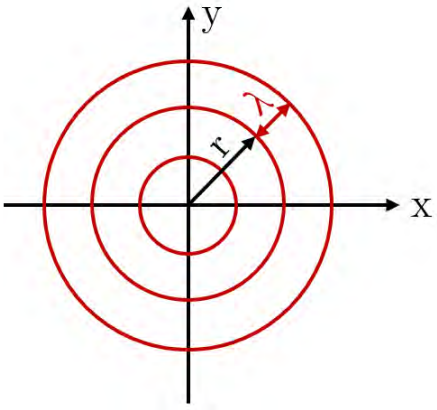

Figure 2.10: Two-dimensional illustration of a spherical wave with a certain wavelength λ. The spherical waves spread from its origin along all dimensions.

A spherical wave is defined by the amplitude E_0, angular frequency ω, time t, wave number k, radius r as given in Equation 2.1.22. [21],[71]

$$E(r,t) = E_0 \frac{e^{i(kr-\omega t)}}{r}; \text{ with } \omega = \frac{2\pi}{\lambda} \cdot c, \; k = \frac{2\pi}{\lambda} \tag{2.1.22}$$

2.1.2.1 Superposition

During the superposition of two or several waves j, the resulting electrical field amplitude E_{res} is defined by the addition of the respective amplitudes E_j at the position of $|\vec{r}|$ at time t as it is given in Equation 2.1.23. [18], [20]

$$E_{res}(\vec{r},t) = \sum_{j=1}^{N} E_j(\vec{r},t) \tag{2.1.23}$$

If two waves with a phase difference ϕ_0 are crossing, the resulting electrical field amplitude is defined as shown in Equation 2.1.26. [21], [37]

$$E_{res}(\vec{r},t) = E_{01}e^{i(\omega t-\vec{k}\vec{r})} + E_{02}e^{i(\omega t-\vec{k}\vec{r}+\phi_0)} = e^{i(\omega t-\vec{k}\vec{r})}(E_{01}+E_{02}e^{i\phi_0}) \quad (2.1.24)$$

The wave E_{res} can not be measured by a detector due to the high spatial frequency. Therefore, the intensity is measured which equals the square of the absolute amplitude as described in Equation 2.1.25. The incidence waves' intensities I_1 and I_2 interfere with each other at a detector. They cause the measured Intensity I_{res} as displayed in Figure 2.11.

$$I \sim |E|^2 \quad (2.1.25)$$

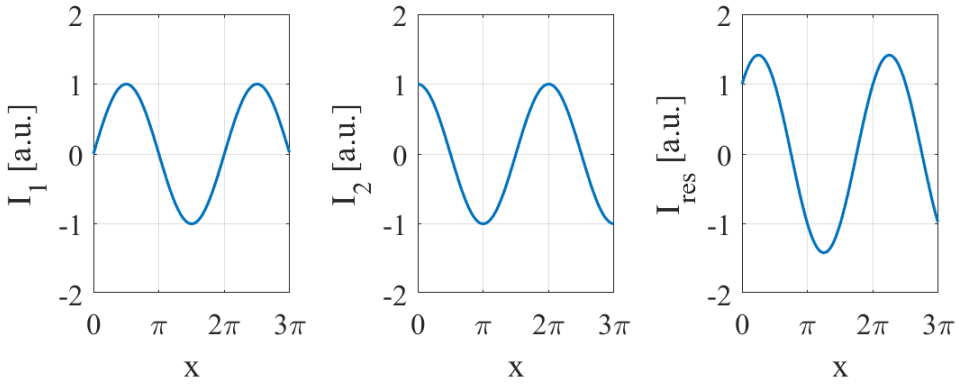

Figure 2.11: Two-dimensional illustration of two waves' interference. The resulting wave I_{res} is the superposition of I_1 and I_2.

Two extreme interference cases can be distinguished. One case is constructive interference as shown in Figure 2.12. Thereby, the phase difference ϕ_0 is an even multiple $2n$ of π. [37], [45]

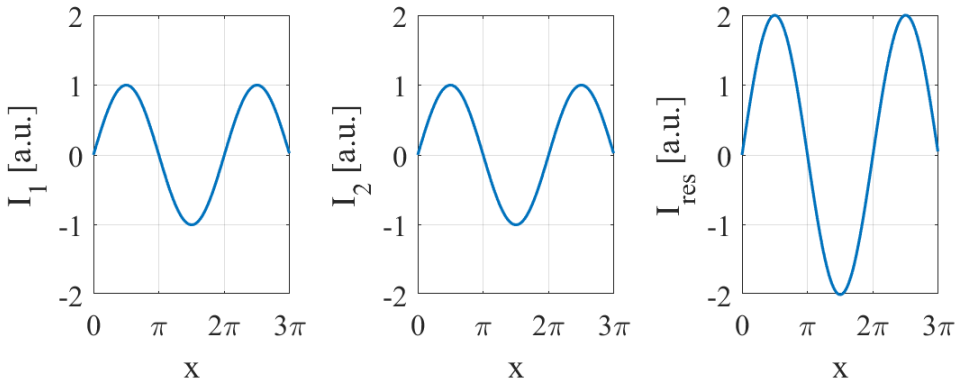

Figure 2.12: The constructive interference of I_1 and I_2 causes a maximal amplitude of the resulting wave I_{res}.

The constructive condition is described in Equation 2.1.26. [37], [45]

$$\phi_0 = 2n\pi \tag{2.1.26}$$

The case of destructive interference is demonstrated in Figure 2.13. The superposition of both waves results in a intensity I_{res} which is equal to zero. [37], [45]

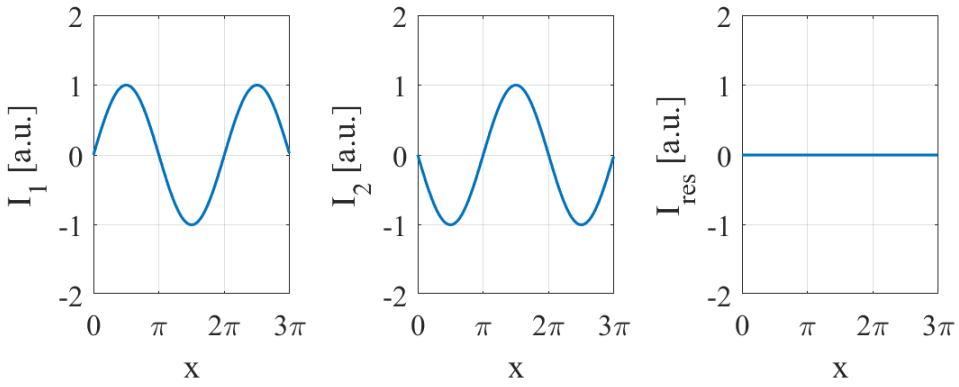

Figure 2.13: The destructive interference of I_1 and I_2 causes amplitude extinction of the resulting wave I_{res}.

In the destructive case, the phase difference ϕ_0 is an uneven multiple $2n+1$ of π as given in Equation 2.1.27. [37], [45]

$$\phi_0 = (2n+1)\pi \tag{2.1.27}$$

2.1.2.2 Diffraction and Optical Grating

The diffraction of a wave is based on the redirection of the wave at a slit. If the circumstances are ideal, the diffraction of a coherent wave can be explained using the HUYGENS principle. According to this, a wavefront can be described by a superposition of an infinite number of spherical waves. An incident plane wave propagates an optical grating by forming spherical waves in the slit. Since the original plane wave changes its propagation from one to infinity directions, this phenomenon is called diffraction. If the slit width w_s is similar to the wavelength λ, it is approximated that one spherical wave per slit propagates the optical grating as shown in Figure 2.14. [20], [21], [71]

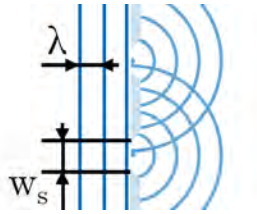

Figure 2.14: The incident plane wave is diffracted at an optical grating. Spherical waves propagate from the split in all directions. The spherical waves create a new wavefront by superpose each other according to HUYGENS principle. If the slit width w_s is equal to the wavelength λ, it is approximated that one spherical wave per slit is formed at the optical grating.

In Figure 2.15, the effect of the FRAUNHOFER diffraction is demonstrated. The interference pattern of the spherical waves is visible at a detector in the far-field region. The intensity maxima m, which are named diffraction orders, are caused by constructive interference at the detector. The geometrical relation of the distance between the diffraction orders d_m is defined in Equation 2.1.28. The distance between the diffraction orders d_m increases if the distance l between the optical grating and the detector or the diffraction angle α_m increases. The diffraction angle α_m increases by decreasing the gating constant g. [20], [21]

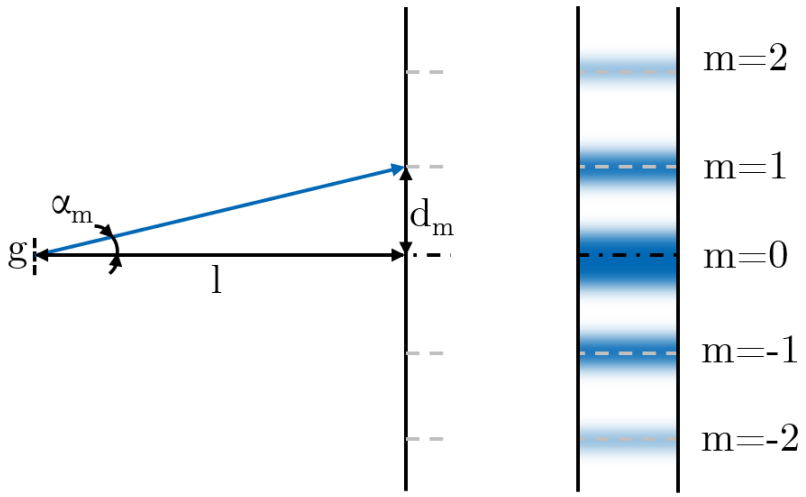

Figure 2.15: Based on the geometrical relations of the FRAUNHOFER diffraction, the distance between the diffraction orders d_m can be calculated. It is a function of the distance l from the optical grating to the detector and the diffraction angle α_m which is directly affected by the diffraction order m, the wavelength λ, and the grating constant g.

$$d_m = tan(\alpha_m)\, l \quad with \quad \alpha_m = arcsin\left(\frac{m\lambda}{g}\right) \tag{2.1.28}$$

In the case of an incoherent illumination, waves are differently diffracted in correlation to their wavelengths according to Equation 2.1.28. The illumination's spectrum is imaged at the detector.

2.1.3 Abbe Theory and Resolution

ABBE's theory of microscopes is based on its imagining path as illustrated in Figure 2.16. An object is illuminated by a coherent illumination source and its image in the image plane is magnified via two positive lenses. The object plane and the aperture plane are in the focal points of lens 1. The aperture plane and the image plane are located in the focal points of lens 2. The microscopes imaging and the diffraction-limited resolution can be explained using the displayed setup of Figure 2.16 and the FOURIER system theory. [17], [25]

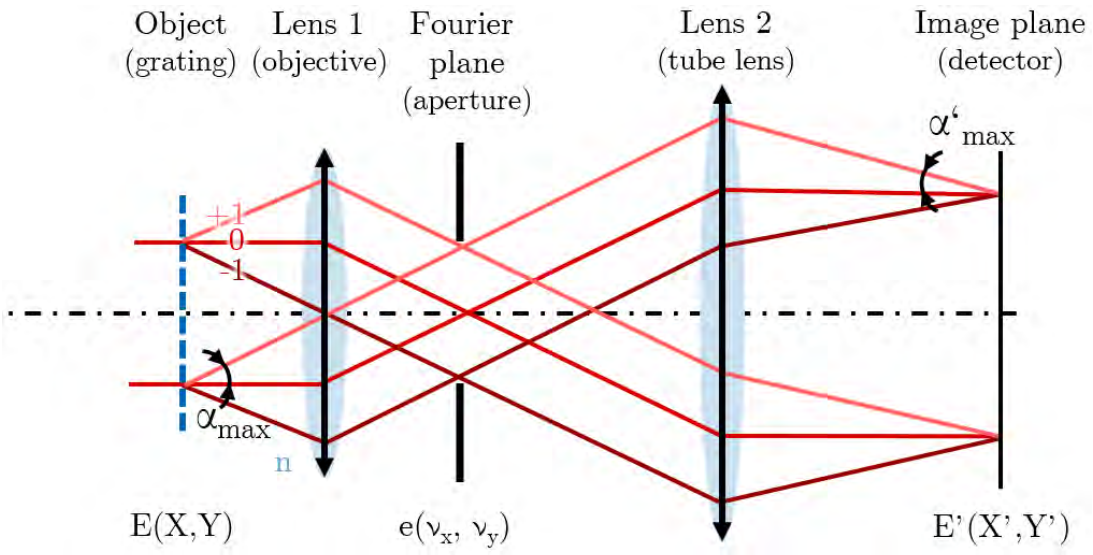

Figure 2.16: ABBE's theory of microscope is based on the FOURIER system theory. Since lenses 1 and 2 transform the object's intensity distribution via the FOURIER plane, the microscope's image can be calculated by multiplication of the original object with the system's complex optical transfer function (OTF).

The ABBE's theory can be explained by the diffraction at an optical grating in the object plane. The diffracted waves are captured by the lens 1 which image the object to infinity. This is equals to the FOURIER transformation of the object's complex electrical field amplitude $E(X,Y)$ that causes the imaging of complex electrical field amplitude $e(\nu_x,\nu_y)$ in the FOURIER plane as described by Equation 2.1.29. [25]

$$e(\nu_x,\nu_y) = \mathscr{F}\{E(X,Y)\} = \frac{1}{2\pi}\int\int_{\infty}^{\infty} E(X,Y)\cdot e^{i(\nu_x\cdot X+\nu_y\cdot Y)}dxdy \qquad (2.1.29)$$

The complex electrical field amplitude $e(\nu_x,\nu_y)$ is affected by the microscope's projection characteristic. The complex Optical Transfer Function[3] OTF describes the system's projection of an object's point in the image plane as a function of the spatial frequency ν. The system-affected complex electrical field amplitude $e'(\nu_x,\nu_y)$ can be calculated by a multiplication with the $OTF(\nu_x,\nu_y)$ in the FOURIER domain as shown in Equation 2.1.30. [17], [25]

$$e'(\nu_x,\nu_y) = e(\nu_x,\nu_y)\cdot OFT(\nu_x,\nu_y) \qquad (2.1.30)$$

[3]The complex $OFT(\nu_x,\nu_y)$ is equivalent to the Point Spread Function $PSF(X,Y)$ in the spatial domain.

The lens 2 captures the resulting complex amplitude $e'(\nu_x, \nu_y)$ and images the object in the image plane. This is analog to an inverse FOURIER transformation of the resulting complex amplitude $e'(\nu_x, \nu_y)$ as given in Equation 2.1.31. The image of the FOURIER plane is transformed back to the spatial domain. The incident waves onto the image plane interfere at the detector and causes the microscope's image. [17], [25]

$$E'(X,Y) = \mathscr{F}^{-1}\{e'(\nu_x, \nu_y)\} = \frac{1}{2\pi} \int \int_{\infty}^{\infty} e'(\nu_x, \nu_y) \cdot e^{-i(\nu_x \cdot X + \nu_y \cdot Y)} d\nu_x d\nu_y \tag{2.1.31}$$

In the case of a normal coherent illumination, the first diffraction order must pass the system to ensure the interference on the detector in the image plane. As illustrated in Figure 2.16, the aperture stop determines the transmitted diffraction orders and the resulting spectrum in the FOURIER plane. It has the effect of a low pass filter since it cuts off higher diffraction orders. ABBE's resolution limit of a diffraction-limited microscope is defined by the wavelength λ and the maximum first order diffraction angle passing the system α_{max} as given in Equation 2.1.32. In addition, the *NA* increases using an immersion medium n and the system's resolution becomes higher. [17], [25]

$$g_{min,coherent} = \frac{\lambda}{n\ sin(\alpha_{max})} \tag{2.1.32}$$

In contrast, if the illumination is incoherent and not coherent, the diffraction does not correlate with wave's phase. The diffracted waves do not constructively or destructively interfere and the detected image is based on the addition of the diffracted waves. Therefore, the minimal resolved grating constant $g_{min,incoherent}$ is two times smaller than the minimal grating constant $g_{min,coherent}$ using a coherent illumination. In case of an incoherent illumination, the minimal grating constant $g_{min,incoherent}$ can be calculated by the wavelength λ, the diffraction angle α_{max} and the immersions medium's refractive index n as de-

scribed in Equation 2.1.33. [17], [25]

$$g_{min,incoherent} = \frac{\lambda}{2\, n\, sin(\alpha_{max})} \tag{2.1.33}$$

At this point, it must be noted that the ABBE's theory of microscopes can be applied to lithography systems since a lithography system is based on an inverse illuminated microscope.

2.1.3.1 Numerical Aperture

The Numerical Aperture *NA* of a system is defined by the system's opening angle θ, which is equal to the refracted diffraction angle α'_{max} of Figure 2.16. If an immersion medium is used, its impact is taken into account by multiplying its refractive index n. The geometrical relations of these parameters are shown in Figure 2.17 and the respective equation is given in Equation 2.1.34. [18], [20], [21]

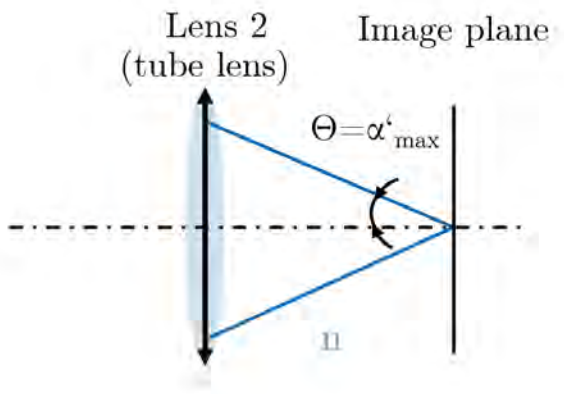

Figure 2.17: The system's numerical aperture *NA* is a function of the system's opening angle θ, which is equal to the refracted diffraction angle α'_{max}, and the refractive index n of the immersion media.

$$NA = n \sin\theta \tag{2.1.34}$$

2.1.3.2 Modulation Transfer Function

The difference of an ideal diffraction-limited system and the real aberration-affected system is defined by the complex $OTF(\nu)$. The $OTF(\nu)$ is based on the Modulation Transfer Function $MTF(\nu)$ and the Phase Transfer Function $PTF(\nu)$ as described in Equation 2.1.35. Since the complex $OTF(\nu)$ can not be detected, the absolute $|OTF(\nu)|$ is measured in a MTF analysis. [17], [25]

$$MTF(\nu) = |OTF(\nu)| = |MTF(\nu) \cdot e^{i\,PTF(\nu)}| \tag{2.1.35}$$

The MTF of an optical system is measured by taking the minimum intensity I_{min} and maximum intensity I_{max} of the respective structure's frequency into account. The relation of the minimum intensity I_{min} and maximum intensity I_{max} is the contrast C as described in Equation 2.1.36. [20]

$$C = \frac{I_{max} - I_{max}}{I_{max} + I_{max}} \tag{2.1.36}$$

The Equation 2.1.37 defines the MTF based on the object's and image's contrast according to Equation 2.1.36. [20]

$$MTF = \frac{C_{image}}{C_{object}} \tag{2.1.37}$$

Figure 2.18 illustrates the contrast behavior of system a and b. The MTF of system a is similar to an ideal MFT of a diffraction-limited system. As given in Equation 2.1.38, the cut off frequency ν_{max} of an ideal MTF is equal to the inverse resolution g_{min} of Equation 2.1.32 and 2.1.33 based on ABBE's theory. The MTF of a diffraction-limited system, with an incoherent illumination and a circular pupil, is real. Its ideal MTF is analytically represented by a function of spatial frequencies ν as described in Equation 2.1.39. In the case of a real system, such as system b, system aberrations cause a phase shift. According to Equation 2.1.35, a phase shift results in deviating values of the real MTF as shown in Figure 2.18. The contrast of a real MTF is always lower than

the ideal MTF's contrast due to the affecting phase shift. Therefore, the real maximum resolved spatial frequency is below an ideal system's maximum spatial frequency ν_{max}. This means that the resolution is reduced by aberrations. [14],[17]

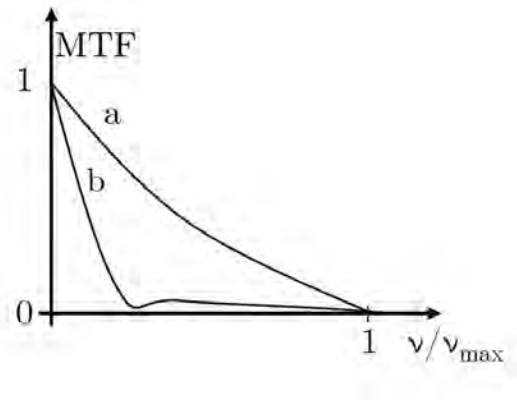

Figure 2.18: MTF visualization of system a and b as a function of the object frequency f in line pairs per mm.

$$\nu_{max} = \frac{1}{g_{min}} \text{ incohrenent illu.: } \nu_{max} = \frac{1}{g_{min,incoherent}} = \frac{\lambda}{2\, n\, sin(\alpha_{max})} \quad (2.1.38)$$

$$MTF(\nu) = \frac{2}{\pi}\left[arccos\left(\frac{\nu}{\nu_{max}}\right) - \frac{\nu}{\nu_{max}}\sqrt{1-\left(\frac{\nu}{\nu_{max}}\right)^2}\right] \quad (2.1.39)$$

An optical system consisting of several units can be described by the MTFs of the individual subsystems i with respect to Equation 2.1.40 [49].

$$MTF = \prod MTF_i \quad (2.1.40)$$

A MTF analysis can be conducted using test charts such as the Siemens star or the USAF chart. The UASF chart was invented later than the Siemens star by the U.S. Air Force to evaluate optical systems. The original target consists of nine groups with six elements. The vertical groups and horizontal elements can be assigned to a specific spatial frequency by the numbering. Figure 2.19 shows the USAF target which is used in the experiments. [18], [70]

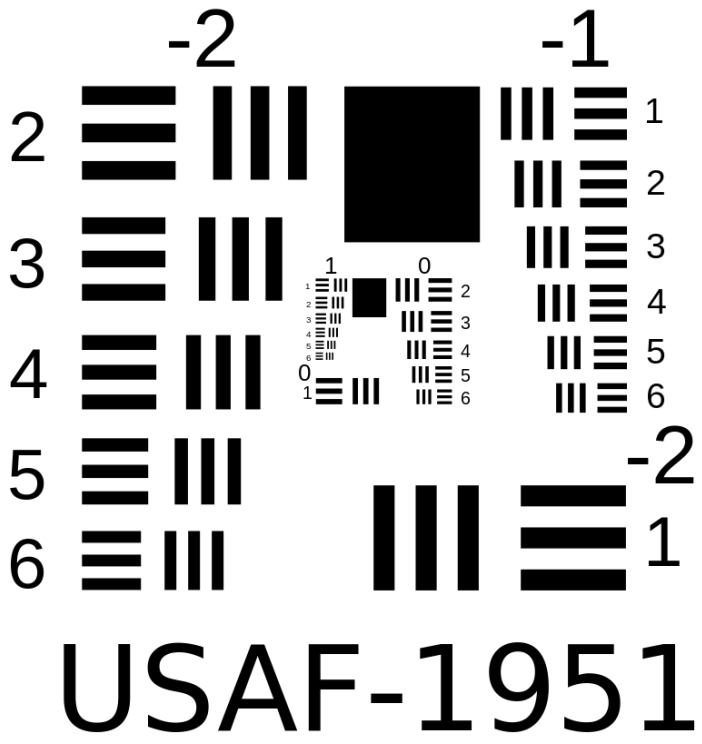

Figure 2.19: The USAF 1951 pattern is a test chart to evaluate the contrast of certain spatial frequencies [70].

2.1.3.3 Rayleigh Criterion

Since optical systems are not aberration-free and they can not be used up to ABBE's resolution limit, there are resolution criteria that define resolution limits based on the Point Spread Function (PSF) of two points. According to the RAYLEIGH criterion, the intensity maximum of one point's PSF must coincide with the first intensity minimum of the other point's PSF, as displayed in Figure 2.20. [17]

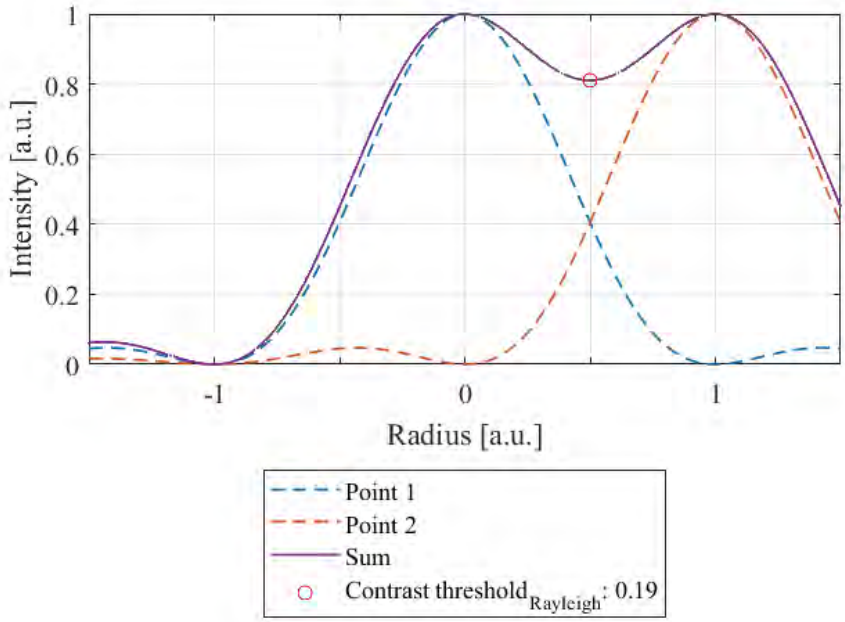

Figure 2.20: The contrast threshold of the MTF analysis is based on RAYLEIGH criterion. According to the RAYLEIGH criterion, the intensity maximum of first point's PSF must be lie in the first intensity minimum of the second point's PSF.

The lateral resolution Δx based on the RAYLEIGH criterion is equal to the distance of the two points' maxima. It is a function of a factorized wavelength λ and the system's NA using a small-angle approximation as given in Equation 2.1.41.

$$\Delta x = 0.61 \frac{\lambda}{NA} \tag{2.1.41}$$

Since optical systems have an impact on the resulting point widths, the contrast threshold based on the RAYLEIGH criterion is determined to 0.15 [17] up to 0.27 [30]. In the following MTF analysis, the contrast threshold is set to 0.2 to evaluate the system's resolution. [1], [13], [41]

2.1.4 Distortion

The distortion of an image is caused by refraction of the chief ray in the system as shown in the simplified Figure 2.21. There are two types of distortion. According to Figure 2.21 (a), the positive distortion drags the image's edges outward due to a chief ray diffraction in front of the aperture. It is also known as pincushion distortion. Refraction of the chief ray behind the aperture stop

leads to a negative barrel distortion as illustrated in Figure 2.21 (b). A system's zoom setting, which is based on the variation of the lenses' distances to the aperture stop, and the lenses' thicknesses have an impact on the distortion. Distortion is the only aberration that does not affect the resolution.

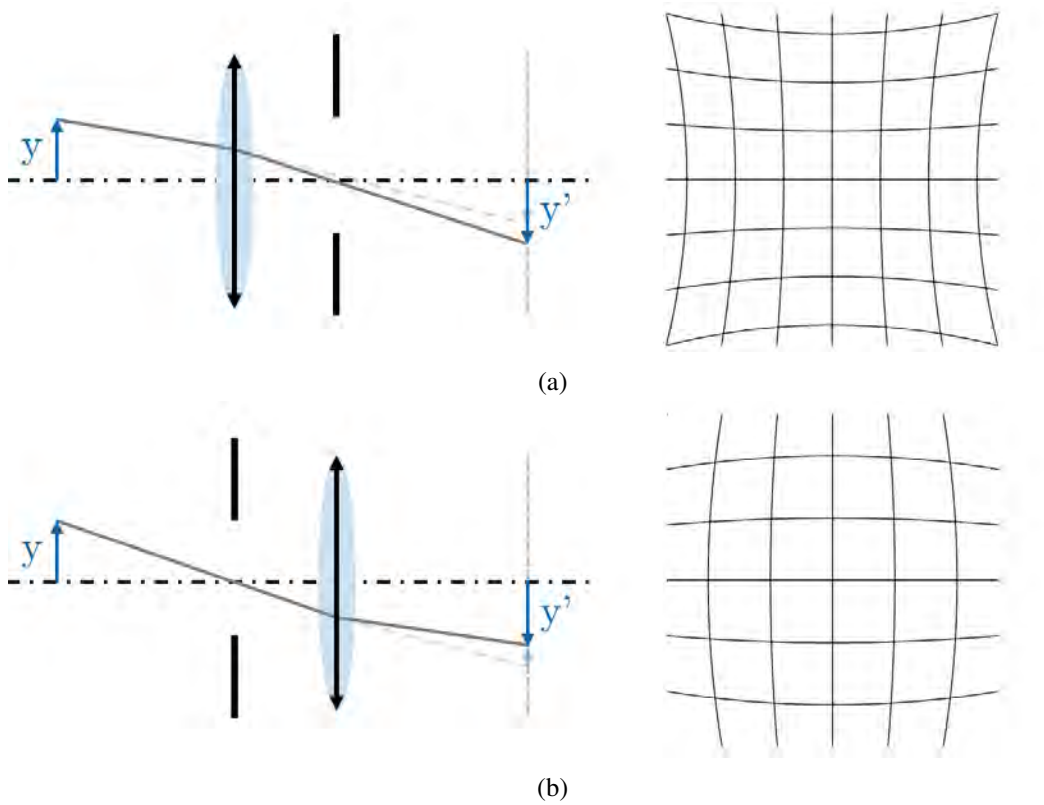

Figure 2.21: Positive distortion is caused by an refraction of the chief ray in front of the aperture stop (a). In contrast, negative distortion is based on a chief ray's refraction after the the aperture stop (b).

Since distortion is a symmetric aberration, it is measured frequently as a function of the radial distance to the center R_i. The respective absolute radial distortion D_i is the absolute distance from the measured image point (red) to the ideal image point (blue) as shown in Figure 2.22. The absolute radial distortion D_i is calculated based on Equation 2.1.42.

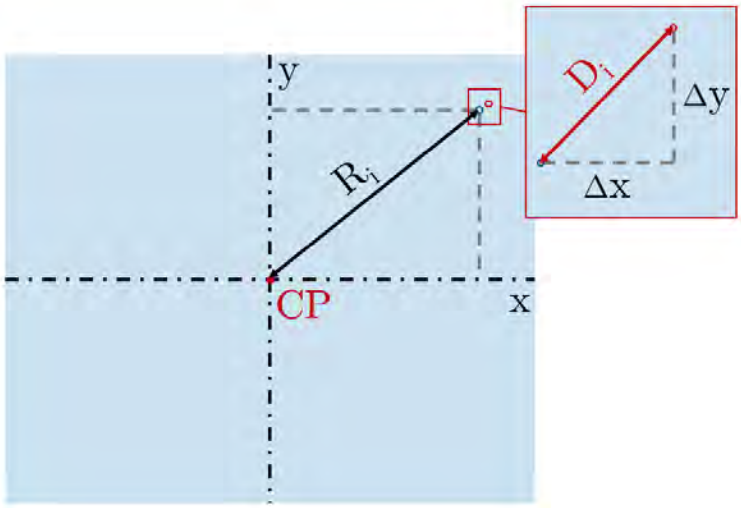

Figure 2.22: The measured distortion is a function of the radial distance to the center R_i. The respective absolute radial distortion D_i is the absolute distance from the measured image point (red) to the ideal image point (blue).

$$D_i(R) = \sqrt{\Delta x_i^2 + \Delta y_i^2} \text{ with } R_i = \sqrt{x_i^2 + y_i^2} \tag{2.1.42}$$

2.2 Conventional Lithography

Lithography is versatile with respect to process principles. Several processes are listed under lithography. For example: Photolithography, EUV Lithography, X-Ray Lithography, Electron, or Ion Beam Lithography. Their common characteristic is the reaction in a target substrate by external energetic influence. The substrate partially changes its cohesive characteristic. The partial change of the coherence property is used in order to remove certain areas of the substrate by a developing process. The development refers to a etching process. A distinction is made between wet and dry etching. Photolithography is a common wet etching process since the exposed photoresist and the respective functional layer are developed by a liquid solvent. In the following, the photolithography and applied photomask are dealt with.

2.2.1 Photolithography

Lithography is based on 'stone' (Ancient Greek: *lithos*) printing. It is implemented in 1798 to replicate color printings. Photolithography was developed to

image a master structure on a stone stamp of the lithography printing. Modern photolithography systems are designed to reduce the photomask structure down to 5 nm on a silicon-based substrate using Extreme Ultraviolet (EUV) Light with a wavelength of 13.5 nm. EUV light does not propagate through a lens system since it is absorbed completely by the atmosphere. Therefore, modern lithography systems are adapted. They are based on mirrors instead of lenses and vacuum is generated in the lithography unit. In addition, those photolithography systems are part of a wafer scanner that moves the substrate to expose as much surface as possible within the least amount of time. Modern waver scanners, such as the ASML NXE:5000, have a throughput of 185 wafer per hour. [8],[48], [62], [75]

Common photolithography systems are based on the same components as visualized in Figure 2.23. Light from a powerful light source is coupled into a illumination system. The illumination system widens the beam of the light source and prepares it to illuminate the mask and the substrate homogeneously. The photomask's structure is reduced in size by a projection system and imaged on the substrate. The size reduction has the advantage that the photomask can be produced more easily in greater dimensions and defects are reduced by the reduction in size. The greatest challenge in optical design strategies is to achieve homogeneous illumination while minimizing the structure size according to a reproducible and aberration-free lithography process. [44], [75]

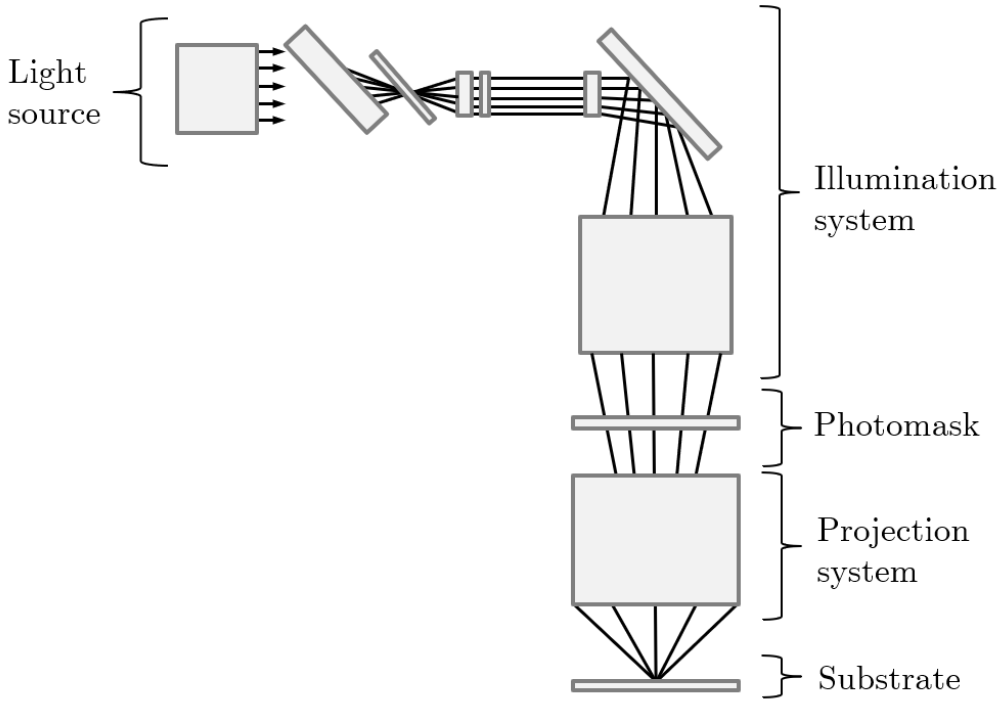

Figure 2.23: The photolithography system's basic setup consists of an illumination system, photomask, projection system, and substrate holder [44].

The resolution and the depth of focus are key parameters of a photolithography system. According to Equation 2.1.32, the resolution of an axial illuminated system is equal to the wavelength λ divided by the numerical aperture NA of the system. The Equation 2.2.1 of the photolithography system's minimum resolved structure g_{litho} is expanded by an application factor k_1. This factor is defined by the total photolithography process. The resolution of the photoresist is taken into account. The factor of application must be as small as possible to achieve the smallest feature size. Common systems have an application factor k_1 of 0.4 to 0.8. However, the application factor is decreased significantly since structures of approximately 5 nm and smaller can be developed using a maximal high-NA of 0.55. [44], [48], [52]

$$g_{litho} = k_1 \frac{\lambda}{NA} \tag{2.2.1}$$

The depth of focus DOF_{litho} has an impact on the vertically exposure of the substrate's structure. It must be sufficiently depth to ensure a minimized image blur. According to Equation 2.2.2, the depth of focus is primarily determined by

the wavelength λ, the application factor k_2 and the NA to a power of two. Since the NA should be large to achieve a small feature size g_{litho} based on Equation 2.2.1 and low as possible with respect to Equation 2.2.2, a compromise between feature size and depth of focus must be found. [44], [52]

$$DOF_{litho} = k_2 \frac{\lambda}{NA^2} \tag{2.2.2}$$

The workflow of a photolithography process in the semiconductor industry is explained based on Figure 2.24. A wet etching process is shown in the workflow. The substrate (e.g. Si, SiO)[4] is prepared by applying a functional layer (e.g. SiO_2, Cr)[5] and a photoresist (e.g. PMMA)[6]. The photoresist is sensitive for Ultra Violet (UV) light which is exposed by the lithography system. If a positive resist is developed, the exposed areas are removed by a water-based solvent. A negative resist is locally polymerized by the exposure energy. The non-exposed areas will be removed during development. After development, the functional layer is etched at the unprotected areas. Finally, the photoresist is removed completely and further etching processes can be conducted. [75]

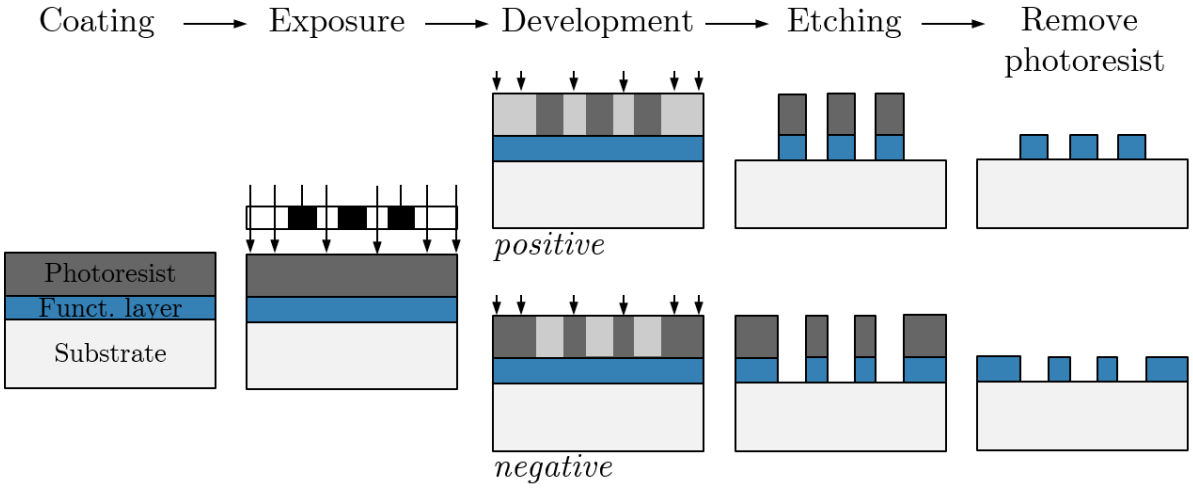

Figure 2.24: Workflow of a basic photolithography process. The developed photoresist layer is used as a wet etch mask for patterning the functional layer. A positive photoresist is dissolved in the exposed areas. In contrast, the negative resist will be removed in the non-exposed areas.

[4] Si: Silicon, SiO: Silicon oxide
[5] SiO_2: Silicon dioxide, Cr: Chromium
[6] PMMA: Polymethylmethacrylat

2.2.2 Photomask

The photomask of a lithography system is also known as a reticle. The original photomask in 1980 was based on Rubylith[7] which is a dual masking film. The first integrated circuits are cut by hand into the first layer of the Rubylith film [23]. As the power of the illumination sources increases, the film mask is deformed by the generated heat during exposure. The next generation of masks had heat-resisting silver halide (AgX e.g. AgBr, AgI, AgCl)[8] structures on standard glass. Since they can be manufactured by a photolithographic process, the silver halide photomasks are suitable for mass production and prevailed as standard. The standard glass was replaced by borosilicate and quartz (SiO_2) to improve the thermal stability while the illumination wavelengths became shorter. Silver halide was replaced by chromium (Cr) since it has better absorption characteristics using UV light. [28], [54],[72]
If the wavelength is smaller than 193 nm, phase-shifting masks are applied to adjust the diffraction and interference behind the mask. A phase-shifting semi-transmitting layer (e.g. MoSi)[9] is deposed on the quartz mask to manipulate the diffraction and increase the contrast as shown in Figure 2.25 [26], [69].

[7] Rubylith is a brand name. It is a masking film based on polyester.
[8] AgBr: Silver bromide, AgI: Silver iodide , AgCl: Silver chloride
[9] MoSi: Molybdenum silicide

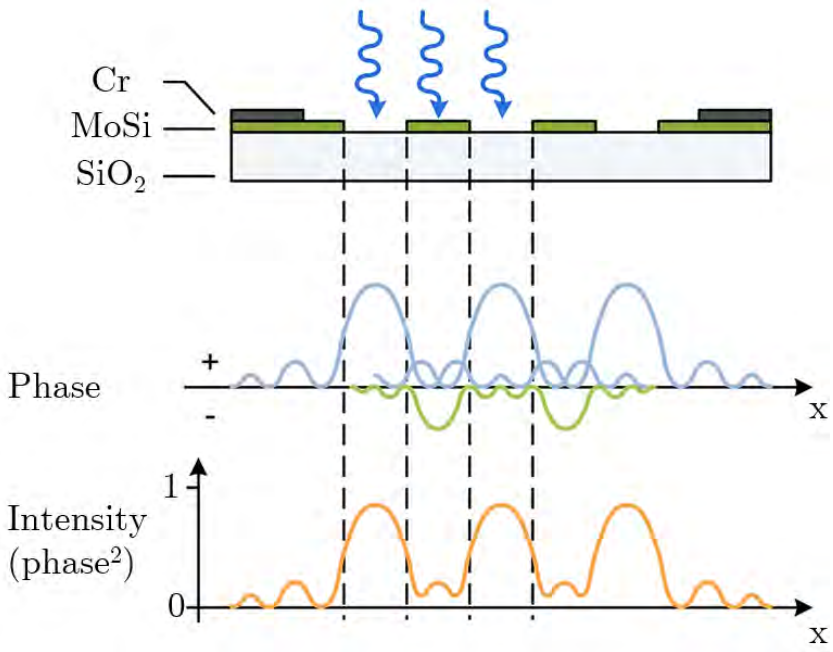

Figure 2.25: In UV lithography using a 193 nm or lower wavelength, a phase shifting mask is required to improve the intensity contrast by a superposition with another phase. The phase shift is caused by a semi-transmitting layer (e.g. MoSi) based on [26].

The photomasks changed in relation to the 13.5 nm EUV lithography implementation. Since the mirror-based systems have an extreme loss of energy due to the partial absorption at the mirrors, the photomask is based on a multi-layer reflector and low thermal expansion absorber. The EUV lithography system's mask is reduced 4x by the projection system. [3], [11], [62]

Regardless of the mask generation, it can be said that the exposed structure is significantly determined by the photomask. Structure defects are transferred through the projection system onto the substrate. Therefore, the photomask and its illumination have a significant impact on the application factor k_1 of Equation 2.2.1 and the resulting resolution of the lithography system. If the projection system's resolution is greater than the photomask's resolution, the photomask limits the exposed structure. [61]

2.3 Inkjet Printing

In the 1960s, continuous printing by amplitude-modulated dispensing was established. The development of drop on demand printing by frequency modulation started a few years later in the 1970s. Todays, inkjet systems are used to apply ink as well as biomedical fluids or conductive materials on paper and other materials. [27], [36]

2.3.1 Digital Layout and Software

The digital layout determines the subsequent printing. The layout's information is stored in a file. There are different file formats to save digital images which are basically distinguished in raster graphics and vector graphics. Raster graphics work on the principle of a pixel array. The digital image information is stored in Cartesian coordinates with no respect to the display size. Zooming into a raster graphic, either a pixel array value is passed to multiple pixels of the screen, or the pixel information is approximated. If the original pixel information is not approximated, the discretization of the raster graphic becomes visible. Typical discrete formats are Portable Network Graphics (PNG), Tagged Image File Format (TIFF) and Windows Bitmap (BMP). Vector graphics have defined image points that are connected by lines, curves, and other shapes. Since the defined connections do not change when the image is rescaled, the graphics can be imaged sharply on varying screen sizes. Scalable Vector Graphics (SVG) is a common file format of vector graphics. [65] [66]

The Raster Image Process (RIP) converts the image from the original file format into a continuous inkjet tone. According to the color tone and respective intensity, the RIP generates a printing pattern that represents the color tone by using the printer's color code (e.g. Cyan Magenta Yellow Key-Black (CMYK)) and calculating the dot density. There are different rendering methods of various printing software. They generate reproducible individual printing patterns by taking the printing setting into account. [33], [36]

2.3.2 Print head

Besides all the mechanical parts, the print head is the main part of a printer. In an inkjet printer, the print head is moved to print in certain areas. A print head is based on a housing and nozzle chambers which dispense the material through the nozzles as shown in Figure 2.26. The mechanical precision and the nozzle density have an impact on the printing resolution. The manufacturers declare the printers' resolution by the dot density in DPI.

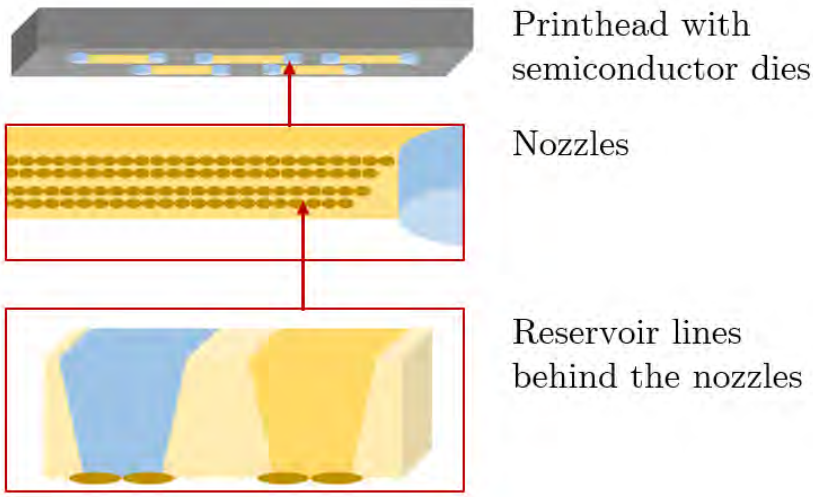

Figure 2.26: The basic components of a inkjet print head are the housing with semiconductor dies. The print head's nozzles are etched into the dies and connected to material reservoirs.

There are different drop on demand technologies that are applied to dispense the material through the nozzle based on thermal, piezoelectric, or electrostatic actuators. Since thermal and piezoelectric print heads will be used in thesis' experiments, the respective drop development will be explained and compared according to Figure 2.27. In Figure 2.27 (a), a current is applied to the resistor of the thermal-based print head which results in a temperature of 350 °C to 400 °C at a resistor's surface. Ink or other material evaporate immediately and generate a pressure wave in the nozzle chamber. A drop is ejected out of the nozzle within 10 µs. Subsequently, a part of the squeezed-out material is sucked back into the chamber by the rising negative pressure. Due to the oscillating pressure, the liquid starts to oscillate for approximately 100 µs. Then, the normal state is reached again. Commercial manufacturers such as Canon and HP fabricate thermal-based print heads because the design is small and a higher nozzle density can be achieved in comparison to a piezoelectric print head.

In piezoelectric print heads, a stimulating voltage is applied to a piezo crystal in order to generate a pressure pulse as shown in Figure 2.27 (b). The material escapes through the nozzle and oscillates after the ejection as explained in case of a thermal-based print head. Subsequently, the material must settle down. Since the drop is mechanically dispensed by the piezo crystal's movement, heat-sensitive materials can be jetted. This is an advantage of the piezoeletric print head in comparison to the thermal-based ones and useful for advanced dispensing of biochemical or conductive material. [2], [27], [34], [36]

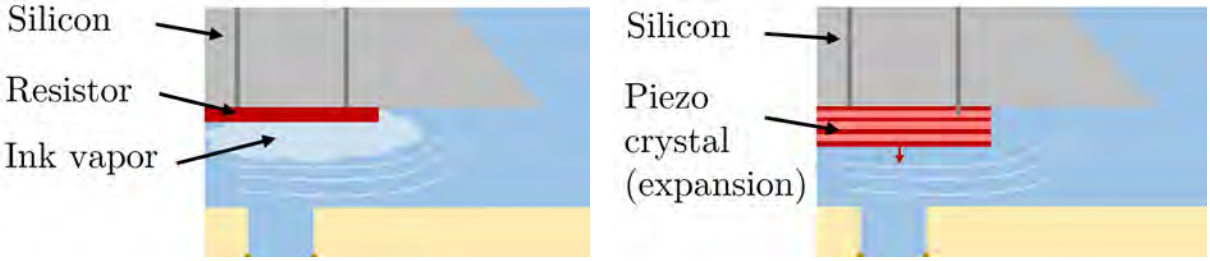

(a) (b)

Figure 2.27: Print heads based on thermal (a) and piezoelectric (b) actuators. The thermal-based print heads dispense material by evaporate material on the resistor's surface and generate a pressure wave. In contrast, the piezo crystals eject out the material mechanically.

As already mentioned, the nozzle distance of the print head and the mechanical drop spacing have a major impact on the printer's resolution. In addition, the resolution is determined by the dried drop size on the substrate. The volume of the material drop, the wetting, and the dry process have an impact on the resulting drop size as shown in Figure 2.28. As visualized in Figure 2.28 (a), the volume of the detached drop is a function of the nozzle diameter a, pressure wave's force F_e, material density ρ, contact angle γ_{c1}, and surface tension between liquid, ambient and nozzle σ as given in Equation 2.3.1 [10]. [51], [74]

$$V = \frac{2\pi a \sigma sin(\gamma_{c1})}{F_e \rho} \tag{2.3.1}$$

If the drop settles down onto the substrate. The dry rate, the resulting surface tension's fore F_s, the wetting fore F_w, and the penetration force F_p affect the drop size. All acting forces depend on the polarity of the drop material and substrate which are included in the contact angle γ_{c2}. In the experiments, which are

[10] The gravitational effect on inkjet drops can be neglected due to the low drop mass.

described in Chapter 3, the inkjet photomask's substrate is Polyethylentereph-thalat PET. The surface of PET and comparable plastics (PE, PVC)[11] have a low polarity which causes a hydrophobic characteristic. The resulting contact angle between the substrate and the high polar water-based ink is large $\gamma_{c2} > 90°$. Since PET foils are not porous, penetration as known from a paper substrate is excluded. Therefore, commercial printing films have additional roughness and promotional coatings to improve wetting and drying. Water-based inks can be modified by chemical supplements to lower their polarity. The dry rate causes a change in the drop's volume V and its material characteristics. Consequently, the drop size will change until it is fully dry. The ambient temperature and additional heating have an impact on the resulting drop size due to the time factor of drying. It is empirically determined that drop on demand systems generate water-based ink dots of 3.5 to 5 pl which results a spot size of 10 to 20 µm. [53], [36], [42],

(a) (b)

Figure 2.28: Visualization of parameters which have an significant impact on the drop volume (a) and the spot size (b).

[11] PE: Polyethylene, PVC: Polyvinyl chloride

3 Methodology

3.1 Analysis of the Printing Systems

The research is divided into two main parts. First, the printing system of the inkjet-printed photomask is characterized. Secondly, the lithography system is constructed by taking the edge quality of the printed mask into account to achieve a ink-dot-free imaging.

A characterization of the printing system is conducted to determine the smallest reproducible structure size and the edge quality of the commercial printer Canon iX6850 using the black (BK) and the pigment-added black (PGBK) cartridges. The ink is dispensed through different print head units. Therefore, the patterns of different inks are analyzed to make conclusions about the print head. According to its datasheet, the printer prints applying 9600 DPI perpendicular to the printing direction. Two structure types are printed in printing system's analysis. The printed structures are directly printed, while the negative structures have a printed background. The structure types are compared to the given size of the digital layout. The digital bar structures vary from 15 µm up to 197.5 µm with 2.5 µm steps. Examples of the digital test patterns are shown in Figure 3.1. The size of the printed structures (a) and negative structures (b) are measured as a bar size *S*. An evaluation based on line pair size is not reliable since binary printed patterns do not have an symmetric duty circle of printed and non-printed parts due to the ink distribution of printed lines. The structure size is measured by a WLI (Zygo) and is automatically evaluated using MATLAB.

(a) (b)

Figure 3.1: Extracted digital layout of the printed structures (a) and the negative structures (b). The measured structure size refers to a single bar and not to a line pair since the printed duty circle is not symmetric.

Since the Canon printer is a closed system, the DMP 2850 is investigated using the black Dimatix test ink. The printer's resolution is set manually via the drop spacing, which must be chosen to match the drop diameter on the substrate. If the drop spacing is too small, too much ink is applied. The printed structures increase in size and the edges become wavy. Otherwise, a too large drop spacing causes unfilled areas. The best drop spacing is determined according to the print edge quality of three 100 µm bars per spacing setting. Therefore, the drop spacing is set to 10 µm and 15 µm. Further spacing settings were excluded from the analysis due to insufficient print quality. Further printing settings such as the printhead temperature, jetting frequency, and applied voltage are adjusted immediately at the drop watcher before printing.

The next step in printing system's analysis is the evaluation of the lowest reproducible structure size. The structure size is varied by a multiple of the minimum drop spacing up to 140 µm. The mean structure width and its reproducibility is analyzed. The reproducibility is determined by the standard deviation of the measured structure widths. The edge quality measured by the standard deviation of the printed edges.

The commercial Canon printer and the DMP are compared. Based on the best achievable edge quality, the lithography system's maximal resolution is calculated.

3.2 Setup and Analysis of the Lithography System

The ink dots of the printed mask structure should no longer be identifiable in the NIL master structure for developing smaller structures and more precise edges. Therefore, the lithography system is rebuilt to only resolving structures larger than edges' ink dots and reducing the structure size. The theory of this method is illustrated in Figure 3.2. In the first system part, the structure of the printed mask (a) is imaged in the intermediate plane (b). The edges' ink dots become blurred and the intensity distribution during exposure is smoothed. According to this, the single ink dots of the printed photomasks will no longer be identifi-

able. In the second part of the system, the intermediate image is reduced onto the substrate plane (c) by an objective lens. The intensity distribution during the photoresist's exposure is still smoothed. A non-linear photoresist is only developed if the exposure intensity exceeds a certain level I_{th} (d). The smoothed intensity distribution results in steep slopes in the non-linear photoresist.

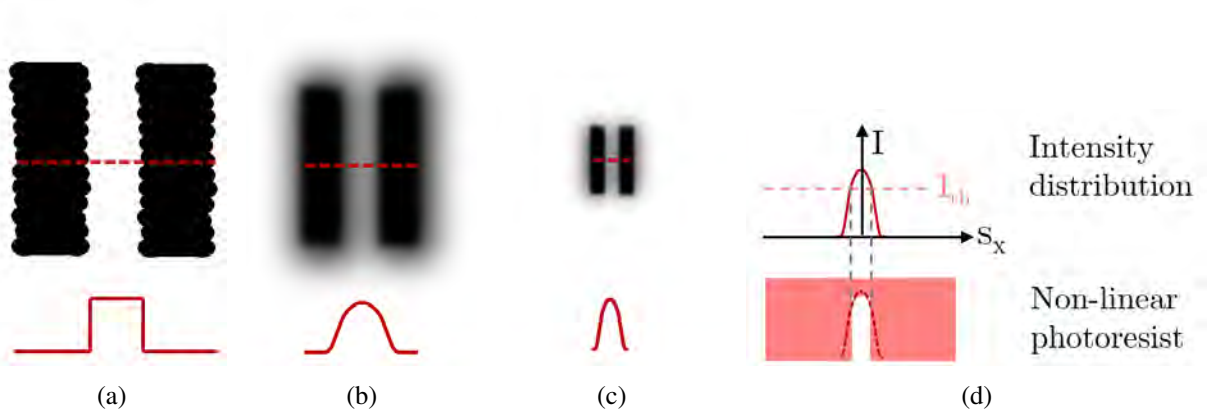

Figure 3.2: Theory of the lithography system's effects on the mask structure and the developed photoresist structure. The mask structure (a) is blurred imaged in an intermediate image (b) to make the ink dots unidentifiable. Subsequently, the structure is significantly reduced onto the photoresist's surface (c). The non-linear photoresist is only developed if a certain energy level is exceeded during exposure (d).

According to the system's concept of Figure 3.2, the basic lithography system consists of two main functional parts in order to make the mask's image blurred and reduce it. The lithography system's basic setup with the respective functional parts is illustrated in Figure 3.3. The printed inkjet mask is illuminated by a 405 nm LED. The mask's ink dots are blurred imaged due to the lower resolution limit of a macro lens than the printing edges' inaccuracy. The second part of the system reduces the intermediate image about 20x onto the substrate plane by a tube lens and a microscope lens.

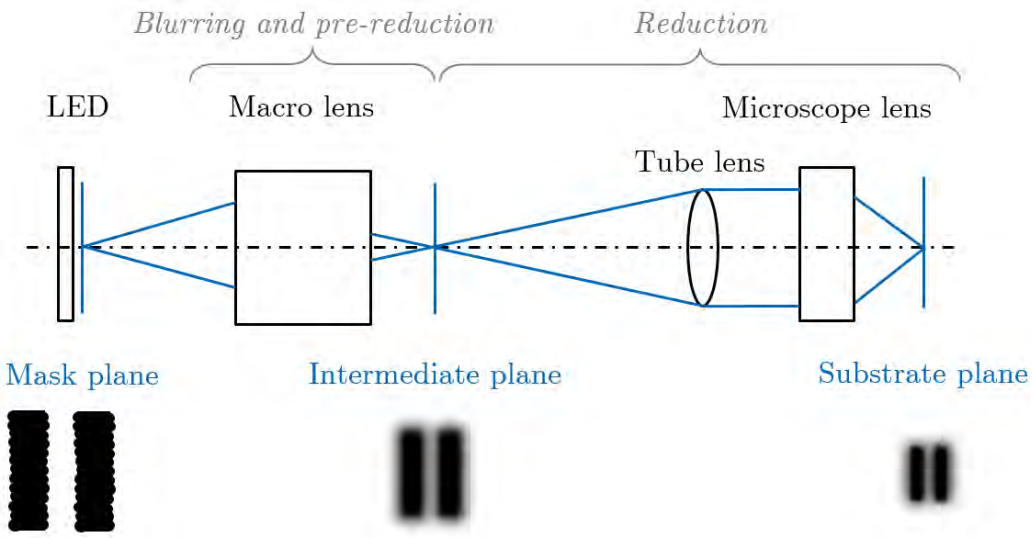

Figure 3.3: Setup of the lithography system based on two functional units. The first unit images blurred structures if they have a structure size below its resolution. In addition, it conducts a pre-reduction in size. The main reduction is done by a high-resolution microscope lens. The respective images of the shown system planes are visualized below.

The macro lens is an Optem video zoom lens that has a focal length from 18 up to 108 mm and a closed aperture F/2.5. The field stop, the zoom, and the focus can be adjusted manually [35]. The best combination of three field stops, seven focus lengths, and 12 zoom settings must be evaluated for using this lens in the lithography system. All settings are combined, and the respective resolution limits are evaluated by a MTF analysis. Further parameters such as the Field of View (FOV) are determined. The setting combinations with a resolution limit below the printing edge inaccuracy and the greatest FOVs up to 80 % of the illumination source's diameter will be analyzed again by taking the distortion into account. Finally, the optimum is evaluated with respect to the resolution, FOV, and less distortion-affected imaging. The reduction factor of the second system part is a function of the focal length ratio of the tube lens and the microscope lens. In the built lithography system, the tube lens has a focal length of 175 mm and the microscope lens' focal length is 8 mm approximately[1] which affects an assumed reduction factor of 0.046x. The pre-reduction unit is applied to multiply the main reduction factor. After the lithography system is built, the resolution and the reduction factor of each system unit and the total system will be measured by a MTF analysis and the imaging reduction.

[1]The real focal length of the Leica lens is not defined. The approximation is based on a comparable system that has a tube length of 160 mm and a resulting reduction of 0.04x. The calculation, 160 mm multiplied by 0.04, results in an approximated focal length of 8 mm.

4 Experimental results

According to the planned methodology in Chapter 3, the experiments are conducted. The commercial Canon iX6850 and the DMP 2850 are analyzed with respect to the minimal structure size and the edge quality. The lithography system's resolution limit is defined based on the printing edges' analysis. Subsequently, the photolithography system is set up in eight calibration steps. The results of each calibration step are dealt including the system power's measurement.

4.1 Printing Systems

4.1.1 Canon iX6850

Bar structures such as the bar groups of Figure 4.1 are printed by the Canon iX6850. There are three bars of each size perpendicular[1] to the printing direction. The different bar groups are arranged in a grid of multiple sub-inches [2] to support the RIP and achieve the highest resolution.

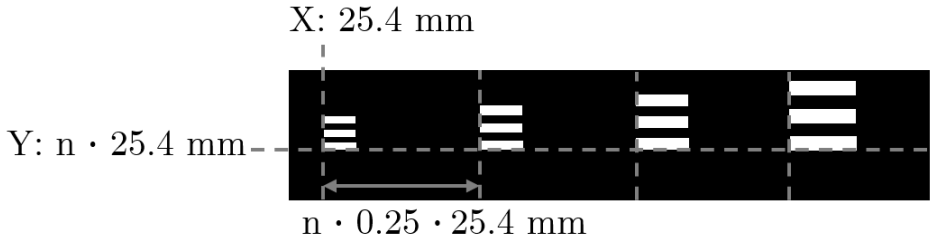

Figure 4.1: Structures' grid of the printed test patterns. The bars are oriented perpendicular to the printing direction. The bar groups' horizontal distance is a multiple of 0.25 · 25.4 mm. The vertical distance is a multiple of 24.4 mm.

Since structures larger than 60 µm are resolved, Figure 4.2 shows the measured bar size according to the respective digital bar size in a range from 60 µm up to 197.5 µm. In Figure 4.2 (a), the measured bar sizes of BK printed structures are

[1] The 9600 DPI can be achieved perpendicular to the printing direction. Therefore, this orientation is used to achieve the highest resolution.

[2] 1 inch = 25.4 mm

plotted. The measured bar size of PGBK printed structures are displayed in (b). Negative structures of PGBK ink in (b) are reliable identifiable if they are wider than 82.5 µm. Smaller bars do not always result in a complete bar structure due to the distribution of the ink. In the following the bar size, its reproducibility, the printing algorithm, and the impact of the ink type (BK: CLI-551BK and PGBK: PGI-550PGBK) will be discussed with respect to Figure 4.2.

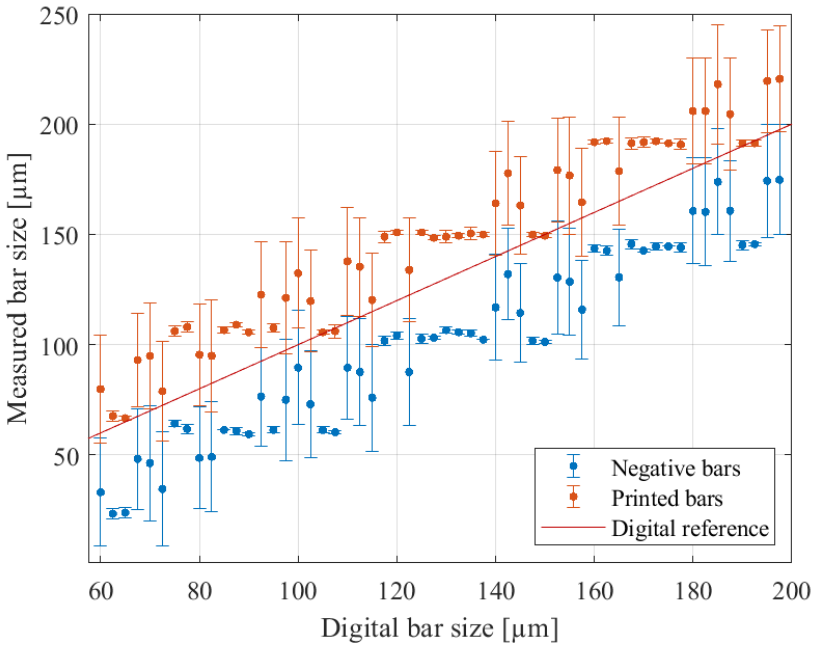

(a)

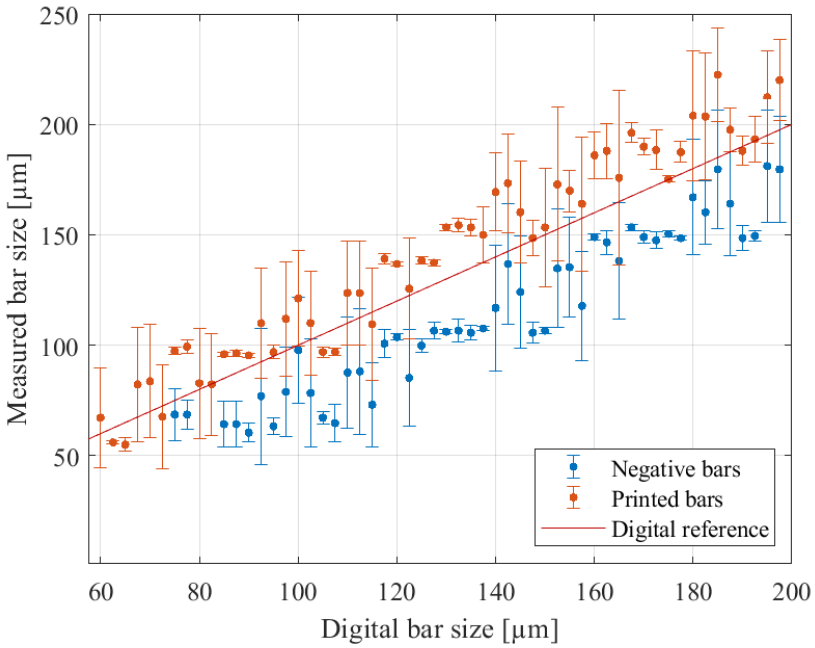

(b)

Figure 4.2: Measured bar sizes of the Canon iX6850 printed structures using BK ink (a) and PGBK ink (b). The negative bars (blue) tend to be smaller than the digital reference (red). In contrast, the printed bars (orange) are rather larger than the digital reference.

In general, printed structures are wider than the negative structures due to the ink spreading around the dot center as visualized in Figure 4.3. According to printed 125 µm structures of Figure 4.3, the printed structure size S tend to be wider than the digital reference Ref (a) and the negative structure S is smaller

than the expected reference *Ref* (b). If a predictable offset is known, the offset between the digital structure size and the printed structures can be adjusted in the digital layout.

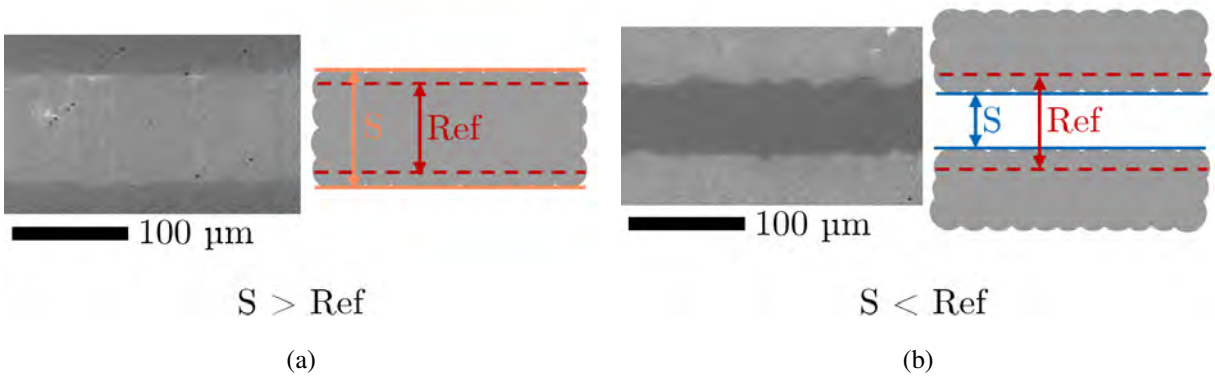

Figure 4.3: Impact of the structure printing type on the resulting structure size. Printed bars *S* tend to be larger than the reference *Ref* (a). In comparison, negative bars *S* are smaller than the reference *Ref* (b). The black ink is shown in a lighter gray tone than the unprinted areas on the WLI images.

As shown in Figure 4.2 (a), the standard deviation of the bar size depends on the digital structure size and affects printed structures and negative structures equally using the BK ink. This relation cannot be applied to structures printed with PGBK ink because the standard deviation's difference of printed structures and negative structures are conspicuous in Figure 4.2 (b). Therefore, the negative structures' images are compared as displayed in Figure 4.4. The reference structure size of 132.5 µm is printed with BK ink (a) and PGBK ink (b). Based on this, the variation of PGBK structures' standard deviation is primarily caused by the added ink pigments of the PGBK. The PGBK ink causes a rough printing edge and a greater standard deviation of the measured structure size.

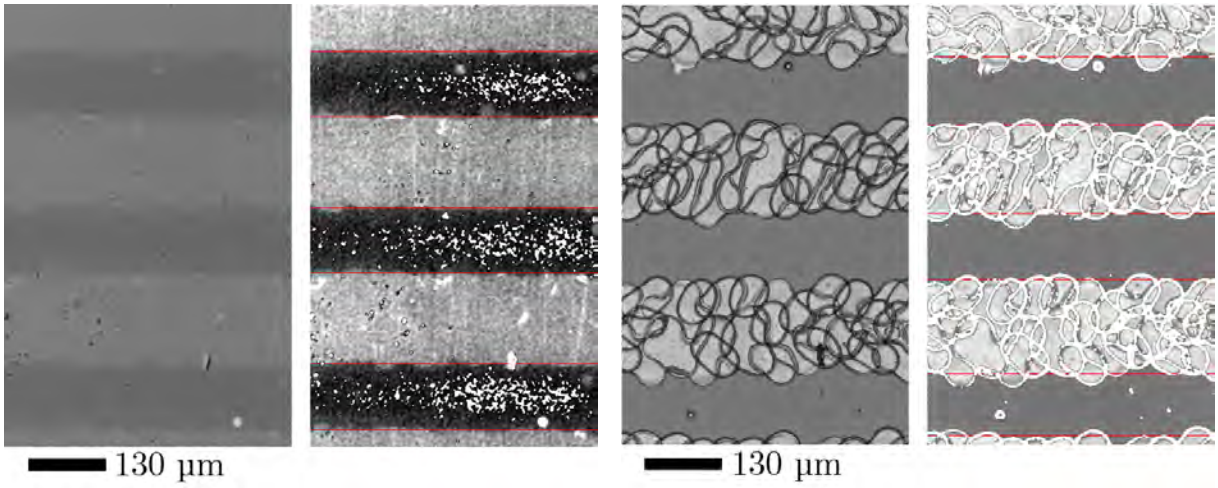

(a) (b)

Figure 4.4: Background printed structures of 132.5 µm reference size which are printed using a Canon iX6850 with BK ink (a) and PGBK ink (b). The respective WLI grayscale images are shown on the left side. The MATLAB analysis' images are displayed to the right. At this point, it must be noted that the dark ink is brightly visible on the WLI image. The dark edges of the PGBK ink are caused by outward reflected light, which is not captured by the WLI camera.

The BK printed structure size within a bar group varies greatly with respect to the standard deviation of Figure 4.2 (a). There are a few exceptions that have stagnant structure size, such as the measured bar sizes in a range from 125 µm to 137.5 µm and 167.5 µm to 177.5 µm. The PGBK printed structures of Figure 4.2 (b) have a similar characteristic including a higher standard deviation due to the mentioned pigments. All BK and PGBK printed structures are visually compared to investigate the standard deviations' source and algorithm of the RIP. The complete visual comparison is added to Appendix A. Based on this, two main statements can be derived.

First, the bar size discretization is similar using BK ink or PGBK ink as shown in Figure 4.5. The discretization causes a rounding up or down to an ink dot line. Having a precise printing edge, the standard deviation is repeatable if one bar of the group is smaller or larger by one ink dot line as demonstrated in Figure 4.2 (a). Secondly, it is assumed that the stagnant bar sizes are a superposition effect of the RIP due to the changing pattern of Figure 4.2 (a). Since the system's discretization, especially the RIP, is not known, the stagnant area and all structures with low standard deviation are defined as confidence ranges[3].

[3]Confidence ranges of BK printed structures: 62.5 µm - 65 µm, 75 µm - 77.5 µm, 85 µm - 92.5 µm, 97.5 µm, 105 µm - 107.5 µm, 117.5 µm - 120 µm, 12 µm - 137.5 µm, 147.5 - 150 µm, 157.5 µm - 177.5 µm, 170 µm - 172.5 µm.

Structures within a confidence range can be reproducibly printed. The smallest reproducible structure size is 23.4 $\pm$ 2.5 µm. It is achieved using the Canon iX6850 with BK ink and the negative reference structure of 62.5 µm.

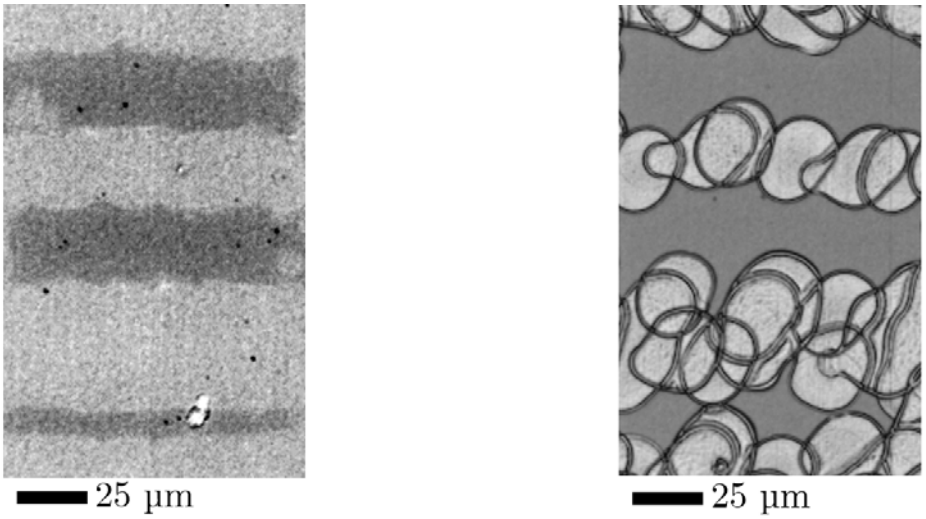

(a) (b)

Figure 4.5: Background printed structures of a 67.5 µm reference structure size based on BK ink (a) and PGBK ink (b). The structures are based on the same dot grid. The bars, which should have the same size, have a maximum discretization difference of one dot line.

In the next step of the Canon iX6850 system's analysis, the printed edge quality is investigated. The standard deviation of the printed edge's contour is calculated. The standard deviation of BK and PGBK printed edges are compared in Figure 4.6. The plots' data distribution supports the observation of Figure 4.4 that the PGBK inks' added pigments cause a rougher edge. The PGBK edges' roughness is more than twice times the BK edges' roughness, as it will be dealt with in detail.

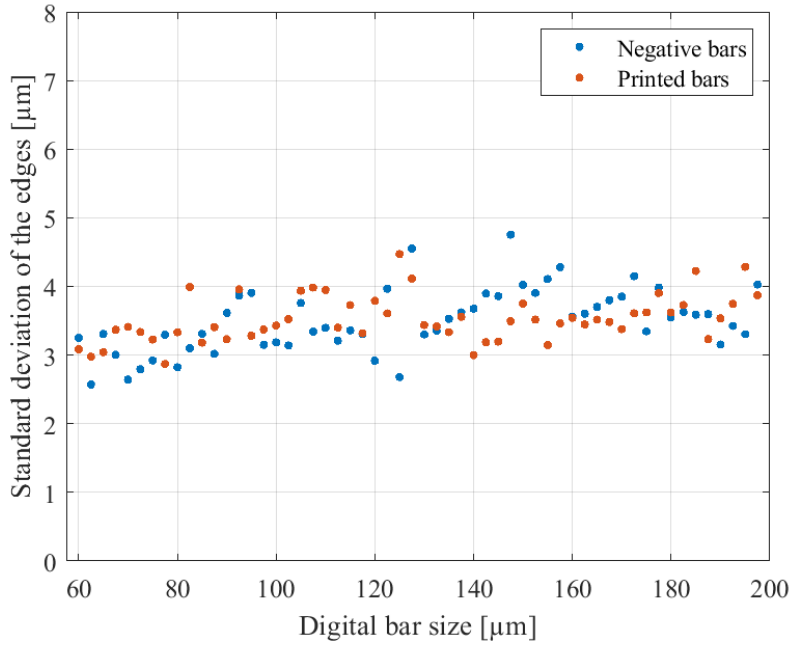

(a)

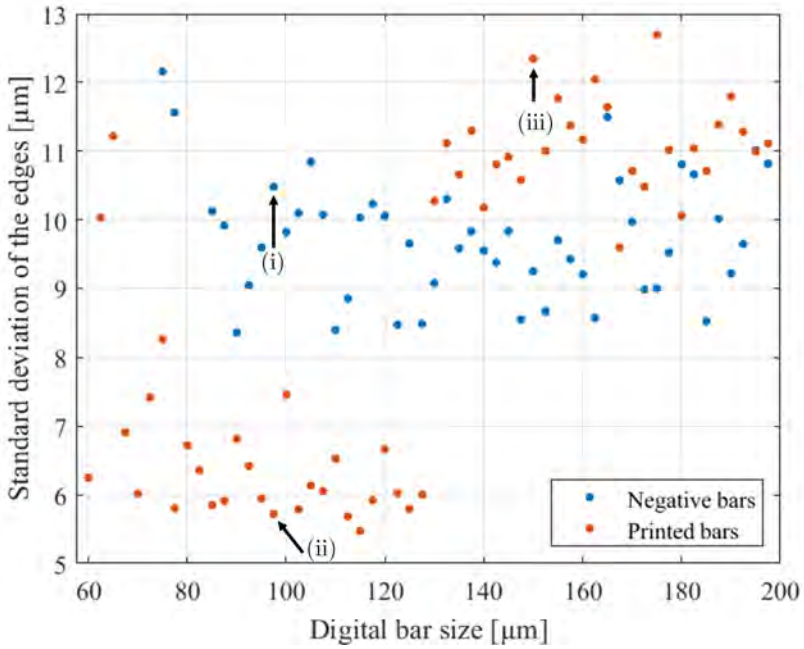

(b)

Figure 4.6: Analysis of the Canon iX6850 printed edges which are based on BK ink (a) and PGBK ink (b). The edge quality is quantified by the standard deviation of the edges' contours. In general, three cases (i), (ii), and (iii) are distinguished and discussed. The first case is about negative PGBK printed structures (i). The second (ii) and third (iii) case refer to printed structures which are smaller than 127.5 µm (ii) and larger than 127.5 µm (iii). For example, the respective images of the arrowed data points are shown in Figure 4.7.

In contrast, the PGBK printed edges are affected by the structure type and bar size. Three cases can be distinguished based on Figure 4.6 (b). In the first case (i), negative PGBK structures have a relatively consistent standard devia-

tion of 9.7 ± 0.9 µm. This means that the PGBK printed edges are about 2.7 times rougher than BK printed edges. The second case (ii) covers the PGBK printed bars up to a bar size of 127.5 µm. These PGBK edges have a lower mean standard deviation of 6.6 ± 1.3 µm. The third case (iii) is defined by the standard deviation of PGBK printed edges which are wider than 130 µm. Those edges' standard deviation increases significantly to a mean standard deviation of 11.1 ± 0.7 µm. A representative structure of each case is visually compared as shown in Figure 4.7 to find the deviation's source. The imaged edges of Figure 4.7 confirm the quantitative analysis that printed edges of the first case (a) and third case (b) are the roughest ones. In comparison, the 97.5 µm structure of (b) consists of multiple single ink dots. Larger printed areas such as the printed background of (a) or the bars of (c) have more merged areas and the single ink dots are no longer identifiable. The increasing ink density in more printed areas is one possible explanation for the rougher edges. Since the BK printed structures have almost a twice time better edge quality and the minimal reproducible structure size is printed using BK ink, the PGBK printed structures are no longer investigated. The mean standard deviation of 3.5 ± 0.4 is used as the quantity of the Canon iX6850 printer's edge quality.

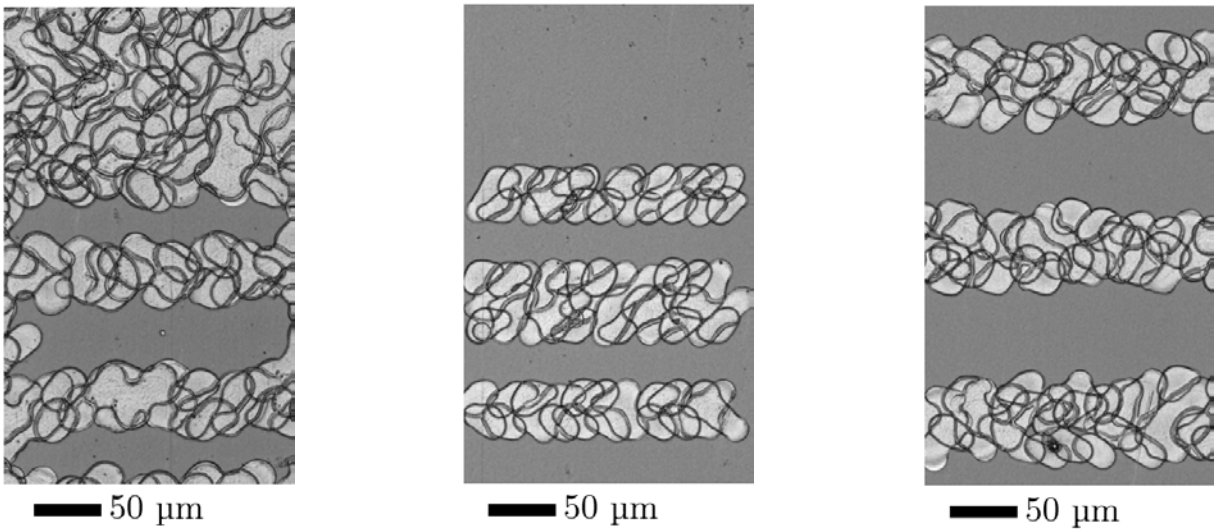

(a) (b) (c)

Figure 4.7: Images of PGBK printed structures with a bar size of 97.5 µm (negative structures) (a), 97.5 µm (printed bars) and 150 µm (printed bars) (c). The printed edges of (a) and (c) are rougher than the edges of (b).

4.1.2 Dimatix 2850

All structures of the DMP 2850 analysis are printed with a Dimatix black test ink. The most precise drop spacing of the DMP 2850 is evaluated by printing three 100 µm bars of each relevant spacing and measuring the edge quality. The drop spacing is set to 10 µm (2540 DPI) and 15 µm (1270 DPI)[4]. The edge quality is measured by the standard deviation of the printed edges' contours as applied previously. Using a drop spacing of 10 µm, the edges' standard deviation is ± 4.3 µm. More precise edges with a standard deviation of ± 2 µm can be printed using a 15 µm drop spacing. Therefore, a 15 µm drop spacing is used.

The smallest reproducible structure size of the DMP 2850 is investigated similar to the Canon printer's analysis. The results of the measured structure sizes are shown in Figure 4.8. Structures sizes, which are at least 45 µm, can be resolved. Therefore, the bar sizes from 45 µm up to 135 µm are measured [5]. According to the results shown in Figure 4.8, the smallest reproducible structure is 18.1 ± 2.0 µm. In comparison, the smallest reproducible structure size of the Canon printer using the BK ink is 23.4 ± 2.5 µm with respect to Figure 4.2. It is possible to print smaller and more reproducible structures using the DMP. The ratio of the printed structure and the digital bar size is linear as demonstrated by the fitted curves. The mean offsets of +27.5 (± 1.2) µm and - 25.7 (±0.9) µm can be taken into account in the digital layout to improve the precision of the structure widths.

[4]Further drop spacing settings are excluded according to a visual check and a detected insufficient print quality.
[5]The analysis of greater bar sizes is not necessary due to the constant printing characteristic.

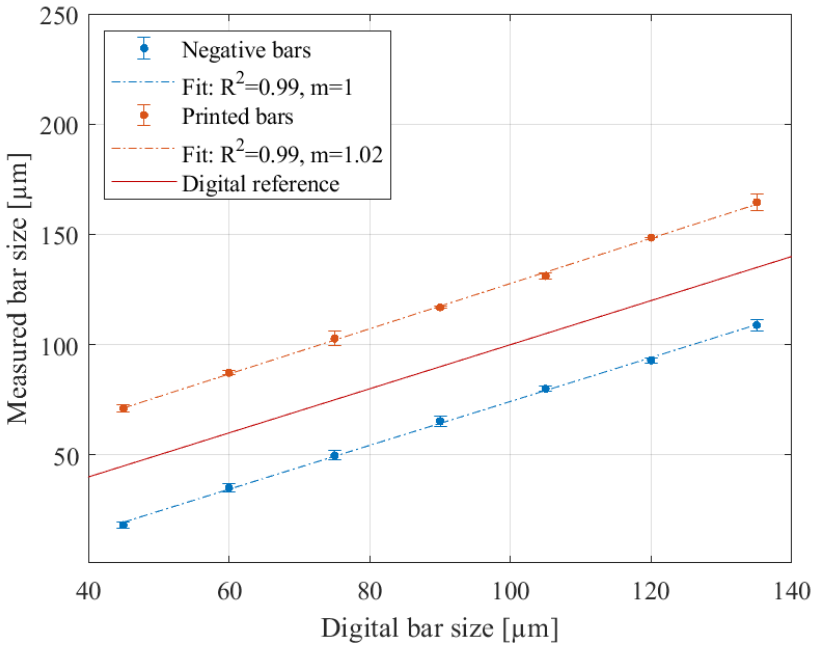

Figure 4.8: Measured bar sizes of the DMP 2850 printed structures using the Dimatix test ink. The blue error bars refer to the negative structures and the orange error bars are based on the printed structures. The digital bar size of the printing layout is plotted as a reference (red).

The printed edges' quality is evaluated based on Figure 4.9 which shows the standard deviation of the printed edges' contours. The bar size has no impact on the edge quality with respect to Figure 4.9. The mean standard deviation is 2 ± 0.3 µm. This is almost the half of the Canon printer's roughness[6].

[6]The Canon iX6850 edges' standard deviation is 3.5 ± 0.4 µm based on Figure 4.6 (a).

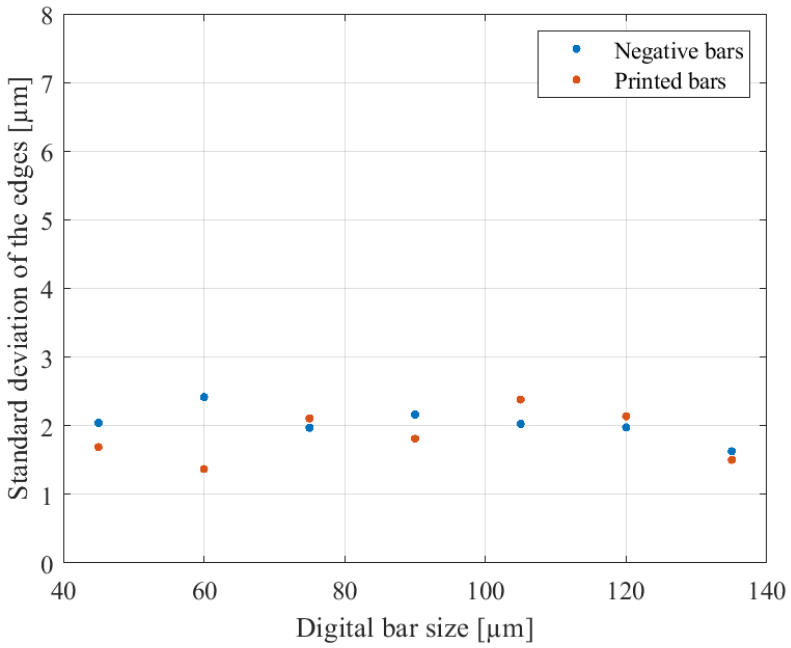

Figure 4.9: Analysis of the DMP 2850 printed edges. The edge quality is quntified by the standard deviation of the edges' contours. In comparison to Figure 4.6, the vertical dimension is shifted by 3 µm. The increments are still the same.

4.1.3 Printer Comparison and Determination of the Lithography System's Resolution Limit

The results of the printing systems' analysis are summarized in Table 4.1. According to this, the DMP is able to print a 22.7 % smaller reproducible structure size and more precise edges. Therefore, the photolithography system's construction is calculated with respect to the DMP's inaccuracy.

Table 4.1: Comparison of the printing systems' analysis results.

	Smallest reproducible structure size [µm]	Edge quality (standard deviation) [µm]
Canon (BK ink)	23.4 ± 2.5	± 3.5
DMP (15 µm drop spacing, test ink)	18.1 ± 2.0	± 2.0

The inks dots of the photomask's edges should not be visible. Based on the demonstrated concept in Figure 3.2, the photolithography system's resolution

limit must be below the structure size of the edges' ink dots to result in a blurred image. If the inaccuracy is normally distributed as assumed, then $\pm$ 3 times the standard deviation σ covers 99.7 % of the inaccuracy as visualized in Figure 4.10.

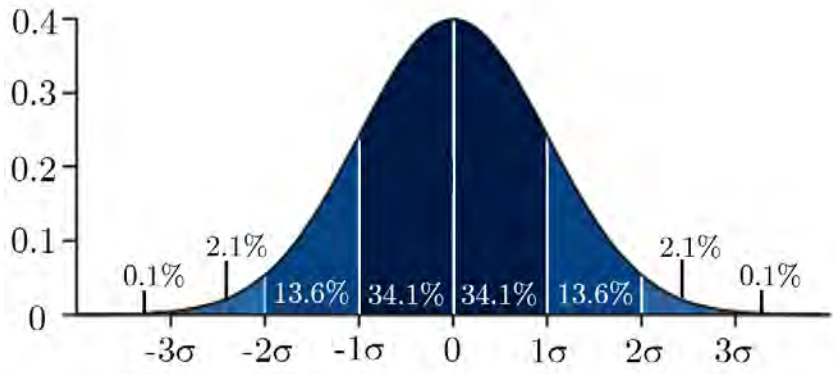

Figure 4.10: Visualization of the normal distribution and the σ ranges. The first σ is calculated by the standard deviation of the measurement data.

The total inaccuracy I_t is 12 µm as given in Equation 4.1.1.

$$I_t = 3 \cdot (\pm\sigma) = 3 \cdot (2 \cdot 2\ \mu m) = 12\ \mu m \tag{4.1.1}$$

The resolution limit of the lithography system is calculated based on the total inaccuracy I_t and equals 83.88 lp/mm. Equation 4.1.2 displays the rearranging.

$$I_t = 12\ \frac{\mu m}{lp} = \frac{1}{0.012}\ \frac{lp}{mm} = 83.33\ \frac{lp}{mm} \tag{4.1.2}$$

4.2 Photolithography System

The final photolithography system is captured in Figure 4.11. A photo of the built system is shown in Figure 4.11 (a). For a examination in detail, the system is illustrated with dimensions, image path (blue), as well as illumination path (red) in (b) and (c). In (c), the dashed framed system units of (b) are illustrated. The system consists of a horizontal lithography system and a vertical camera system which will be used to focus onto substrates. The beam of a 405 nm LED

(M405L3-C4, Thorlabs [60]) is widened by a KEPLER telescope (D=24.5 mm f=35 mm N-BK7, D=24.5 mm f=150 mm N-BK7, Thorlabs [55], [57]) to image the light source into the macro lens' (Macro Video Zoom Lens 18-108 F/2.5, Optem) field stop and generate a homogeneously illumination in the substrate plane. The macro lens captures the photomask and images the photomasks' structures in the intermediate image. The intermediate image is imaged to infinity by the tube lens[7] (D=24.5 mm f=175 mm N-BK7, Thorlabs [56]). A beam splitter (Non-polarizing beamsplitter cube 400-700 nm, Thorlabs [59]) directs the image and illumination path downward. The microscope lens (HC PL FLUOTAR 20x/0.50, Leica) images the intermediate image via the tube lens and the beam splitter onto the substrate. The substrate positioned by a three-axis stage (x and y stage M-531.PD, z stage M-501.DG , Physik Instrumente (PI) [38], [39]). If the substrate is illuminated by the lithography system's illumination or the mask image is reflected on the substrate, the camera system captures the substrate plane as shown in (c) with respect the drawn arrows. The beam to the right of the beam splitter are absorbed and excluded from the system. The camera system is based on a lens (MLH-10x, Computar [9]) which image the substrate plane on a camera sensor (mvBlueFox-1100G, Matrix Vision [31]).

[7]The deviation from the measured distance of 171.8 mm to the expected focal length of 175 mm is within the tolerance due to the macro lens' depth of focus and the tube lens' real focal length of 174.4 $\pm$ 1.7 mm [56].

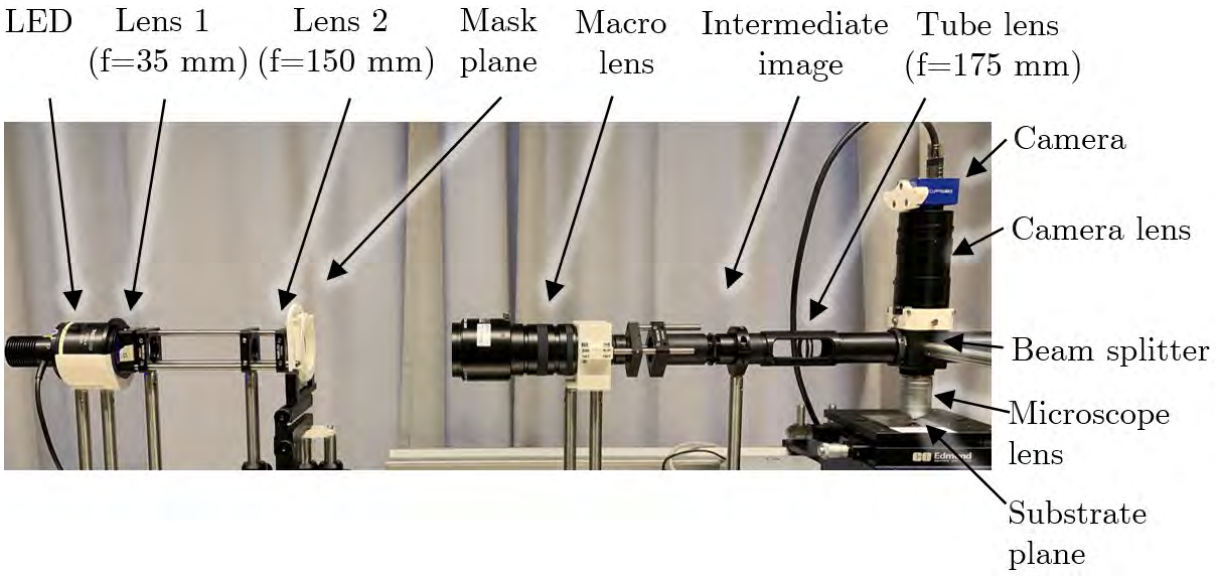

(a)

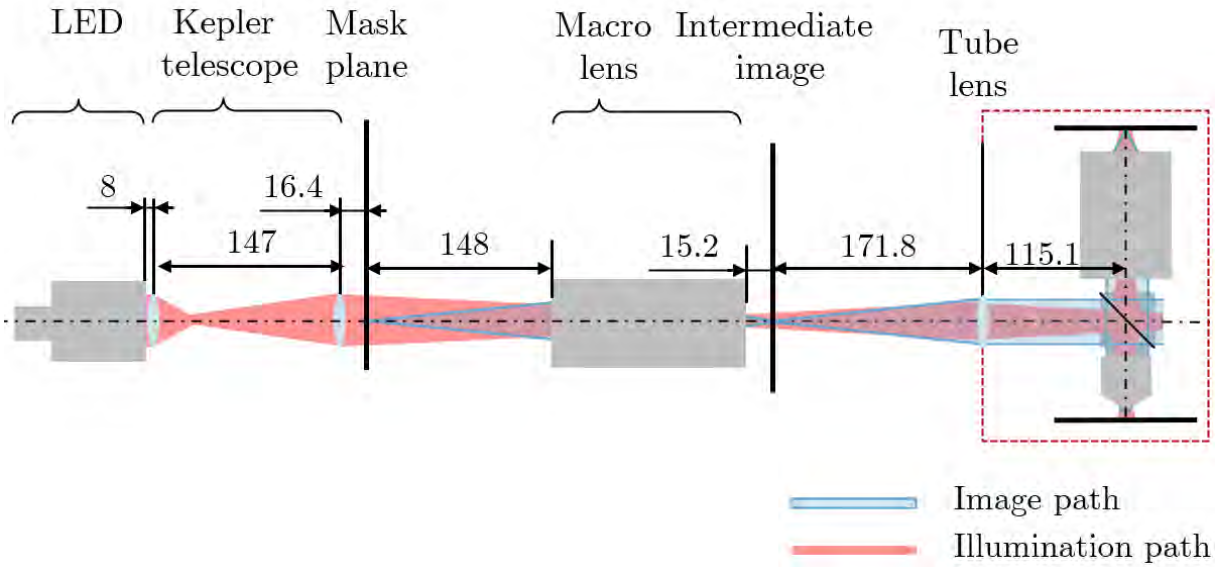

(b)

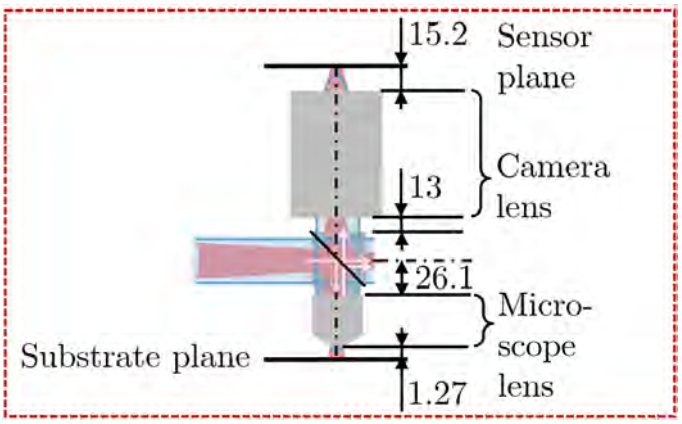

(c)

Figure 4.11: The system is based on a horizontal lithography system and a vertical camera system which will be used to focus onto substrates. The labeled photo in (a) displays the system. The respective drawing in (b) and (c) shows the dimensions in [mm], the image path and the illumination path of the lithography system.

The main assembly steps of the shown photolithography system such as the determination of the most optimal macro lens setting in Chapter 4.2.1, the adjustment of the system units[8] in Chapter 4.2.2, and the measurement of the illumination power in Chapter 4.2.3 are dealt with.

4.2.1 Determination of the Most Optimal Macro Lens Setting

The setup of the macro lens' investigation is visualized in Figure 4.12 (a). A 405 nm LED illuminated the USAF chart along the optical axis. The sensor captures the image of the macro lens. The different settings are labeled on the lens as shown in Figure 4.12 (b). The achieved resolution of three field stop setting ($f1$, $f2$, $f3$), seven working distances f_w (148-198 mm), and 12 zoom settings ($z1 - z12$) are analyzed by the images' MTF. The resolution is determined by a resolution threshold at a contrast of 0.2. A table of all MTF analysis results is shown in Appendix B. The respective FOV is the product of the sensor's image diameter d and the lens's transversal magnification factor.

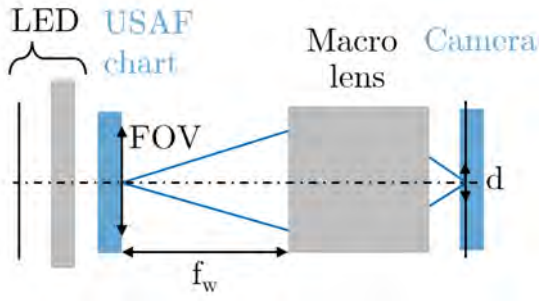

(a)

(b)

Figure 4.12: Experimental setup the macro lens' analysis with respect to resolution and FOV. In this experiments the USAF chart is illuminated by a LED along the optical axis and a camera captures the macro lens's image (a). The different settings are labeled on the macro lens (b).

The results of the macro lens' analysis are plotted in Figure 4.13. Settings, which achieve a relatively great FOV, are more useful since a greater mask area can be imaged. The resolution tends to be lower if the FOV is greater. Therefore, the settings for further experiments are restricted by the FOV-resolution ratio. Only settings, which are above the black dashed lines, are considered. In

[8]The adjustment of the camera system will not be discussed in detail since it was developed within a intership semester by Adrian Dannhauer.

addition, the FOV is limited by the illumination's diameter. Based on the LED diameter with an added safty factor, the FOV is limited to 35.2 mm as shown by the red dashed line. The resolution must be below the determined resolution limit of 83.33 lp/mmm to image the printed edges blurred according to the theory of Figure 3.2. Eight usable settings remain by applying the mentioned constraints as shown by the blue box of Figure 4.13.

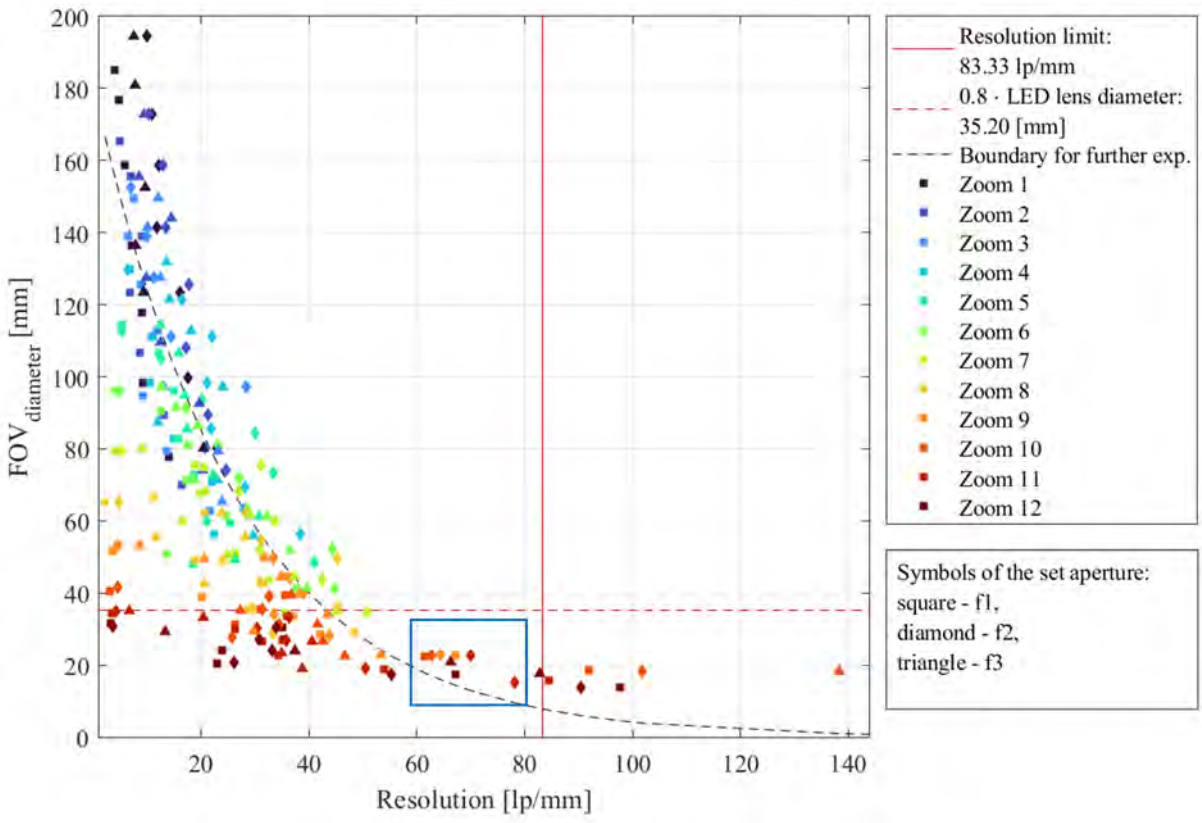

Figure 4.13: Results of the macro lens' analysis with respect to the FOV and the resolution of the respective macro lens' setting. The settings for further investigation are constrained by the FOV-resolution ratio, the maximal FOV, and the determined resolution limit.

The images of the chosen eight settings are analyzed with respect to the distortion. In this experiment, 8/6- and 6/5-grid-based point test patterns[9] are illuminated by a 405 nm LED as shown in Figure 4.14 (a). The captured images are evaluated by the absolute radial distortion. It is measured by the difference of the master and measurement center points as demonstrated in Figure 4.14 (b).

[9]Different point test pattern are applied to fill in the whole FOV as much as possible and achieve the most precise results.

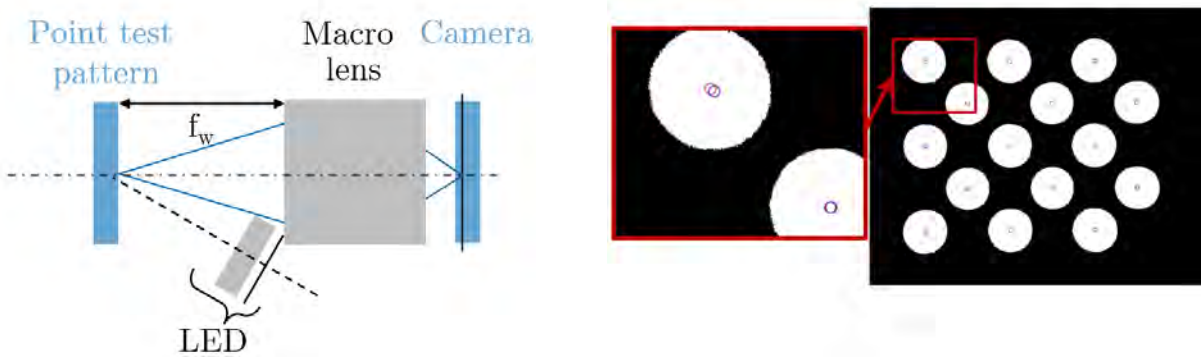

(a) (b)

Figure 4.14: The setup of the distortion measurement is based illuminated point test pattern and macro lens' image is captured by a camera (a). The automatized evaluation calculates the absolute radial distortion (b).

The measured absolute radial distortion, as a function of the radius from the image's center point, is plotted in Figure 4.15. The maximal distortion is measured at the maximal radius. The maximal radius is defined by the maximal sensor size in the image plane of 6.01 mm. Two settings ('f1, f_w=173 mm, z12' and 'f2, f_w=148mm, z11') are noticeable since their respective distortion is 5 and 9 times greater than the minimal distortion of 0.18 mm ('f2, f_w=148mm, z9').

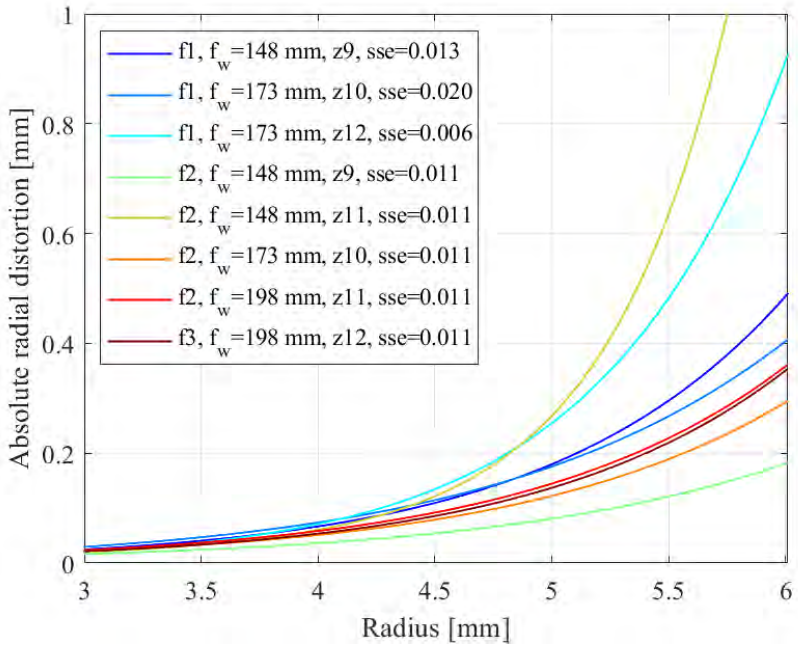

Figure 4.15: The absolute radial distortion increases in correlation to the radius. The yellow and turquoise graphs of 'f1, f_w=173 mm, z12' and 'f2, f_w=148mm, z11' reach 5 and 9 times greater maximal distortion than the minimal distortion of 0.18 mm.

The eight pre-chosen settings are numerically compared in Table 4.2. As observed, the distortions of samples 3 and 5 are disproportionately larger in comparison to sample 4. Since the distortion of sample 3 is 5 times as well as the distortion of sample 5 is 9 times greater and the resolution is almost the same [10], these settings are excluded from the further discussion about the most optimal setting.

Table 4.2: Preset optem settings based on resolution, FOV, and distortion.

Sample No.	Aperture f1-f3	Working distance f_w [mm]	Zoom z1-z12	Resolution [lp/mm]	FOV_{dia} [mm]	Max. distortion mm at r=6.01 [mm]
1	1	148	9	67.22	22.74	0.49
2	1	173	10	61.48	22.56	0.41
~~3~~	1	173	12	67.27	17.48	0.93
4	2	148	9	64.50	22.88	0.18
~~5~~	2	148	11	78.10	15.16	1.62
6	2	173	10	62.77	22.74	0.3
7	2	198	11	69.91	22.56	0.36
8	3	198	12	66.29	20.86	0.35

The parameters of the remaining settings are normalized to 1 and plotted in the spider diagram of Figure 4.16. The greater the area *a* is, the more suitable is the chosen macro lens setting. The setting of the green plotted sample ('f2, f_w=148mm, z9') has the greatest area of 0.631 and will be used in the lithography system.

[10] The respective resolution is rounded 1.0 and 1.2 times greater. Therefore, it is assumed that it is almost the same.

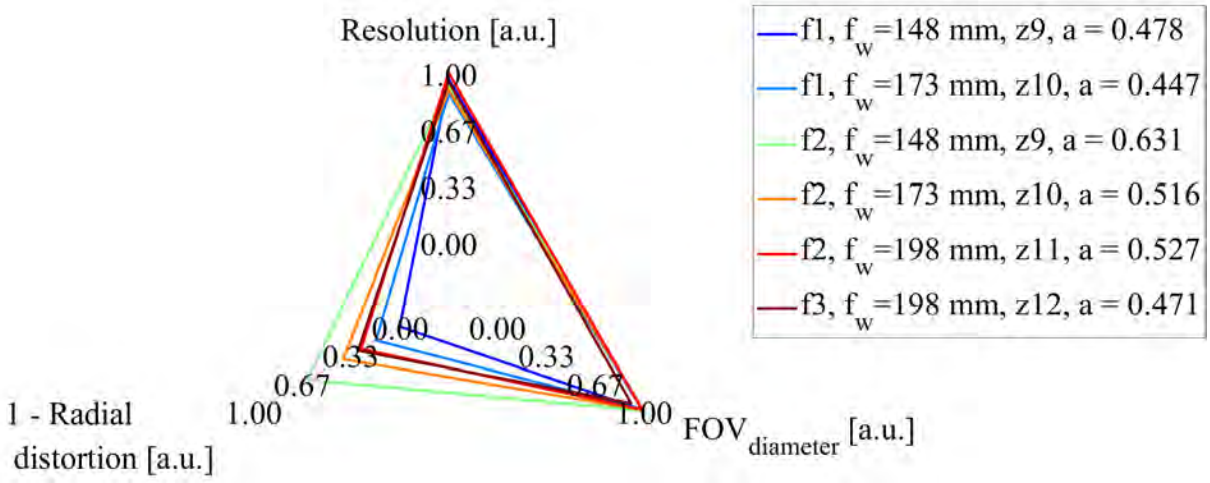

Figure 4.16: Comparison all pre-chosen macro lens settings to evaluate the most optimal setting for the lithography system's setup with respect to resolution, FOV, and distortion. Since the green plotted setting has the greatest spun area, it is used in the lithography setup.

4.2.2 Adjustment of the System Units

4.2.2.1 Focusing the Macro Lens

The determined macro lens setting ('f2, f_w=148mm, z9') is applied as shown in Figure 4.17. First, the blue imaging path is considered. The macro lens is positioned 148 mm behind the mask plane and its focus is adjusted using the camera in the image plane. The same plane is located 15.526 mm behind the c-mount thread. The USAF chart is illuminated by the LED and is imaged on the camera sensor along the optical axis. The focal plane is determined visually on the basis of the USAF chart's image. An evaluation of the focus is made by a MTF analysis in Chapter 4.2.2.7.

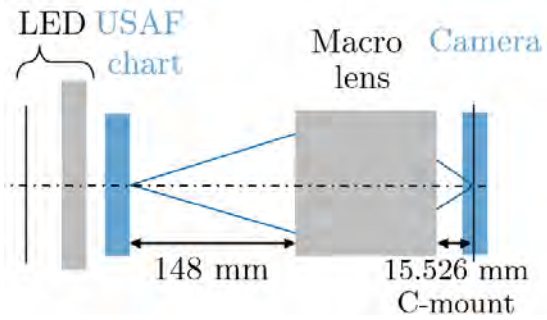

Figure 4.17: The macro lens focusing is done using the camera system which is placed into the image plane. The LED illuminates the USAF chart in the mask plane.

4.2.2.2 Determination of the Tube Lens Position

The focal plane of the tube lens is positioned at the image plane of the macro lens to image the mask structure to infinity. Therefore, the distance between this intermediate plane and the tube lens is 175 mm. The precise adjustment is done using a Wavefront Sensor (WFS) as shown in Figure 4.18. The LED beam is focused by a 35 mm positive lens onto a 10 µm pinhole. The pinhole approximately generates a point light source which will be imaged to infinity by the tube lens. The imaging to infinity is equal to a plane wavefront in the ideal case. The tube lens is adjusted by placing it in the position where the wavefronts Root Mean Square (RMS) error is minimal.

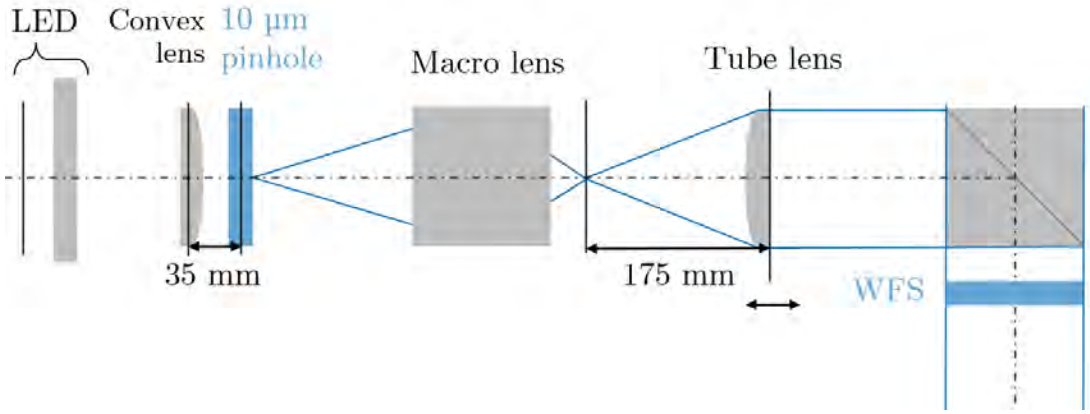

Figure 4.18: The tube lens of the lithography system images the intermediate image to infinity. Therefore, the tube lens' focal point must be precisely located in the intermediate plane. The most optimal tube lens position is adjusted by a wavefront analysis with a WFS.

The RMS error is calculated as given in Equation 4.2.1 [58]. The difference from each measurement point i to the mean value is defined as x_i. The mean RMS error of the final tube lens position is 0.596 ± 0.056 µm. The respective wavefront and the measurement data are added to Appendix C.

$$RMS_{error} = \sqrt{\frac{1}{n}\sum_{i=1}^{n} x_i^2} \tag{4.2.1}$$

4.2.2.3 Illumination Adjustment by LED Movement

The goal of the illumination adjustment is a homogeneous illumination in the substrate plane due to a well-positioned LED light source. As shown in Figure

4.19 (a), the LED is based on an (aspherical positive) lens and a LED chip. In the first adjustment step, it is assumed that the LED chip can be approximated by a point source. This point source should be imaged in the aperture of the microscope lens to affect a homogeneously illuminated substrate plane. In the adjustment setup of Figure 4.19, the illumination path is reversed and a pinhole is placed in microscope's aperture plane. The LED lens housing is initially positioned directly behind the mask since this maximizes the illuminated area. If the inserted pinhole is illuminated by a LED, the pinhole is imaged via the beam splitter, the tube lens, the macro lens, and the LED lens behind the LED lens as demonstrated in Figure 4.19. The position of this image correlates to the most optimal position of the point light source. The manually measured position of an ideal light source is 3.7 mm within the LED housing as drawn in Figure 4.19 (b).

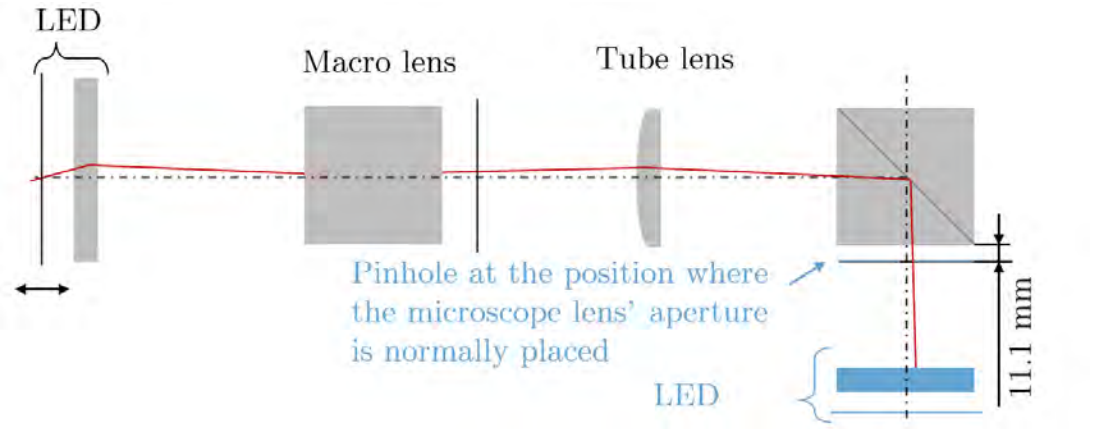

(a)

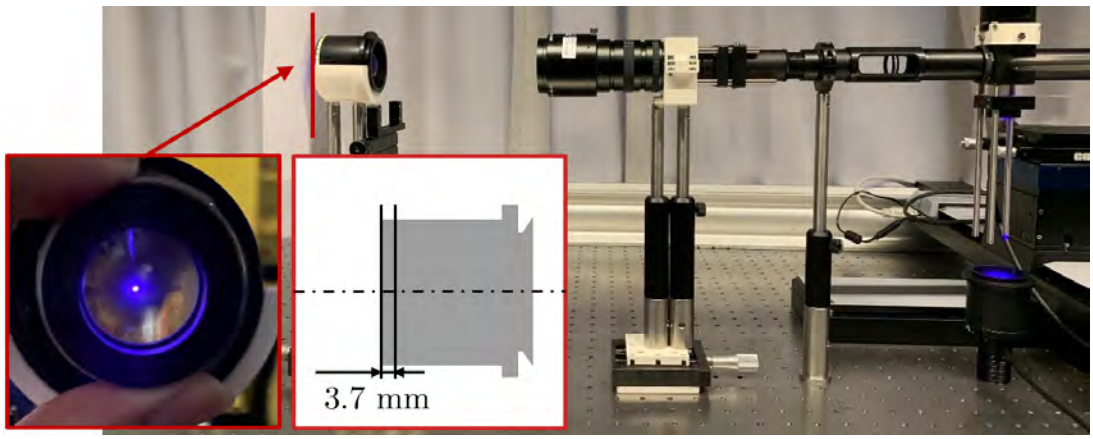

(b)

Figure 4.19: The lithography system is reverse illuminated to determine manually the position of the LED chip. The LED chips' position is defined by the smallest pinhole's diameter of its image. The experimental principle is illustrated in (a) and the respective photo in (b).

Subsequently, the precise adjustment of the illumination is conducted as shown in Figure 4.20. The Microscope lens is positioned below the beam splitter and its image is captured by a camera. The LED chip is mounted on a stage in the determined distance of 3.7 mm to the LED lens housing. The LED chip is moved precisely for the most homogeneous illumination in the substrate plane using the illumination distribution on the camera sensor.

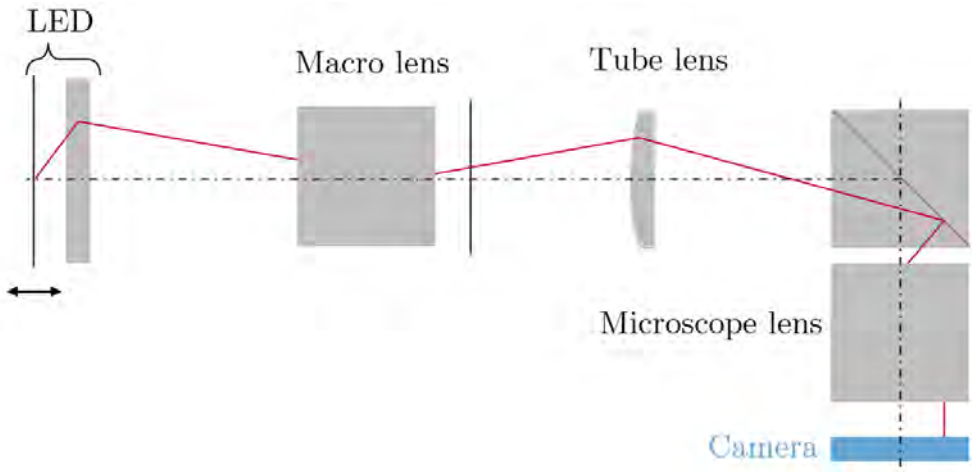

Figure 4.20: The precise adjustment of the illumination is conducted by moving the LED chip and capturing the illumination distribution in the substrate plane.

Using the setup of Figure 4.20, the LED chip is blurred imaged in the substrate plane as shown in Figure 4.21 (a). Small and large displacement of the LED chip only result in a change in size of the image. There are two possible causes for this observation. Either the light source is not imaged in the aperture plane of the microscope lens or the led chip cannot be approximated with a point source. A screen has been placed in the aperture plane to check the imaging of the light source as shown in Figure 4.21 (b). Since the LED chip is imaged in the aperture plane, it is verified that the led chip can not be assumed to be a point light source in this application.

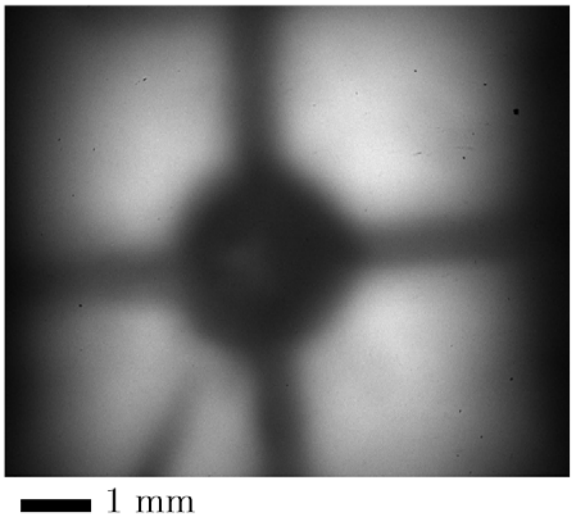

(a)

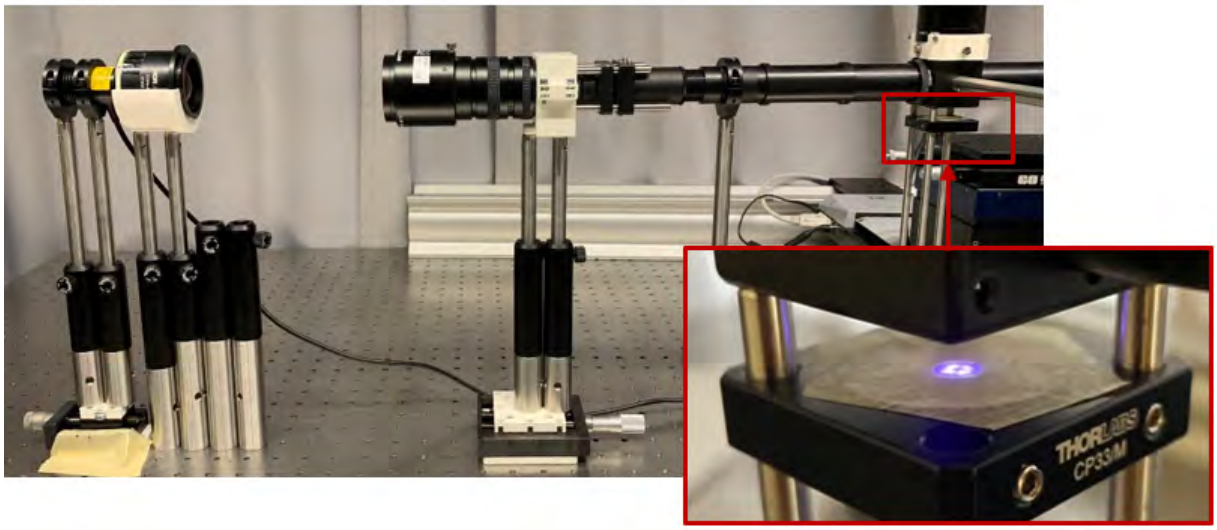

(b)

Figure 4.21: The illumination homogeneity in the substrate plane is not acceptable due to the imaged LED chip (a). Although, the light source is imaged in the microscope lens' aperture plane (b). It is deduced that no homogeneous illumination of the substrate plane can be generated by the planned adjustment process since the LED chip can not be approximated as a point light source.

The LED is moved backward to avoid the imaging of the light source in the substrate plane as illustrated in Figure 4.22. The setup is not further modified. The illumination distribution in the substrate plane is evaluated by the usable area. The illumination threshold of the measured usable area is defined by the STREHL criteria as given in Equation 4.2.2. An image area is considered if the relative intensity I exceeds 0.6 [16]. In this analysis, the distance d between the LED housing and the mask plane is increased from 18.8 mm up to 93.8 mm. It is observed that the substrate plane is symmetrically illuminated as displayed

in Figure 4.23 (a). There is vignetting at the spot edge. Since all illumination distributions at different distances d are affected by vignetting as shown in Appendix D, the distance has no impact on the vignetting in the analyzed range. Vignetting indicates a beam's escape or its cut off in the lithography system. Two possible error sources are illustrated by the dashed red line in Figure 4.22. The beam could be cut off by the macro lens' aperture and the exit angle σ' could cause a partial escape of the beam.

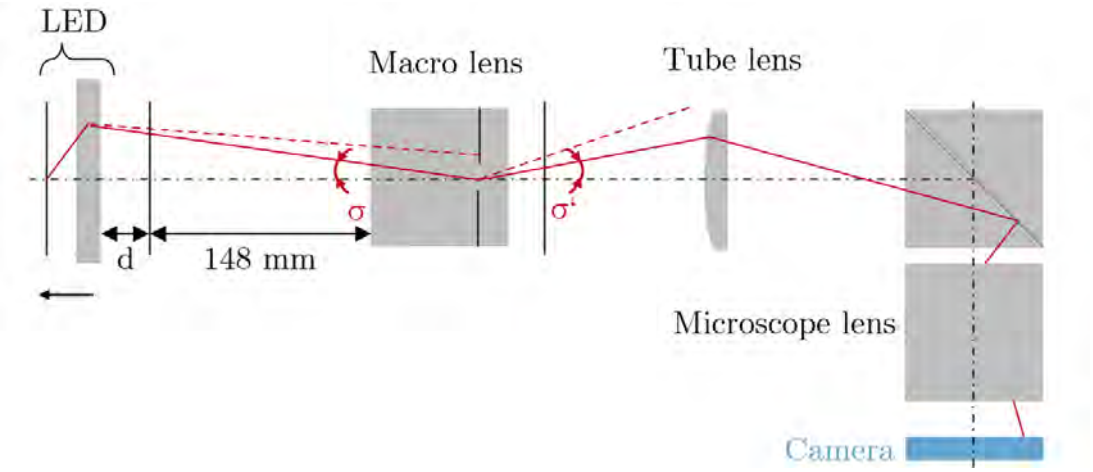

Figure 4.22: The distance d between the mask plane and the LED is increased in 5 mm steps to analyze the intensity distribution in the substrate plane. The dashed lines indicate possible error sources of vignetting in the substrate plane. The beam could be cut off by the macro lens' aperture and the opening angle σ' could cause a partial escape of the beam.

The measured usable area as a function of the LED distance d is plotted in Figure 4.23. The usable area tends to increase with an increasing distance. It does not exceed 0.22 mm^2 within the distance range of 18.8 mm up to 93.8 mm. The resulting usable area is directly related to the system error that causes the vignetting due to the beam's cut off. If the source of the vignetting is eliminated, the usable area will increase.

$$D_s = \frac{I_{real}}{I_{ideal}} > 0.6 \tag{4.2.2}$$

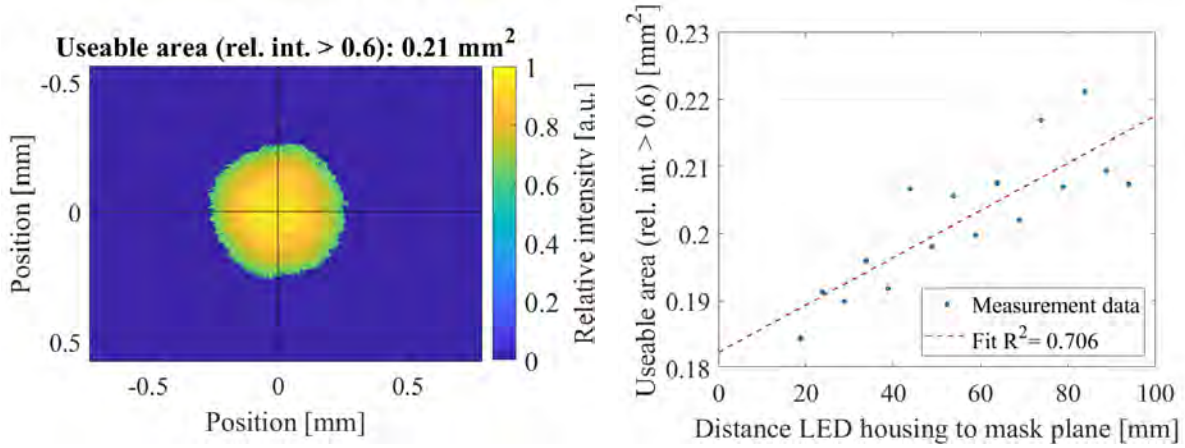

(a) (b)

Figure 4.23: The analysis of the illumination homogeneity and the usable area is based on the relative intensity (a) and the increasing distance from the LED housing to the mask plane (b). The displayed illumination distribution in (a) is captured at a LED distance of 63.8 mm.

According to the analysis results of the illumination by moving the LED, the homogeneity and the useable area could be improved by reducing the vignetting. A increased illumination incidence angle σ, which focuses the illumination in the macro lens' aperture plane, minimizes the beam's cut off. An increased incidence angle causes a decrease of the exit angle σ' [11] and avoids the beam's partial escape. An optical integrator [63], [64] or KEPLER telescope can be used to change the incidence angle and improve the illumination in the substrate plane, for example.

4.2.2.4 Illumination Adjustment by Kepler Telescope

A KEPLER telescope is applied between the LED and the mask plane to change the incidence angle and improve the illumination in the substrate plane by increasing the homogeneity and the useable area. The modified setup using the KEPLER telescope is shown in Figure 4.24. The first lens (f=35 mm) focus the beam at a short distance. The original beam is widened due to the more distant second lens (f=150 mm). The moving of the second lens determines the beam's diameter and focus. The focal point in the macro lens must be estimated since it is not possible to determine the aperture plane and the beam path in detail. The adjustment is done by optimizing the illumination distribution in the substrate plane, which is measured with a camera.

[11] The real relation between the incidence angle and the exit angle is not shown in the simplified illustration of Figure 4.22.

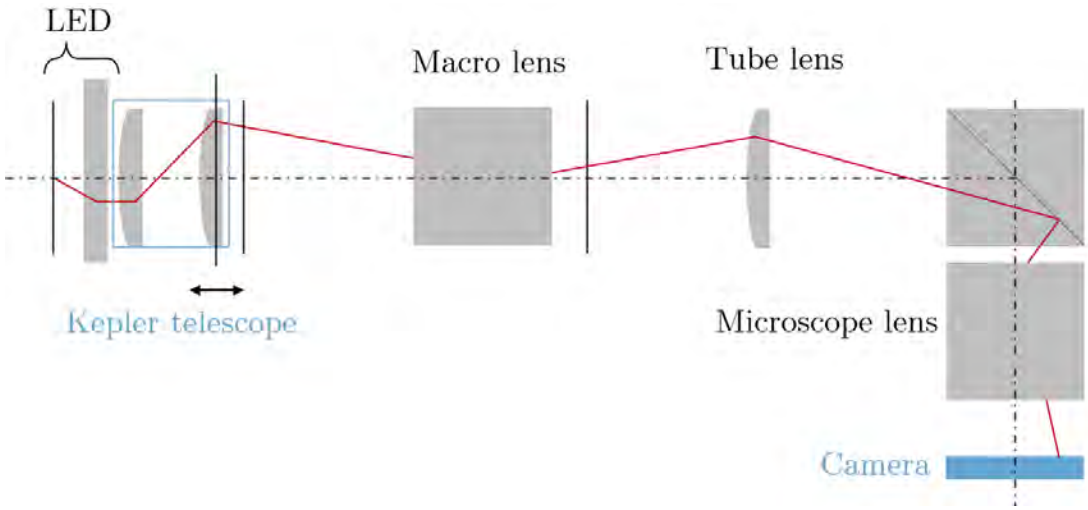

Figure 4.24: The lithography system is modified using a KEPLER telescope to improve the illumination in the substrate plane. A camera measures the intensity distribution in the substrate plane.

The analysis results[12] of the achieved illumination in the substrate plane is shown in Figure 4.25. No vignetting can be observed according to Figure 4.25 (a). In comparison, the STREHL-based usable area has doubled using the Kepler lens. Instead of maximal 0.22 mm^2, an area of 0.43 mm^2 can be used for exposure. This is equal to a spot diameter of 0.72 mm. In addition, the homogeneity is evaluated based on the Full Width Half Maximum (FWHM) of the GAUSSIAN-fitted relative intensity distribution of the useful area as shown in the histogram of Figure 4.25 (b). The spot area is more homogeneous illuminated, if the FWHM is smaller. The FWHM without using the KEPLER telescope is 0.40 $\pm$ 0.04 with respect to Appendix D. In contrast, this is two times the improved system's FWHM 0.19 $\pm$ 0.01.

[12]The given standard deviation is calculated based on 16 samples which are add to the Appendix E.

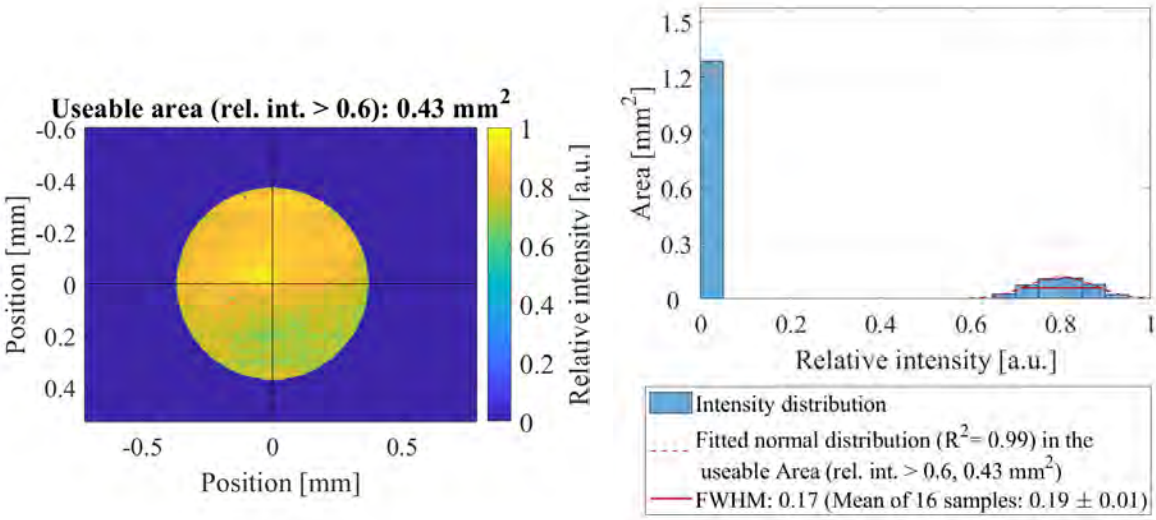

(a) (b)

Figure 4.25: The analysis of the illumination homogeneity and the usable area using a KEPLER telescope is based on the relative intensity (a) and the respective FWHM of the fitted normal intensity distribution (b). The fitted GAUSSIAN distribution refers to the measured relative intensity in a range from 0.6 up to 1.

4.2.2.5 Assembly of the Lithography and Camera System

As mentioned, a vertical camera system is used to adjust the lithography system as illustrated in Figure 4.26. Therefore, the mask image plane and the captured substrate plane must positioned at the same location. Since the camera lens is focused at a distance of 550 m, it is assumed that the camera lens is focused to infinity. After the adjustment, the lithography and the camera system must have the same focal plane via the microscope lens. The lithography system's focus and the camera system's focus are compared using a USAF chart in the mask and the substrate plane. The USAF chart in the substrate plane has a reflective surface which affects the imaging of both USAF charts in the camera sensor's plane.

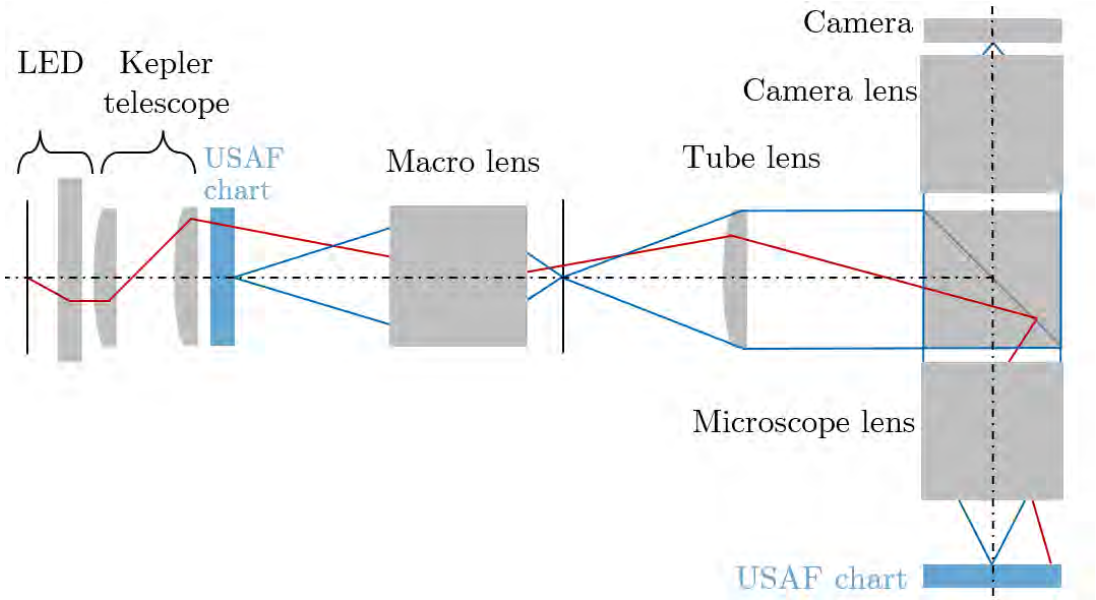

Figure 4.26: In the assembly of the lithography and camera systems, the lithography system's image plane and the camera system's focal plane are positioned at the same location. The focus of the lithography and the camera system are compared using a USAF chart in the mask and the substrate plane.

At first, the mask image plane M is below the the captured substrate plane S as shown in Figure 4.27 (a) and (b). The position of both focal planes are determined by moving the z axis of the stage with a step size of 1 µm. The tube lens' postion is changed to adjust the mask image plane's position interatively as demonstrated in Figure 4.27 (a). The final position is reached if no difference in the sharpness of both USAF chats can be detected with the camera as shown in Figure 4.27 (c).

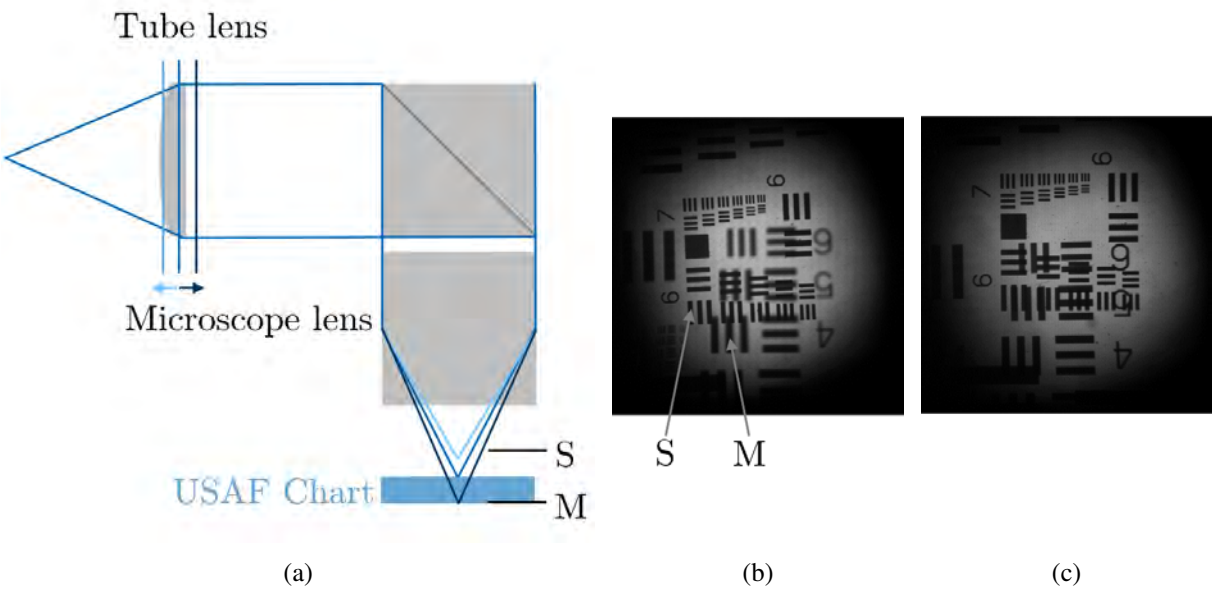

(a) (b) (c)

Figure 4.27: The assembly of the vertical camera system and the horizontal lithography system is conducted by moving the tube lens (a). At first, the mask is imaged below the substrate plane (b). The mask image plane and the captured substrate plane are matched iteratively until their images are sharply displayed (c). The vignetting of the images in (b) and (c) is due to the camera system.

The illumination in the substrate plane is checked since the movement of the tube lens affects the illumination path. According to the results in Appendix E, an equal useable area of 0.43 mm^2 is measured in this investigation. The illumination's homogeneity in the substrate plane corresponds to a FWHM of 0.19. Since the difference from 0.19 to the previously calculated 0.17 is lower than the measurement uncertainty, it is assumed that the impact of the system's change is negligible.

4.2.2.6 Evaluation of the Camera System

The magnification and the resolution of the camera system is evaluated to characterize the lithography system. A USAF chart is positioned in the substrate plane and illuminated by the lithography system's illumination as shown in Figure 4.28.

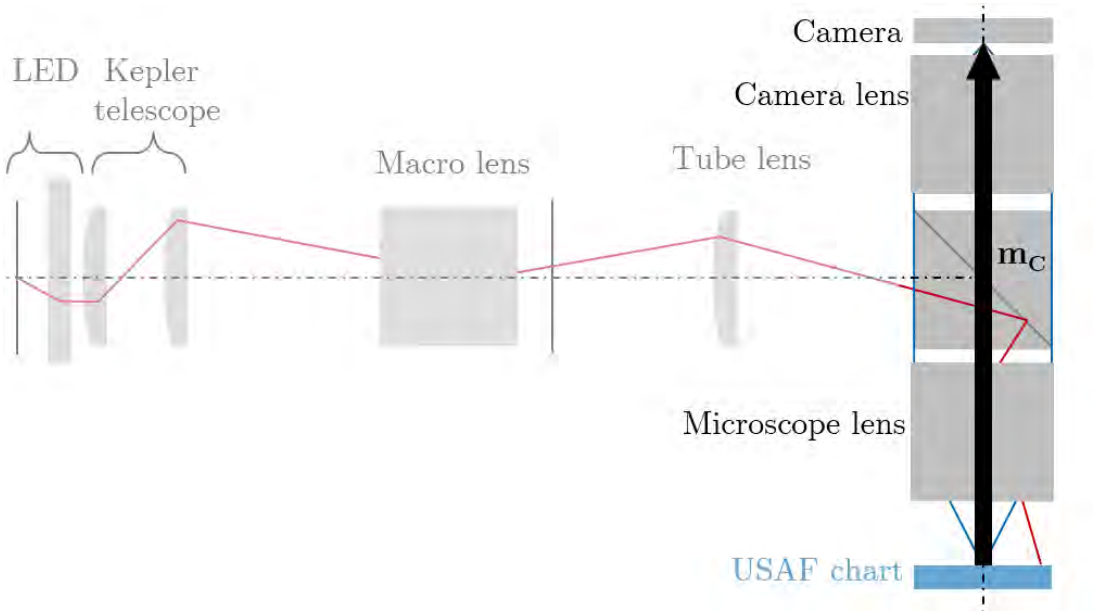

Figure 4.28: In the analysis of the camera system's magnification and resolution, a USAF chart in the substrate plane is illuminated by the lithography system's illumination. It is captured by the camera sensor. The camera system's magnification m_c is defined by the difference in size between the structure in the substrate plane and the imaged structure on the sensor.

The camera system's magnification m_C is calculated by moving the USAF chart 6 times in the substrate plane and measuring the period of group 6 element 2. The element 2 of group 6 has a resolution r_p of 71.8 lp/mm. One period of this element correlates to 50 measured[13] pixels n_{px} of the camera sensor. The camera sensor's pixels l_{px} are 1.67 µm/px. This results in a magnification factor of 6 as given in Equation 4.2.3.

$$m_C = l_{px} \cdot n_{px} \cdot r_p = 1.67 \cdot 10^{-3} \frac{mm}{px} \cdot 50\ px \cdot 71.8 \frac{1}{mm} = 6 \tag{4.2.3}$$

According to the imaged USAF chart of Figure 4.29, the resolution of the camera system is greater than 228 lp/mm. All elements of the USAF chart are resolved sufficiently. The camera system's resolution is more than 10 times the lithography system's resolution (23.1 lp/mm) as it will be evaluated in Chapter 4.2.2.7. Therefore, the camera system is a sufficient measurement instrument of the lithography system.

[13] Since the standard deviation is equal to ± 1% of the measurement value, it is neglected.

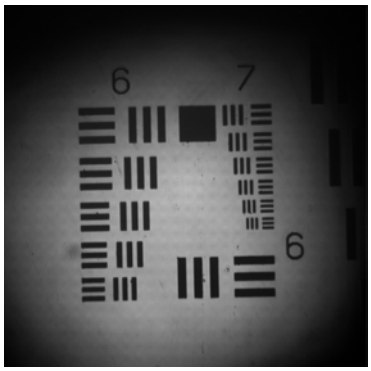

Figure 4.29: The magnification and resolution is evaluated by a captured USAF chart which is positioned in the substrate plane. It can be derived that the resolution is greater than 228 lp/mm based on the imaged USAF chart's elements.

4.2.2.7 Evaluation of the Lithography System

The evaluation of the lithography system units can be conducted based on the magnification factor of the camera system m_C and the captured images of the intermediate plane and the substrate plane. At first, the lithography system's magnification factor m_L and the resolution are analyzed. The used setup is illustrated in Figure 4.32. The USAF chart of the mask plane is imaged on the substrate plane. The camera sensor captures the USAF chart's image since the image is reflected by a mirror in the substrate plane.

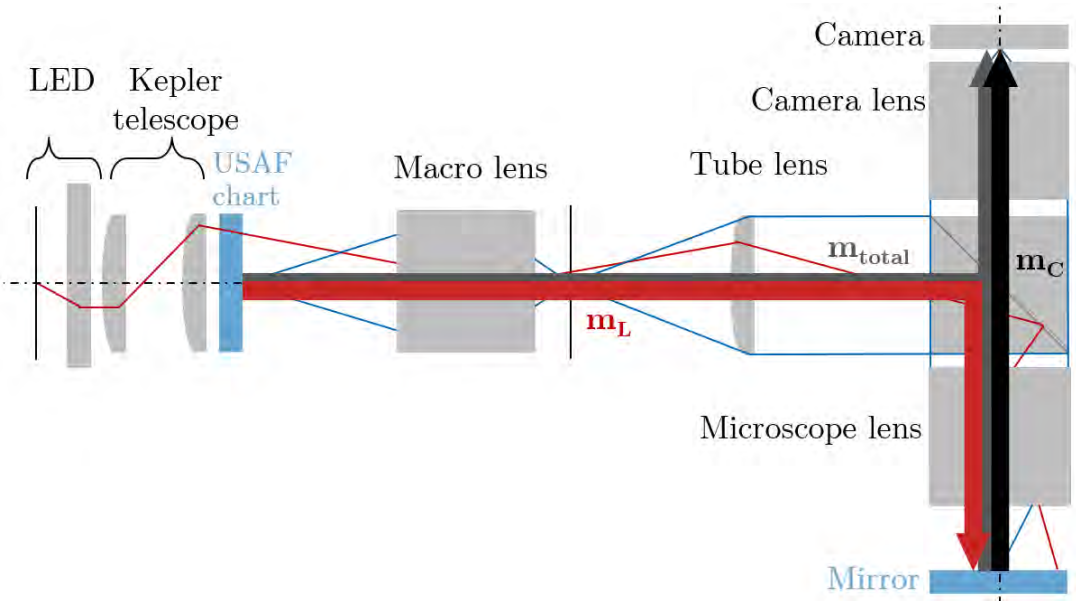

Figure 4.30: In the analysis of the lithography system's magnification and resolution, a USAF chart in the mask plane is illuminated and imaged in a mirror in the substrate plane. The camera sensor of the camera system captures the image of the substrate plane. The lithography system's magnification m_L is defined by the measurable total magnification m_{total} and the camera system's magnification m_C

The lithography system's magnification m_L is defined by the measurable total magnification m_{total} and the camera system's magnification m_C as given in Equation 4.2.4. In this analysis, element 3 of group 0 is measured on 6 camera sensor's images. The element 3 of group 0 has a resolution of r_p of 1.26 lp/mm on the original USAF chart. The respective measured element is imaged onto 84.76 sensor pixels n_{px} in average[14], while one pixel has a size l_{px} of 1.67 µm/px. Lithography system's magnification factor is 0.03 as demonstrated in Equation 4.2.4.

$$m_L = \frac{m_{total}}{m_C} = \frac{l_{px} \cdot n_{px} \cdot r_p}{m_C} \tag{4.2.4}$$

$$= \frac{1.67 \cdot 10^{-3} \, \frac{mm}{px} \cdot 84.76 \, px \cdot 1.26 \, \frac{1}{mm}}{6} = \frac{0.18}{6} = 0.03$$

The resulting FOV in the mask plane has a diameter of 24 mm based on the 0.72 mm spot diameter d_s in the substrate plane and the lithography system's magnification m_l as shown in Equation 4.2.5.

$$FOV = \frac{d_s}{m_L} = \frac{0.72 \, mm}{0.03} = 24 \, mm \tag{4.2.5}$$

The resolution of the lithography system is evaluated using USAF chart's images, such as the displayed image in Figure 4.31 (a). The respective MTF analysis of Figure 4.31 (b) is based on 6 samples. The measurement values are averaged and fitted to determine the resolution. The resolution of the total system is 22.1 lp/mm. Since the resolution of the camera system is more than 10 time greater, it is assumed that the lithography system is the limiting system unit.

[14] Since the standard deviation is lower than ± 1% of the measurement value, it is neglected.

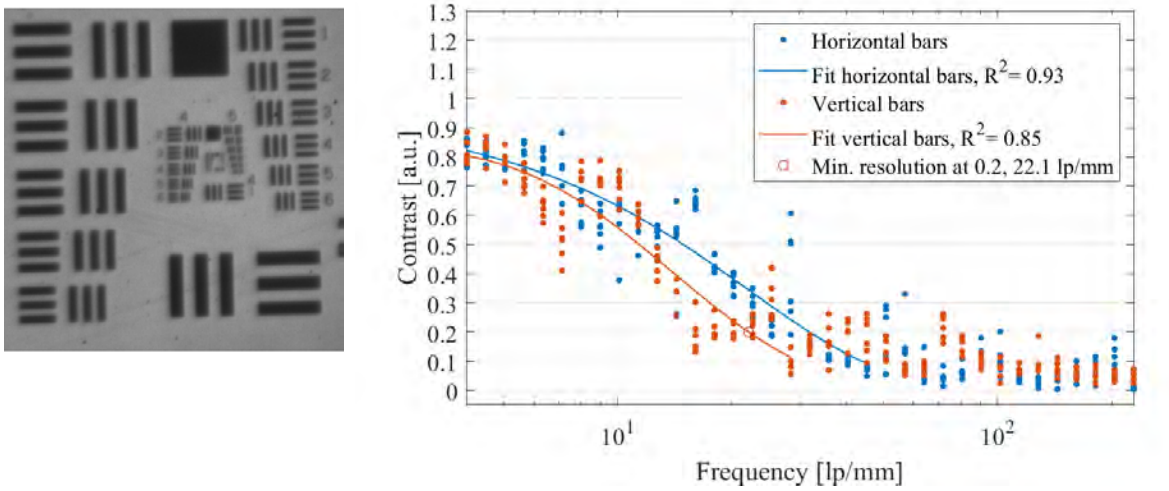

(a) (b)

Figure 4.31: The MTF analysis of the total system is based on imaged USAF charts such as the displayed one in (a). In general, 6 samples are used to calculate the MTF graphs of (b) and determine the lithography system's resolution.

The lithography system's magnification factor is based on the pre-magnification m_{L1} of the macro lens and the main magnification m_{L2} of the microscope lens. In the analysis of lithography system, the magnification and resolution of the macro lens are investigated as illustrated in Figure 4.32 (a). The intermediate image is captured by camera sensor and the respective resolution is evaluated by a MTF analysis. The microscope lens' magnification factor, which is shown in of Figure 4.32 (b), is calculated with respect to the lithography system's magnification m_L and macro lens' magnification m_{L1}.

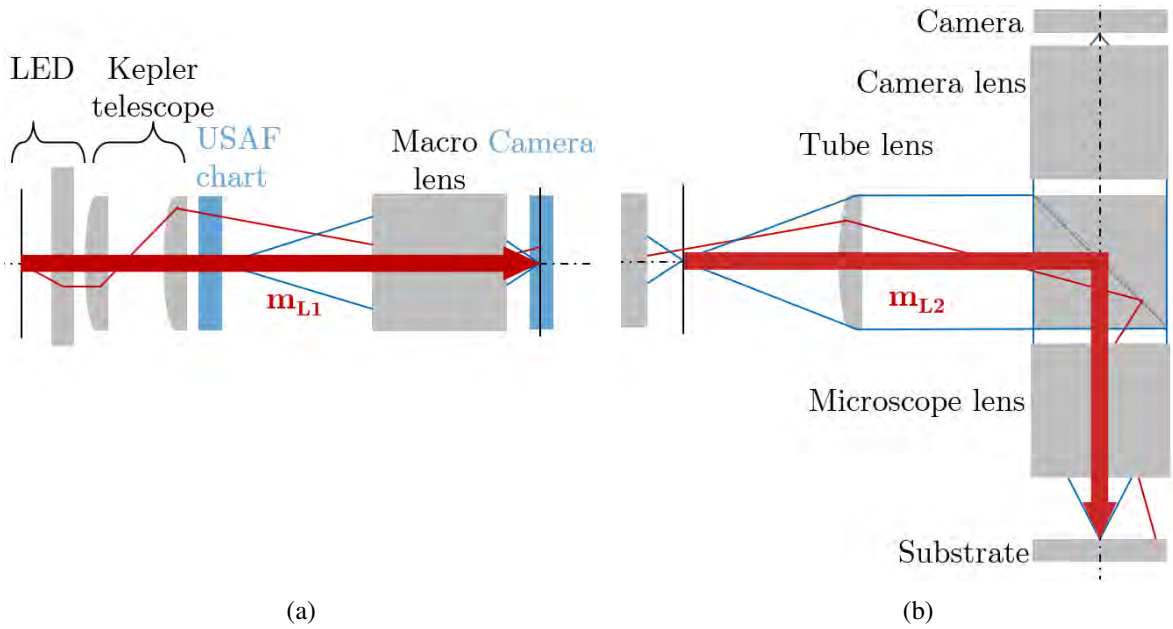

Figure 4.32: Visualization of the lithography system's resulting magnification which is based on the macro lens magnification m_{L1} (a) and the microscope lens' magnification m_{L2} (b). The macro lens' magnification and resolution is measured in the macro lens's image plane using a camera. The microscope lens' magnification is calculated with respect to the lithography system's magnification m_L and macro lens' magnification m_{L1}.

The macro lens' magnification factor is evaluated by correlating the USAF chart element 2 of group 2 and the respective measured pixels n_{px} of 6 camera sensors images which are comparable to the shown USAF chart of Figure 4.33 (a). The element 2 of group 2 has a resolution r_p of 4.49 lp/mm on the USAF chart in the mask plane, which refers to 32.72 pixels n_{px} on the camera's images in average[15]. In this measurement, the camera sensor has a pixel size l_{px} of 3.45 µm/px. The macro lens' magnification factor is 0.51 based on demonstrated calculation in Equation 4.2.6.

$$m_{L1} = l_{px} \cdot n_{px} \cdot r_p = 3.45 \cdot 10^{-3} \frac{mm}{px} \cdot 32.72\ px \cdot 4.49 \frac{1}{mm} = 0.51 \quad (4.2.6)$$

The resolution of the macro lens is evaluated by a MTF analysis. It is conducted using 6 captured USAF chart images such as the displayed one in Figure 4.33 (a). The average of the contrast values are fitted as shown in Figure 4.33 (b). Based on this analysis, the macro lens' resolution is 52.6 lp/mm.

[15] Since the standard deviation equals to ± 1% of the measurement value, it is neglected.

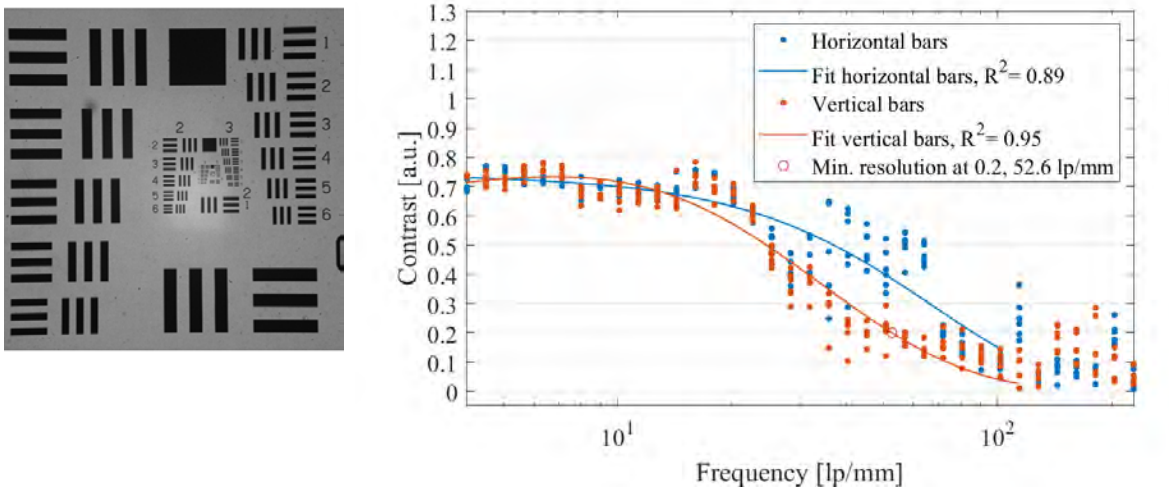

Figure 4.33: The MTF analysis of the macro lens is based on imaged USAF charts such as the displayed in (a). In general, 6 samples are used to calculate the MTF graphs of (b) and determine the macro lens' resolution.

As mention, the microscope lens' magnification is calculated based on the lithography system's magnification m_L and macro lens' magnification m_{L1}. Since the lithography system' magnification m_L is the product of the macro lens' magnification m_{L1} and the microscope lens' magnification m_{L2}, the microscope lens magnification m_{L2} is calculated by dividing the lithography system's magnification factor m_L through the macro lens' magnification factor m_{L1} as given in Equation 4.2.7. The calculated microscope lens' magnification factor of 0.06 is equal to the magnification of 16.6x.

$$m_{L2} = \frac{m_L}{m_{L1}} = \frac{0.03}{0.51} = 0.06 \tag{4.2.7}$$

4.2.2.8 Application of a Printed Photomask

The DMP printed masks are applied to the adjusted system as illustrated in Figure 4.34. The printed mask is illuminated by the KEPLER illumination and imaged in the intermediate plane as well as in the substrate plane. The camera captures the imaged mask structure via the mirror which is positioned in the substrate plane.

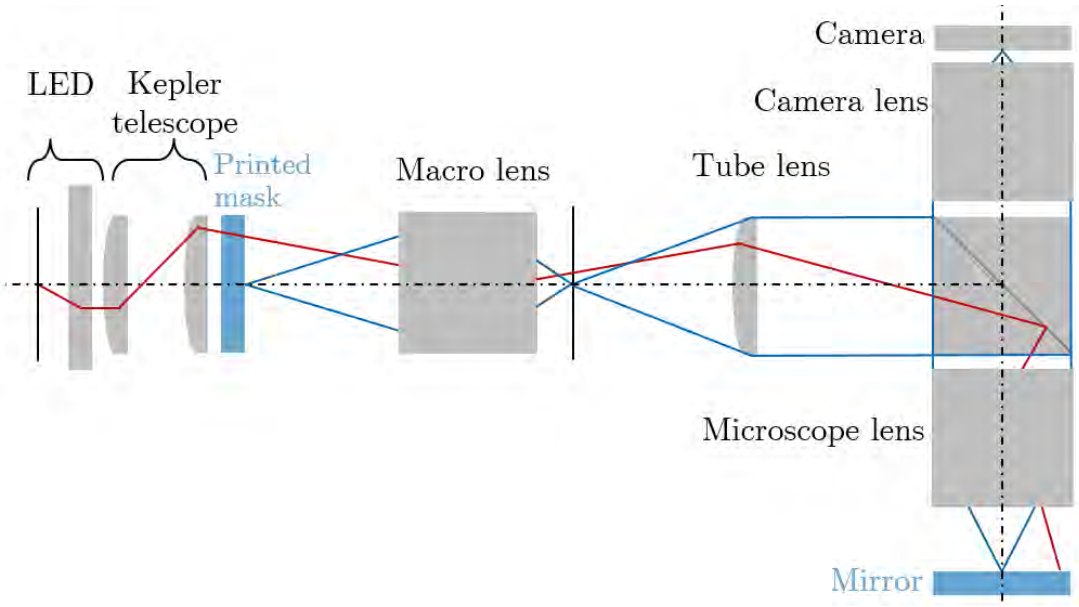

Figure 4.34: Setup of the lithography system by applying the printed photomask in the mask plane. The printed photomask is illuminated by the KEPLER illumination and imaged on the substrate plane. The image of the substrate plane is captured by the camera sensor via a mirror in the substrate plane.

The mask structure is imaged sharply without readjusting the substrate plane as shown in Figure 4.35. The smaller structures in the range of 45 µm to 75 µm in Figure 4.35 (a) are identifiable on the captured image. The structures[16] of 45 µm to 75 µm (a) and 90 µm to 135 µm (b) are imaged sharply on the substrate plane. Ink dots seem no longer visible at the structures' edges as displayed in the zoom images of Figure 4.35 (a) and (b). However, no reliable statement about the imaging in the photoresist can be made with respect to these images due to the camera system's impact on the imaging. The pixel size of 1.67 µm/px is not sufficient to measure the edge inaccuracy I_t of 12 µm which is magnified by 0.18 (m_{total}) on the camera sensor with respect to Equation 4.2.4. As demonstrated in Equation 4.2.8, the resulting imaged inaccuracy I_c of 2.16 µm can not be measured by a sensor pixel size l_{px} of 1.67 µm since it must be lower than the half size of the imaged inaccuracy. [17] [49].

$$I_c = m_{total} \cdot I_t = 0.18 \cdot 12\ \mu m = 2.16\ \mu m \tag{4.2.8}$$

[16] The given structures' size refer to the digital structure size.

[17] The sampling rate f_s must comply with the NYQUIST criteria. Thereby, the NYQUIST frequency f_{Nyq} is the highest frequency of the signal to be sampled: $f_s > 2 \cdot f_{Nyq}$ [49].

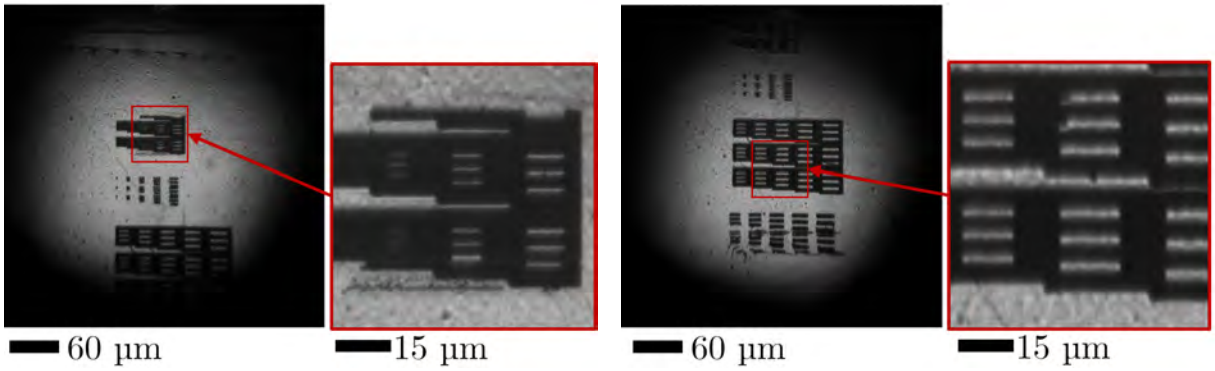

(a) (b)

Figure 4.35: The images of the substrate plane show the imaged printed mask. The structures of 45 µm to 75 µm (a) and 90 µm to 135 µm (b), which are identifiable on the mask, are imaged sharply on the substrate plane.

The printed photomask must be exposed onto a photoresist to evaluate the lithography system's effect on minimal reproducible structure size and the structures' edges quality. In this analysis, the structure size and the edges' standard deviation of the photoresist structures will be measured.

4.2.3 Illumination Power

It is necessary to know the power in the substrate plane for the correct exposure of a photoresist. The system's power is regulated by a LED controller via a Pulse Width Modulation (PWM) signal of an ADRUINO nano. In this experiment, the relative LED power is set 3 times in a range of 10 % to 100 % and the respective power is measured by a power meter near[18] the substrate plane as illustrated in Figure 4.36.

[18]The power meter can not placed directly in the substrate plane due to the senor fixation which conflict with the microscope lens. This is an advantage for the measuring since the power is distributed over a greater spot area and the sensor measures more precise.

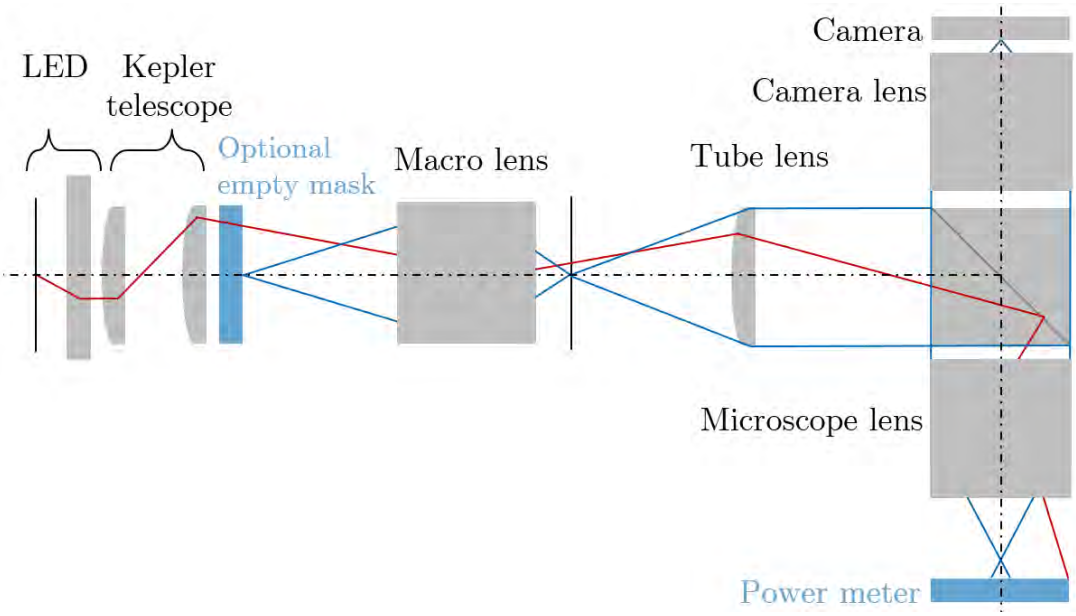

Figure 4.36: The lithography system's power during the exposure is set by the LED controller via a PWM signal. In the analysis of the expose power, the relative intensity from 10 % to 100 % is applied and the power in the substrate plane is measured by a power meter.

The measured power in the substrate plane under the application of an empty photomask and without a photomask is shown in Figure 4.37 (a). The power jumps in the circled relative LED intensity settings. There are three possible error sources. The power jump is caused by either the PWM signal, the LED controller, or the LED chip. The PWM signal is controlled with an oscilloscope and the LED controller is replaced. The results are added to Appendix G. Since the power characteristic of the new controller is the same, the LED chip is the identified error source. The application's power setting is limited to 60 % up to 100 % due the LED chips' defects at lower LED intensities. The resulting power as a function of the relative LED intensity is plotted in Figure 4.37 (b). The power behavior is linear as demonstrated by the fit function of mask applied setting. In comparison, the photomask absorbs 48.8 % of the applied power on average[19].

[19]At this point, the power absorption of 48.8 % can not be related to other condition or applications. The evaluated power absorption is useful in further investigations if the exposure power is improved or the mask type is changed for example.

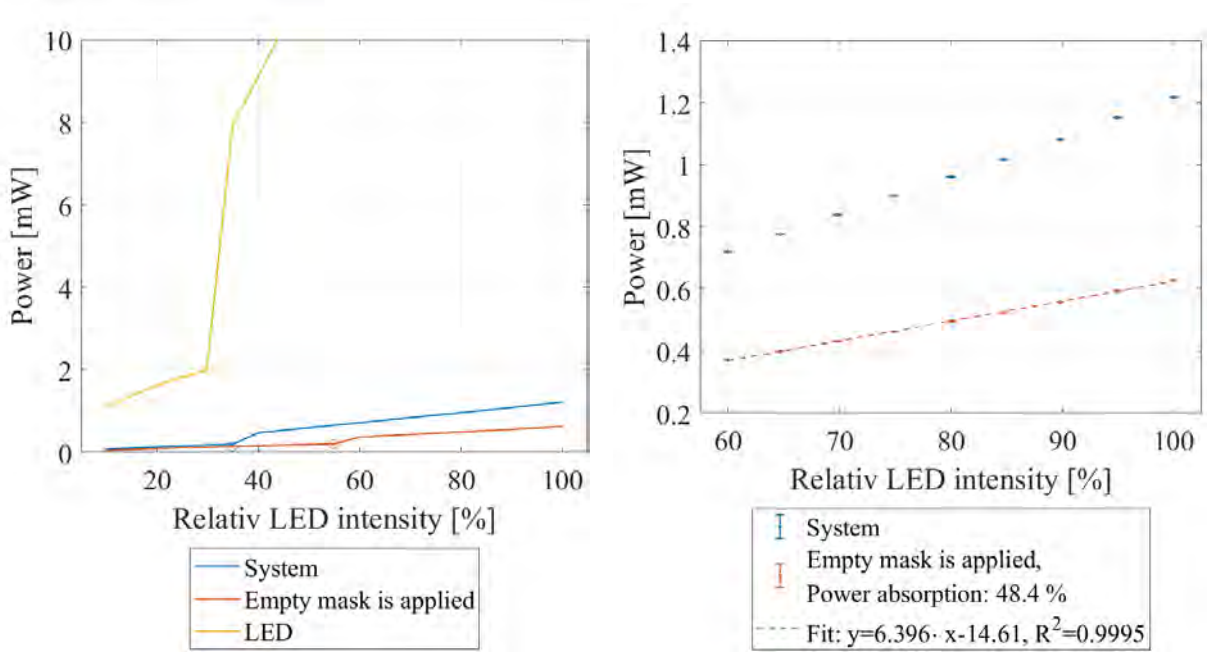

(a) (b)

Figure 4.37: The exposure power under different conditions is measured by a power meter. In (a), the measured LED power in relation to the relative LED intensity in a range from 10 % to 100 % is plotted. The system's power with an empty photomask (red) and without a photomask (blue) as well as the LED power (yellow) have a power jump due to a LED chip error. Therefore, the application's power settings are limited to 60 % up to 100 % as shown in (b).

A look-up table for possible exposure power and time settings is generated based on the analyzed power. The exposure time t_{LED} is defined by the required exposure dose D which is multiplied by the spot area A of $4.3 \cdot 10^{-1}$ mm^2 and divided by the set LED power P_{LED}. In the relative LED intensity P_{LEDrel} range of 60 % up to 100 %, the set LED power P_{LED} is calculated by the fit function of Figure 4.37 (b) as given in Equation[20] 4.2.9. The look-up table and a exposure time calculation are attached to Appendix H for example.

$$t_{LED} = \frac{D \cdot A}{P_{LED}} = \frac{D \, \frac{mJ}{cm^2} \cdot 4.3 \cdot 10^{-3} \, cm^2}{(6.396 \cdot P_{LEDrel} - 14.61) \, mW} \tag{4.2.9}$$

[20]The used units are not SI-compliant. Since the exposure dose D is commonly given in mJ/cm^2 in the photoresists' datasheets, the calculation is adapted.

5 Discussion

The analysis results of the DMP printed masks are dealt with by taking the printing resolution and the edge quality into account. Furthermore, the lithography system's magnification, its FOV and its illumination are discussed. The lithography system's resolution is not covered in this discussion since it will be evaluated based on the exposed photoresist structure as already mentioned in Chapter 4.2.2.8. The aim is to evaluate the measured system parameters to justify limits and to work out theoretically possible improvements.

5.1 Printing System

The smallest reproducible structure size of the DMP is 18 ± 2 µm at a digital bar size of 45 µm and has a total edge inaccuracy of I_t of 12 µm. Therefore, the size of the Canon printer's minimal printed structure is 22.7 % reduced using a Dimatix printer. According to [19], it is possible to print 1 µm negative structures using the DMP with a 15 µm drop spacing. If the negative mask structure should have a decreased bar size, the digital bar size, the edge inaccuracy, and the drop size must decrease without opposite edges drops flowing together. Therefore, it will be discussed which printing parameters limit the DMP's resolution and how the resolution of the inkjet-printed photomask can be improved.

Since larger bar sizes than 45 µm can be reproducibly printed in a step size of 15 µm, it is assumed that the DMP's position accuracy is sufficient to print smaller structures and the printing resolution of the analyzed mask printing is limited by the resulting ink dot diameter. With respect to Figure 2.28, the resulting ink dot diameter can be reduced by decreasing the drop volume V, increasing the ink dot's surface tension force F_S, decreasing the wettability F_W, or increasing the dry rate. If these parameters are modified, the complex relation of the mentioned parameters must be considered. For example, an increased ink density results in a decreased drop volume according to Equation 2.3.1. An increased ink density

can also decrease the surface tension which does not support a smaller ink dot diameter.

The mentioned parameters also affect the printed edge's inaccuracy. Smaller ink dots are improving as long as the edge inaccuracy is not worsened by reducing the dot diameter. As shown in Figure 5.1, the measured structure width S_m must be greater than the total edge inaccuracy of I_t to still be able to identify the blurred structure. If the minimal resolved structure width of the lithography system is greater than the total edge inaccuracy of I_t, the measured structure width S_m must be greater than the resolved structure width.

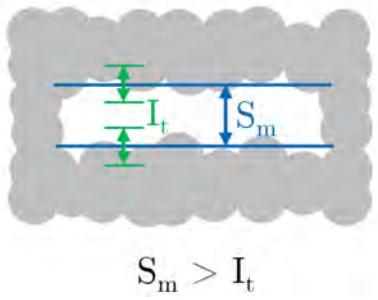

Figure 5.1: The dot size has a major impact on the total edge inaccuracy I_t. The measured structure width S_m must be greater than the total edge inaccuracy I_t to still be able to identify the blurred structure since structures, which are smaller than the total edge inaccuracy I_t, are blurred imaged.

5.2 Photolithography System

In the assembly of the lithography and camera system, the lithography system is adjusted by moving the tube lens. Since the microscope lens is optimized for capturing images from infinity, the system's adjustment would be more precise if the camera lens' setting is changed to focus on the lithography system's substrate plane. The focal offset Δf of the set image plane a and the focal plane f' is calculated to quantify the system error. As illustrated in Figure 5.2, the focal offset Δf is defined by the object distance a, the image distance a' and the focal length f' of the microscope lens.

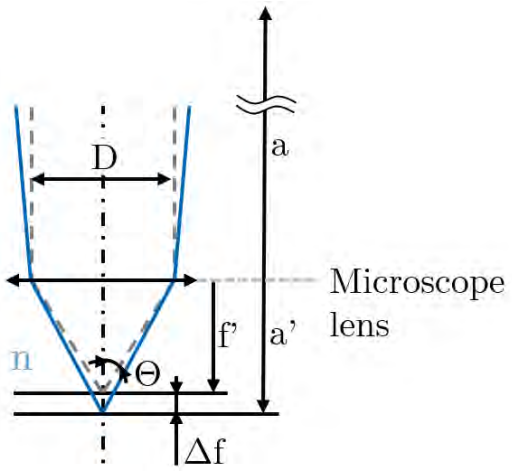

Figure 5.2: The focal offset Δf in the substrate plane is calculated based on the object distance a, the image distance a' and the focal length f' of the microscope lens.

The microscope lens' focal length f' is defined by the half aperture diameter D of 10 mm and microscope lens' NA of 0.5 as given in Equation 5.2.1. According to Equation 2.1.34, the NA is defined by the opening angle θ and the refractive index n.

$$f' = \frac{D}{2\,tan(sin^{-1}(NA_{\theta,n=1}))} \tag{5.2.1}$$

In the calculation of focal offset Δf of Equation 5.2.2, it is assumed that the object distance a is equal to the camera lens' image distance. The camera lens' image distance has been measured to be 550 m.

$$\Delta f = a' - f' = \frac{1}{\frac{1}{f'} - \frac{1}{a}} - f' \approx 150\,nm \tag{5.2.2}$$

Since the calculated offset of 150 nm is lower than the z-stage's step width[1], it is neglected.

The resolution of the inkjet-printed masks is significantly[2] lower than precise chromium masks. Therefore, inkjet photomasks tend to be printed as large as possible to minimize the impact of the ink dots on the exposured structures. Due to the larger printed mask structures, the magnification and the FOV are

[1]The minimum applied step width is 1.001 µm since focal differences are not identifiable using a smaller step size.

[2]In the comparison of a 18.1 µm DMP bar and a common USAF chart bar size (group 9, element 8) of 0.7 µm, the resolution of chromium masks are at least 25 times (significantly) higher.

relevant parameters and will be discussed.

In the comparison of the microscope lens' resulting and the expected [3] magnification, the resulting magnification factor m_{L2} is 0.06. This results in 86 % of the expected reduction. Based on Figure 5.3, the tube and the microscope lens are simplified to two thin lenses and the geometrical relation of Figure 2.3 are applied. According to Equation 2.1.13, the imaged magnification is determined by the tube length a and the image distance a' as well as the focal lengths f and f'. The reduction can be increased by increasing the tube lens' focal length f or decreasing the microscope lens' focal length. A decrease in the microscope lens' focal length can only be achieved by replacing the assembled lens.

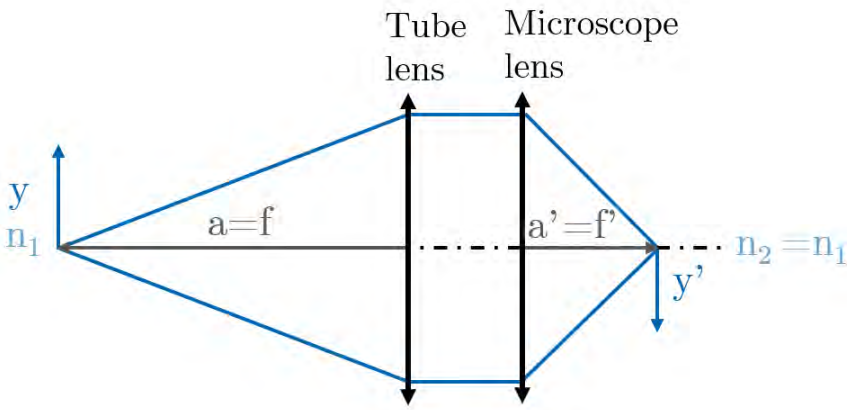

Figure 5.3: The geometrical relation of two thin lenses can be applied to the relation of the tube and the microscope lens. Based on this simplification, the magnification factor of the microscope lens m_{L2} is defined by the tube lens' focal length f and the microscope lens' assumed focal length f'.

Since the microscope lens' focal length is not given in the datasheet, it is assumed to be 10.5 mm based on Equation 5.2.3.

$$f' = a \cdot m_{L2} = 175\,mm \cdot 0.06 = 10.5\,mm \tag{5.2.3}$$

The expected magnification factor of 0.05 is achieved if the tube lens' focal length f is 210 mm by taking the assumed microscope lens' focal length f' of 10.5 mm into account. In general, a greater focal length of the tube lens results

[3] A 20x magnification is equal to a reducing magnification factor of 0.05.

in a greater reduction with respect to Equation 5.2.4.

$$f = \frac{f'}{m_{L2}} = 210\,mm \tag{5.2.4}$$

The lithography system's calculated FOV of 24 mm is defined by an aperture that is located in or nearby the object or intermediate plane since the edges are sharply imaged in the substrate plane. Otherwise, if the illumination path is cut off at other locations of the lithography system, vignetting in the substrate plane would occur[4]. The image at the intermediate plane is not restricted by any system element as demonstrated in Figure 4.11 (b). The mask holder is excluded as a restrictive unit since its diameter is 6 mm larger than the calculated FOV of 24 mm. The frame of the second KEPLER lens (f = 150 mm) has a measured diameter of 23.5 mm. The measured frame diameter is close to the calculated FOV of 24 mm. It is assumed that the illumination path's geometry, the measurement inaccuracy of the camera sensor in the substrate plane, and the rounding of the magnification factor cause the diameter deviation of 0.5 mm from the calculated FOV to the measured frame diameter. Based on this assumption, the frame of the second KEPLER lens (f = 150 mm) restricts the image diameter. The diameter of the second lens must be increased to enlarge the FOV by taking the increasing distortion at the outer area into account.

In comparison to the previous microscope-based lithography, the exposure time must be set 7 times longer to achieve the same exposure dose. This is not an issue since required exposure doses up to 280 mJ/cm^2 can be exposed using 100 % LED intensity and an exposure time shorter than 1 s[5]. If it is necessary, the illumination can be enlarged and improved by replacing the KEPLER telescope with a KÖHLER integrator. As shown in Figure 5.4, a KÖHLER integrator is based on two lens arrays *LA*1, *LA*2 and a condenser lens. For example, the fragmented illumination path demonstrates the principle of a KÖHLER integra-

[4]If the illumination is imaged to infinity and restricted by an aperture, the transmitted intensity is decreased and vignetting do not occur. This is comparable to the impact of an aperture in the FOURIER plane on images as explained according to Figure 2.16. Since the illumination of the Lithography system is not imaged to infinity as shown in Figure 4.11 (b), this case is not dealt with.

[5]The critical exposure time of 1 s is a rule of thumb to avoid a change in power due to thermal effects of the LED and the system. [12]

tor. The lens array $LA1$ is positioned in the focal length f_{LA2} and the focal length f_{LA} of $LA1$ is the half of f_{LA2} to optical integrate the beam. The condenser lens captures the fragmented beam and focuses them into the mask plane. In the comparison of a KEPLER and KÖHLER beam processing, an optical integrator is more efficient since a KEPLER telescope cut off a small beam diameter and enlarge it to illuminate the mask. Therefore, optical integrators are applied in commercial lithography systems. [63], [64]

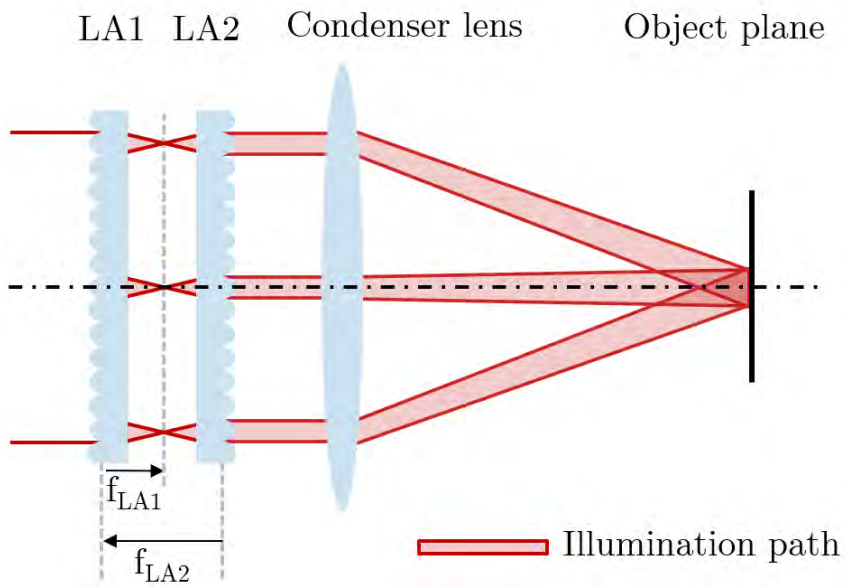

Figure 5.4: The KÖHLER integrator is based on two lens arrays $LA1$, $LA2$ and a condenser lens. The lens array $LA1$ is positioned in the focal length f_{LA2} and the focal length f_{LA} of $LA1$ is the half of f_{LA2} to optical integrate the incidence beam. The condenser lens captures the fragmented beam and focuses them into the mask plane. For example, the fragmented illumination path demonstrates the principle of a KÖHLER integrator.

6 Conclusion and Outlook

In the research within this thesis, the main goal is achieved. A new system was set up. It consists of a lithography system and a camera system, which is used to adjust the lithography system. The pre-magnification unit of the lithography system is construed to avoid the imaging of the photomask's identifiable ink dots. In this chapter, the main results, as well as the respective discussion, are summarized to answer the research questions. Subsequently, an outlook is given about the upcoming issues.

The smallest reproducible printed structure size is 22.7 % reduced using the DMP 2850 with a 15 µm drop spacing instead of the Canon iX6850. The minimal printed negative structure size is 18 $\pm$ 2 µm. The printed photomask's edges have a standard deviation of $\pm$ 2 µm on average. Based on the measured standard deviation, the total edges inaccuracy of 12 µm is determined, which is equal to a spatial frequency of 83.33 lp/mm. If the edge inaccuracy should no longer be resolved by the lithography system, the system's resolution must be less than 83.33 lp/mm. Therefore, the first question[1] is true.

In the analysis of the pre-magnification system, combinations of the macro lens' settings are analyzed with respect to the resolution, the FOV, and the distortion. The most optimal setting out of 252 compared settings is the combination of the aperture setting 2, a working distance f_w of 148 mm, and the zoom setting 9 ('f2, f_w=148mm, z9'). According to this, the second question[2] is answered.

According to the system's parametrization, the pre-magnification unit has a magnification factor of 0.51 and a resolution of 52.6 lp/mm. The microscope unit, based on the tube lens and the microscope lens, has a magnification factor of 0.06. The total magnification of the lithography system is equal to the product of the pre-magnification and the microscope unit's magnification factor. The lithography system's resulting magnification factor is 0.03. With respect to the

[1] First research question: Are there specific combinations of settings that let the mask's identifiable ink dots vanish?

[2] Second research question: Which combination of settings is the most optimal one, by taking the resolution, the FOV, and the distortion into account?

system's MTF analysis, the lithography system has a resolution of 22.1 lp/mm. Since the lithography system's resolution is significantly lower than the determined resolution limit of 83.33 lp/mm, the system avoids the imaging of the photomask's single ink dots in the substrate plane.

The lithography system's image in the substrate plane is captured by the camera system to adjust the lithography system by moving the stage with the substrate into the system's focal point. Since the camera system's resolution is not sufficiently precise, no reliant statement about the ink dots' vanishing can be made based on the camera images. The third research question, whether it is possible to develop steep edges in a photoresist and simultaneously keep the contrast of the original mask image, will be answered in future experiments. In these future experiments, a non-linear photoresist will be exposed through a binary printed mask and the effect of the blurred image will be evaluated based on the developed structure size and the edge quality. The contrast behavior of the photoresist structures can be measured by the aspect ratio of the developed structures.

The developed photoresist structure will be used as a NIL master. Its structure can be replicated several times by a NIL stamp. The NIL stamp manufacturing in detail is known from [4].

In the next step, grayscale lithography can be applied by using a grayscale photomask and a linear photoresist as shown in Figure 6.1. The ink dot density (a) determine the exposure intensity distribution of the macro lens' blurred image (b) and the reduced image in the substrate plane (c). The photoresist's linear behavior supports that the development depth correlates with the applied exposure intensity as demonstrated in (d).

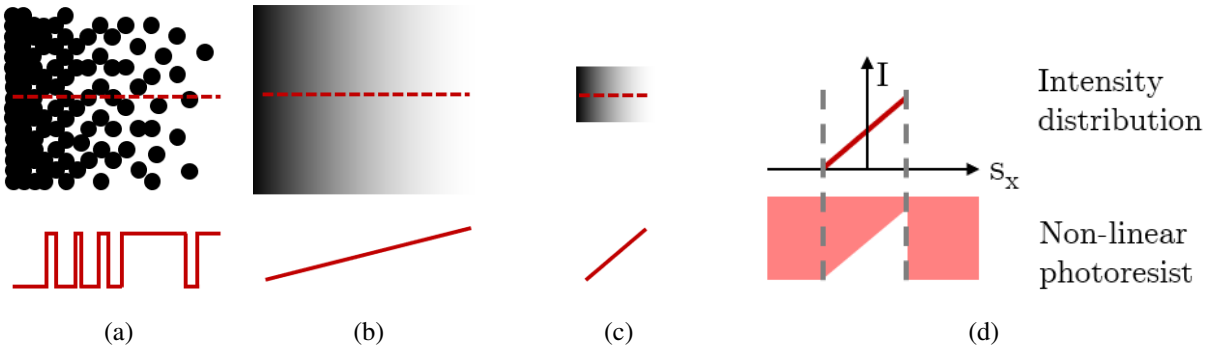

Figure 6.1: Theory of the lithography system's effects on the mask structure and the developed photoresist structure. The mask structure (a) is blurred imaged in an intermediate image (b) to make the ink dots unidentifiable. Subsequently, the structure is significantly reduced onto the photoresist's surface (c). The development depth of a linear photoresist correlates with the applied exposure intensity (d).

Bibliography

[1] Alvarenga, L.: The race to super-resolution microscopy: Is deconvolution enough? (2019). URL https://bit.ly/3HBauOY

[2] Atul pasare: How inkjet printer work - shared product video from hp (2017). URL https://bit.ly/3rGva3E

[3] Ban, C.H., Park, E.S., Ha, U.J.: Pattern dependent distortion and temperature variation in euv mask (2020)

[4] Burkert, S.: Development of a nanoimprint stamp using a lithography master: Implementation and evaluation of an imprint stamp manufacturing process

[5] Burkert, S.: Research results: Master manufacturing

[6] Burkert, S.: Development of a lithography master for nanoimprint processes: Evaluation of an inkjet lithography mask for conventional lithography (2021)

[7] Calafiore, G., Koshelev, A., Dhuey, S., Sassolini, S., Messerschmidt, M., Schleunitz, A., Goltsov, A., Piña-Hernandez, C., Pirri, F.C., Yankov, V., Cabrini, S., Peroz, C.: Step-and-repeat nanoimprint on pre-spin coated film for the fabrication of integrated optical devices. Journal of Micro/-Nanolithography, MEMS, and MOEMS **14**(3), 033,506 (2015). DOI 10.1117/1.JMM.14.3.033506

[8] Carl Zeiss SMT GmbH: Lithographie bei 13,5 nanometern (euv) (17.01.2021). URL https://bit.ly/309nWGJ

[9] Computar: Mlh-10x datasheet (2004). URL https://bit.ly/3saVJhI

[10] Cui, Z., Du, J., Guo, Y.: Overview of grey-scale photolithography for micro-optical elements fabrication. In: E.G. Johnson (ed.) Micromachin-

ing Technology for Micro-Optics and Nano-Optics, SPIE Proceedings, p. 111. SPIE (2003). DOI 10.1117/12.477831

[11] Dai, G., Hahm, K., Sebastian, L., Heidelmann, M.: Comparison of euv photomask metrology between cd-afm and tem. Nanomanufacturing and Metrology (2022). DOI 10.1007/s41871-022-00124-y

[12] Eder, C., Heinrich, A., Burkert, S.: Evg manual (notes on evg training): Lithography, smartnil und softnil an der evg anlage (2021)

[13] Fermum, L.: Grenzauflösung und mtf (2022). URL `https://bit.ly/36ZV8ax`

[14] Goodman, J.W.: Introduction to fourier optics (1996)

[15] Greve, M.M., Holst, B.: Optimization of an electron beam lithography instrument for fast, large area writing at 10 kv acceleration voltage. Journal of Vacuum Science & Technology B, Nanotechnology and Microelectronics: Materials, Processing, Measurement, and Phenomena **31**(4), 043,202 (2013). DOI 10.1116/1.4813325

[16] Gross, H.: Handbook of Optical Systems - Fundamentals of Technical Optics. Betz-Druck GmbH, Darmstadt (2011)

[17] Gross, H.: Handbook of Optical Systems - Aberration Theory and Correction of Optical Systems. WILEY-VCH Verlag GmbH & Co. KGaA (2012)

[18] Gross, H.: Imaging and aberration theory (2018). URL `https://bit.ly/3LuXf5Z`

[19] Grubb, P.M., Subbaraman, H., Park, S., Akinwande, D., Chen, R.T.: Inkjet printing of high performance transistors with micron order chemically set gaps. Scientific reports **7**(1), 1202 (2017). DOI 10.1038/s41598-017-01391-2

[20] Hecht, E., Lippert, K.: Optics, 7th ed. edn. De Gruyter Studium Ser. De Gruyter, Inc, Berlin/Boston (2018)

[21] Helmuth, T.: Fundamental optics - lecture. Ph.D. thesis, Hochschule Aalen, Aalen (Wintersemester 20/21)

[22] Jang, C., Mercier, O., Bang, K., Li, G., Zhao, Y., Lanman, D.: Design and fabrication of freeform holographic optical elements. ACM Transactions on Graphics pp. 1–15 (2020). DOI 10.1145/3414685.3417762

[23] Kanellos, M.: Intel's accidental revolution (2002). URL `https://cnet.co/3Ba357Q`

[24] Kim, S., Kim, D.H., Kim, W., Cho, Y.T., Fang, N.X.: Additive manufacturing of functional microarchitected reactors for energy, environmental, and biological applications. International Journal of Precision Engineering and Manufacturing-Green Technology **8**(1), 303–326 (2021). DOI 10.1007/s40684-020-00277-5

[25] Köhler, H.: On abbe's theory of image formation in the microscope. Optica Acta: International Journal of Optics (1981). DOI 10.1080/713820514

[26] Laube, P.: Photolithography - photomasks (2012). URL `https://bit.ly/3Lp6HHR`

[27] Le, H.P.: Progress and trends in ink-jet printing technology. Journal of Imaging Science and Technology (1998)

[28] Li, D.: Encyclopedia of Microfluidics and Nanofluidics. Springer New York, New York, NY (2015). DOI 10.1007/978-1-4614-5491-5

[29] Liu, W., Wang, J., Xu, X., Zhao, C., Xu, X., Weiss, P.S.: Single-step dual-layer photolithography for tunable and scalable nanopatterning. ACS nano (2021). DOI 10.1021/acsnano.1c03703

[30] MacEvoy, B.: Astronomical optics (2015). URL `https://bit.ly/3HzIco8`

[31] MATRIX VISION GmbH: Usb3 vision industriekamera mit e2v / aptina sensoren - mvbluefox3 - industrielle bildverarbeitung (16.02.2021). URL `https://bit.ly/3bJjIwa`

[32] Mattelin, M.A., Radosavljevic, A., Missinne, J., Cuypers, D., Kommeren, S., Vandael, J., ter Meulen, J.M., Verduyckt, L., van Steenberge, G.: Fabrication and replication of high efficiency blazed gratings with grayscale electron beam lithography and uv nanoimprint lithography. In: G. von Freymann, E. Blasco, D. Chanda (eds.) Advanced Fabrication Technologies for Micro/Nano Optics and Photonics XIII, p. 3. SPIE (01.02.2020 - 06.02.2020). DOI 10.1117/12.2542171. URL https://bit.ly/3kFxDGt

[33] Namedanian, M., Nyström, D., Zitinski Elias, P.: Physical and optical dot gain: Characterization and relation to dot shape and paper properties (2014)

[34] NAUTA SIGN B.V.: Hp thermal inkjet vs piezo printheads the technology behind hp latex printing (2016). URL https://bit.ly/33idvWC

[35] Optem Avimo Precision Instruments: Macro video zoom lens (2000). URL https://bit.ly/3p1UGOZ

[36] Parraman, C.: Colour printing techniques. In: Colour Design, pp. 497–531. Elsevier (2012). DOI 10.1533/9780857095534.3.497

[37] Pfanner, G.: Die wellengleichung. URL https://bit.ly/3uyM461

[38] Physik Instrumente: M-501 datasheet (2020)

[39] Physik Instrumente: M-531 datasheet (2020)

[40] Pina-Hernandez, C., Lacatena, V., Calafiore, G., Dhuey, S., Kravtsov, K., Goltsov, A., Olynick, D., Yankov, V., Cabrini, S., Peroz, C.: A route for fabricating printable photonic devices with sub-10 nm resolution. Nanotechnology **24**(6), 065,301 (2013). DOI 10.1088/0957-4484/24/6/065301

[41] Prudyus, I., Tkachenko V., Kondratov P.: Factors affecting the quality of formation and resolution of images in remote sensing systems (2015)

[42] Ramirez, J.C.C., Tumolva, T.P.: Analysis and optimization of water-based printing ink formulations for polyethylene films. Applied Adhesion Science (2018). DOI 10.1186/s40563-017-0102-z

[43] Rauschnabel, P.A.: Augmented reality is eating the real-world! the substitution of physical products by holograms. International Journal of Information Management **57**, 102,279 (2021). DOI 10.1016/j.ijinfomgt.2020.102279

[44] Rothschild, M.: Projection optical lithography. Materials Today (2), 18–24 (2005). DOI 10.1016/S1369-7021(05)00698-X

[45] Rybach, J.: Physik für bachelors (2019)

[46] Saha, T.K., Knaus, T.N., Khosla, A., Sekhar, P.K.: Investigation of printing properties on paper substrate. Journal of The Electrochemical Society **165**(8), B3163–B3167 (2018). DOI 10.1149/2.0211808jes

[47] Sankey, N.D., Prelewitz, D.F., Brown, T.G.: All–optical switching in a nonlinear periodic–waveguide structure. Applied Physics Letters pp. 1427–1429 (1992). DOI 10.1063/1.107311

[48] Sauter, M.: Euv-halbleiterfertigung: Asml bereitet sich auf high-na-belichtung vor. Golem.de (26.03.2020). URL `https://bit.ly/3uQQpiH`

[49] Schramm, A.: Signale und Systeme I. DHBW Mosbach (2016)

[50] Sieber, I., Thelen, R., Gengenbach, U.: Enhancement of high-resolution 3d inkjet-printing of optical freeform surfaces using digital twins. Micromachines **12**(1) (2020). DOI 10.3390/mi12010035

[51] Socol, Y., Guzman, I.S.: Fast ring-shape self-assembling in water-based ink-jetted droplets. The journal of physical chemistry. B (2006). DOI 10.1021/jp0637577

[52] Song, Y., Gui, C., Huo, Z., Lee, S.W.R., Liu, S.: Mechanical system and dynamic control in photolithography for nanoscale fabrication: A critical review. International Journal of Mechanical System Dynamics (2021). DOI 10.1002/msd2.12010

[53] Stankovska, M., Gigac, J.: The effect of surface sizing on paper - wettablity and on properties of inkjet prints. WOOD RESEARCH (2014)

[54] Tani, T.: Photographic Sensitivity : Theory and Mechanisms. Oxford University Press (1995)

[55] Thorlabs: La1027-a datasheet (2009)

[56] Thorlabs: La1229-a datasheet (2009)

[57] Thorlabs: La1433-a datasheet (2009)

[58] Thorlabs: Wavefront sensor manual (2020)

[59] Thorlabs: Ccm1-bs013 (2021)

[60] Thorlabs: M405l4-c4 datasheet (2021)

[61] Totzeck, M.: Photonic technologies for the fabrication of integrated circuits - ringvorlesung optik (2021)

[62] van Stetten, E., Rook, K., Mesilhy, H.: Multilayer optimization for high-na euv mask3d suppression. Proc. SPIE (2020)

[63] Vetter, A.: Resolution enhancement in mask aligner photolithography

[64] Voelkel, R., Weible, K.J.: Laser beam homogenizing: Limitations and constraints (2008)

[65] W3C Recommendation: Portable network graphics (png) specification (second edition) (2003). URL `https://bit.ly/3rGxDIT`

[66] W3C Recommendation: Coordinate systems, transformations and units — svg 2 (2018). URL `https://bit.ly/3rdLTsd`

[67] Waits, C.M., Modaf, A., Ghodssi, R.: Investigation of gray-scale technology for large area 3d silicon mems structures. Journal of Micromechanics and Microengineering (2002)

[68] Wang, M.: Three-Dimensional Integrated Photonics in Transparent Substrates Enabled by Femtosecond Laser Fabrication (2020)

[69] Weichelt, T., Vogler, U., Stuerzebecher, L., Voelkel, R., Zeitner, U.D.: Resolution enhancement for advanced mask aligner lithography using phase-shifting photomasks. Optics express (2014). DOI 10.1364/OE.22.016310

[70] Wikimedia Foundation Inc.: 1951 usaf resolution test chart (2020). URL https://bit.ly/3bdmM3q

[71] Wikimedia Foundation Inc.: Kugelwelle (2021). URL https://bit.ly/3osqYCl

[72] Wikimedia Foundation Inc.: Photomask (2021). URL https://bit.ly/3rFudIT

[73] Xiong, J., Yin, K., Li, K., Wu, S.T.: Holographic optical elements for augmented reality: Principles, present status, and future perspectives. Advanced Photonics Research **2**(1), 2000,049 (2021). DOI 10.1002/adpr.202000049

[74] Zheng, Y., Zhang, Y., Hu, J., Lin, Q.: Calculation of droplet size and formation time in electrohydrodynamic based pulsatile drug delivery system. URL http://arxiv.org/pdf/1207.3785v1

[75] Zhou, W.: Nanoimprint Lithography: An Enabling Process for Nanofabrication. Springer Berlin Heidelberg, Berlin, Heidelberg (2013). DOI 10.1007/978-3-642-34428-2

Appendices

A Visual Comparison of BK- and PGBK-Printed Structures

In the following visual comparison, the BK and PGBK-printed structures in the range of 60 µm up to 195 µm are imaged. It can be derived that the bar size discretization is similar using BK ink or PGBK ink due to the comparable bar widths. The black inks are displayed in light gray.

Printed background, BK, 60 µm

Printed background, PGBK, 60 µm

Printed bars, BK, 60 µm

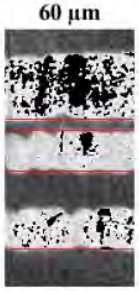

Printed bars, PGBK, 60 µm

Printed background, BK, 62.5 µm

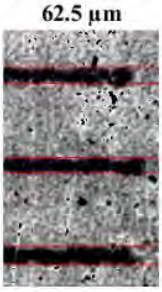

Printed background, PGBK 62.5 µm

Printed bars, BK, 62.5 µm

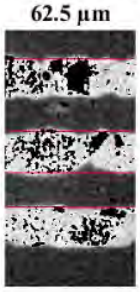

Printed bars, PGBK, 62.5 µm

Printed background, BK, 65 µm

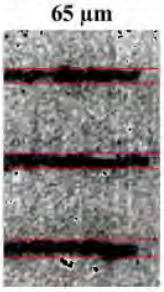

Printed background, PGBK, 65 µm

Printed bars, BK, 65 µm

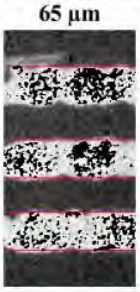

Printed bars, PGBK, 65 µm

Printed background, BK, 67.5 µm

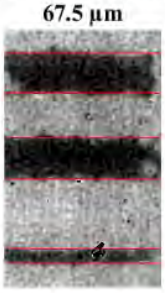

Printed background, PGBK, 67.5 µm

Printed bars, BK, 67.5 µm

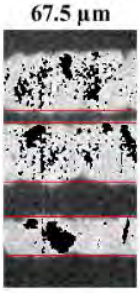

Printed bars, PGBK, 67.5 µm

Printed background, BK, 70 µm

Printed background, PGBK, 70 µm

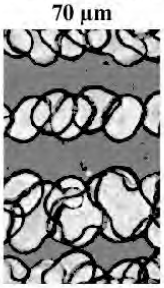

Printed bars, BK, 70 µm

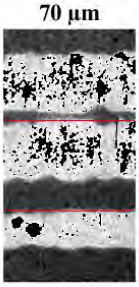

Printed bars, PGBK, 70 µm

Printed background, BK, 72.5 µm

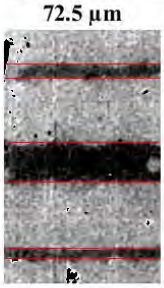

Printed background, PGBK 72.5 µm

Printed bars, BK, 72.5 µm

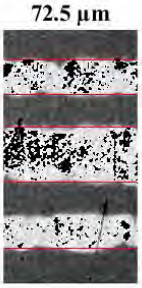

Printed bars, PGBK, 72.5 µm

Printed background, BK, 75 µm

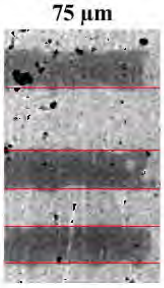

Printed background, PGBK, 75 µm

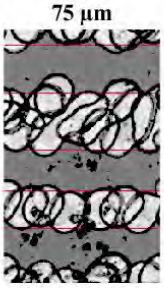

Printed bars, BK, 75 µm

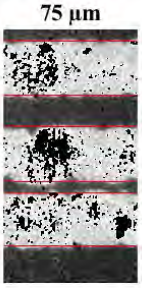

Printed bars, PGBK, 75 µm

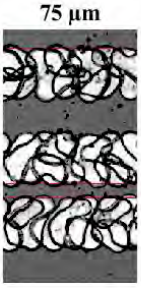

Printed background, BK, 77.5 µm

Printed background, PGBK, 77.5 µm

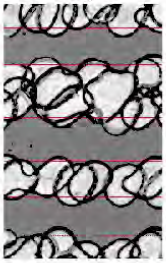

Printed bars, BK, 77.5 µm

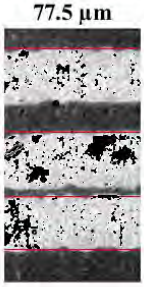

Printed bars, PGBK, 77.5 µm

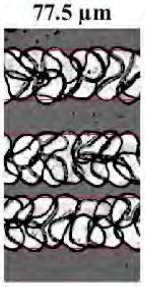

Printed background, BK, 80 µm

Printed background, PGBK, 80 µm

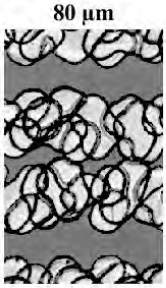

Printed bars, BK, 80 µm

Printed bars, PGBK, 80 µm

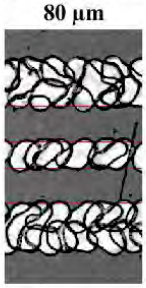

Printed background, BK, 82.5 µm

Printed background, PGBK 82.5 µm

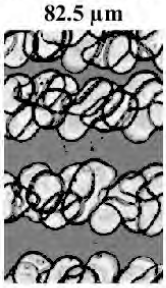

Printed bars, BK, 82.5 µm

Printed bars, PGBK, 82.5 µm

Printed background, BK, 85 µm

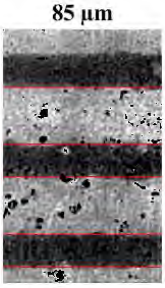

Printed background, PGBK, 85 µm

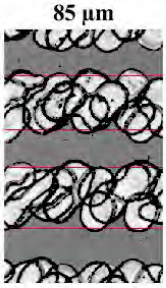

Printed bars, BK, 85 µm

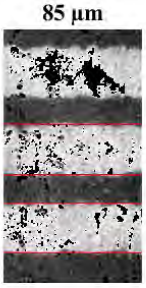

Printed bars, PGBK, 85 µm

Printed background, BK, 87.5 µm

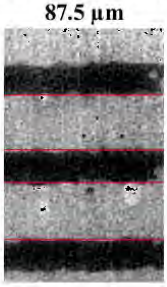

Printed background, PGBK, 87.5 µm

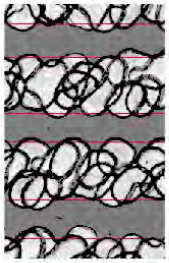

Printed bars, BK, 87.5 µm

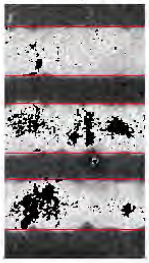

Printed bars, PGBK, 87.5 µm

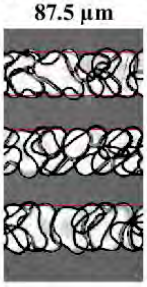

Printed background, BK, 90 µm

Printed background, PGBK, 90 µm

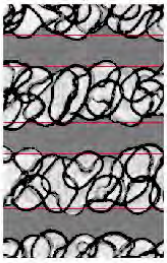

Printed bars, BK, 90 µm

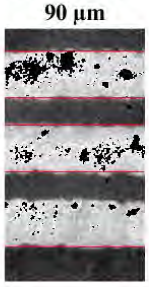

Printed bars, PGBK, 90 µm

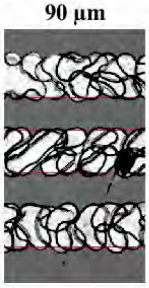

Printed background, BK, 92.5 µm

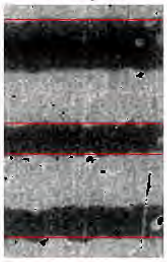

Printed background, PGBK 92.5 µm

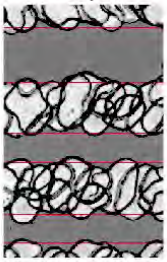

Printed bars, BK, 92.5 µm

Printed bars, PGBK, 92.5 µm

Printed background, BK, 95 µm

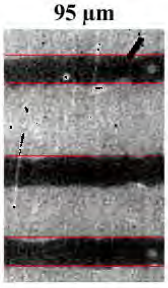

Printed background, PGBK, 95 µm

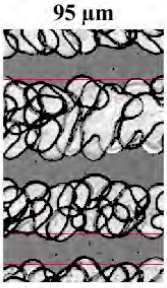

Printed bars, BK, 95 µm

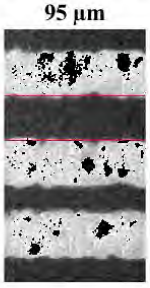

Printed bars, PGBK, 95 µm

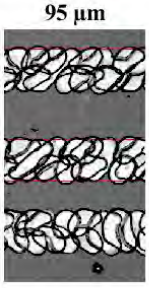

Printed background, BK, 97.5 µm

Printed background, PGBK, 97.5 µm

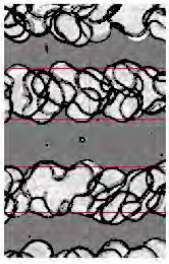

Printed bars, BK, 97.5 µm

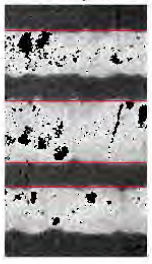

Printed bars, PGBK, 97.5 µm

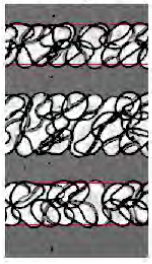

Printed background, BK, 100 µm

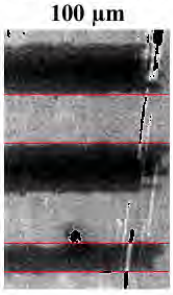

Printed background, PGBK, 100 µm

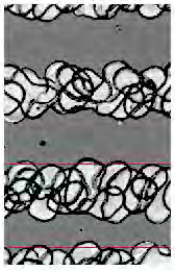

Printed bars, BK, 100 µm

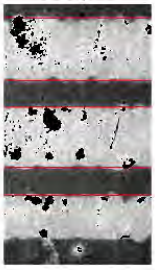

Printed bars, PGBK, 100 µm

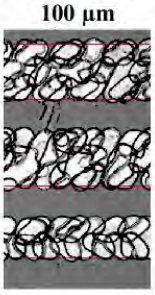

Printed background, BK, 102.5 µm

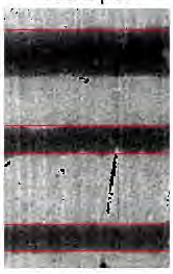

Printed background, PGBK 102.5 µm

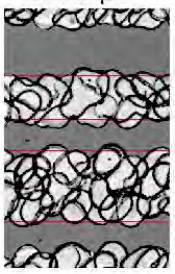

Printed bars, BK, 102.5 µm

Printed bars, PGBK, 102.5 µm

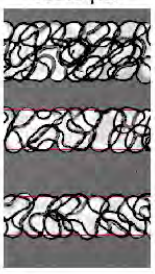

Printed background, BK, 105 µm

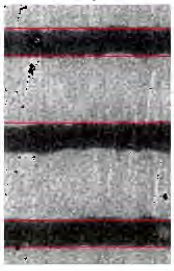

Printed background, PGBK, 105 µm

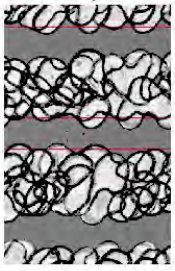

Printed bars, BK, 105 µm

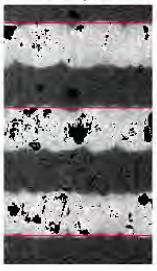

Printed bars, PGBK, 105 µm

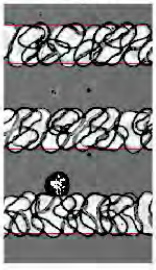

Printed background, BK, 107.5 µm

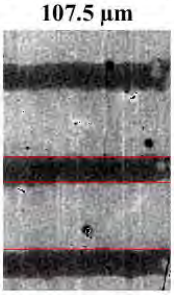

Printed background, PGBK, 107.5 µm

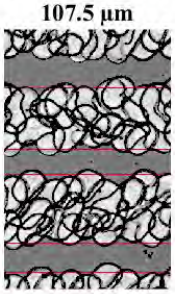

Printed bars, BK, 107.5 µm

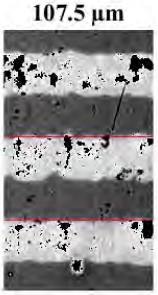

Printed bars, PGBK, 107.5 µm

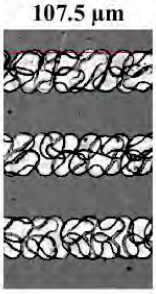

Printed background, BK, 110 µm

Printed background, PGBK, 110 µm

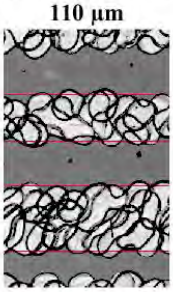

Printed bars, BK, 110 µm

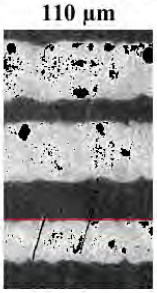

Printed bars, PGBK, 110 µm

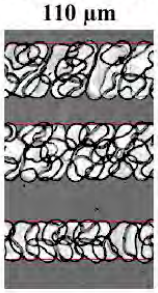

Printed background, BK, 112.5 µm

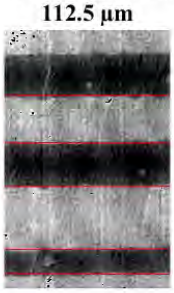

Printed background, PGBK 112.5 µm

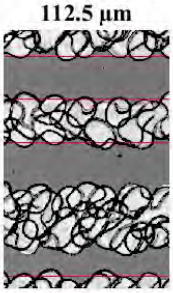

Printed bars, BK, 112.5 µm

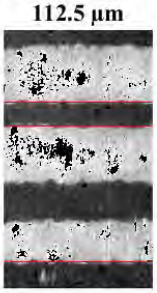

Printed bars, PGBK, 112.5 µm

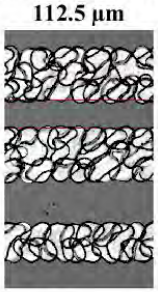

Printed background, BK, 115 µm

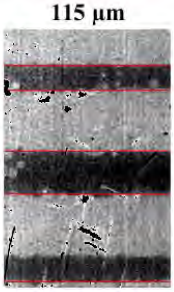

Printed background, PGBK, 115 µm

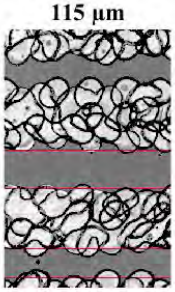

Printed bars, BK, 115 µm

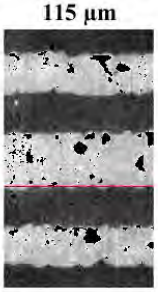

Printed bars, PGBK, 115 µm

Printed background, BK, 117.5 µm

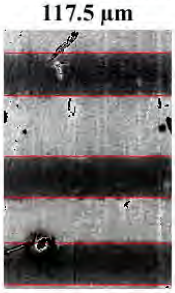

Printed background, PGBK, 117.5 µm

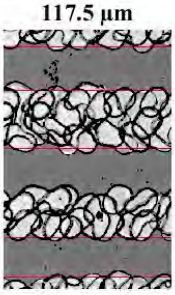

Printed bars, BK, 117.5 µm

Printed bars, PGBK, 117.5 µm

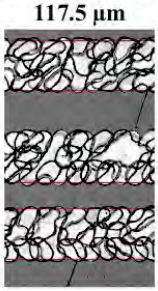

Printed background, BK, 120 µm

Printed background, PGBK, 120 µm

Printed bars, BK, 120 µm

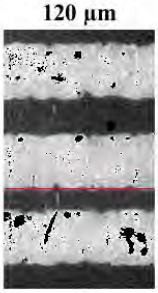

Printed bars, PGBK, 120 µm

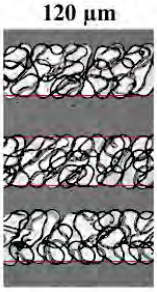

Printed background, BK, 122.5 µm

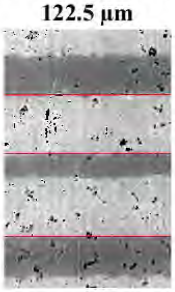

Printed background, PGBK 122.5 µm

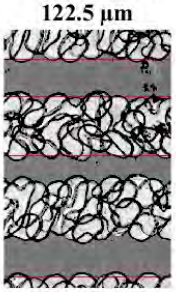

Printed bars, BK, 122.5 µm

Printed bars, PGBK, 122.5 µm

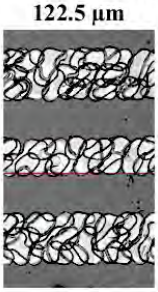

Printed background, BK, 125 µm

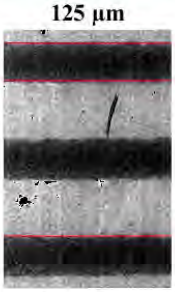

Printed background, PGBK, 125 µm

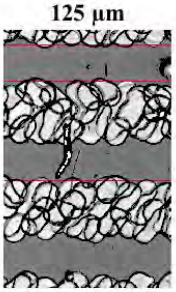

Printed bars, BK, 125 µm

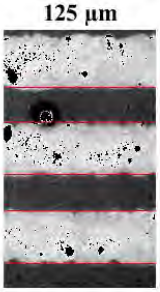

Printed bars, PGBK, 125 µm

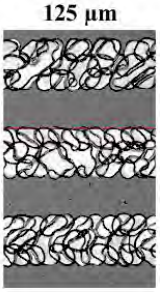

Printed background, BK, 127.5 µm

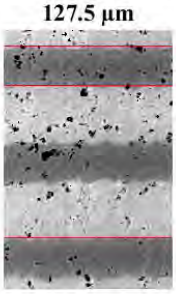

Printed background, PGBK, 127.5 µm

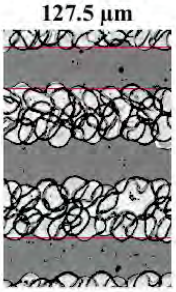

Printed bars, BK, 127.5 µm

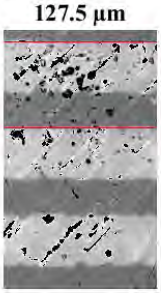

Printed bars, PGBK, 127.5 µm

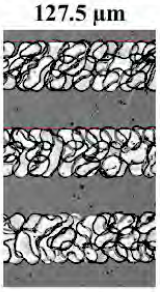

Printed background, BK, 130 µm

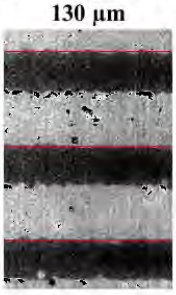

Printed background, PGBK, 130 µm

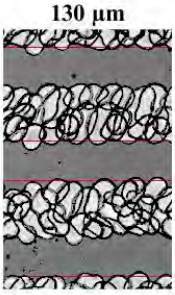

Printed bars, BK, 130 µm

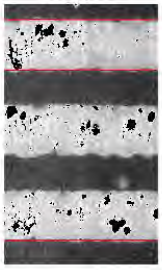

Printed bars, PGBK, 130 µm

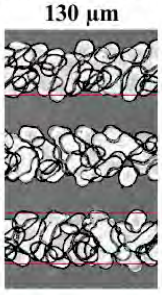

Printed background, BK, 132.5 µm

Printed background, PGBK 132.5 µm

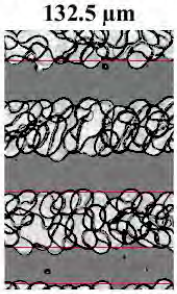

Printed bars, BK, 132.5 µm

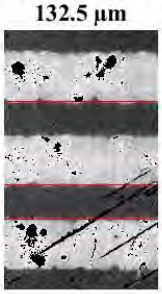

Printed bars, PGBK, 132.5 µm

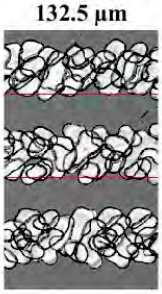

Printed background, BK, 135 µm

Printed background, PGBK, 135 µm

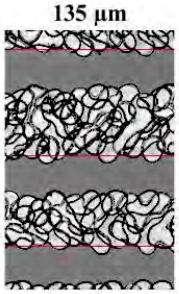

Printed bars, BK, 135 µm

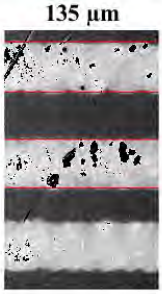

Printed bars, PGBK, 135 µm

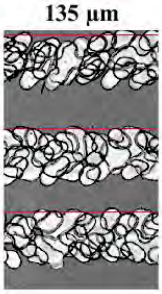

Printed background, BK, 137.5 µm

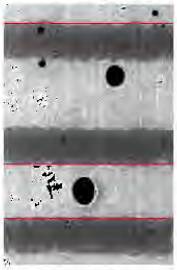

Printed background, PGBK, 137.5 µm

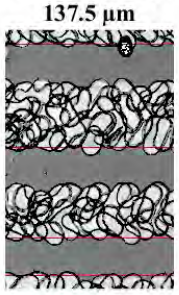

Printed bars, BK, 137.5 µm

Printed bars, PGBK, 137.5 µm

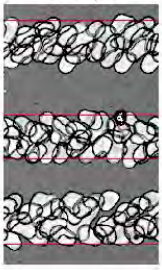

Printed background, BK, 140 µm

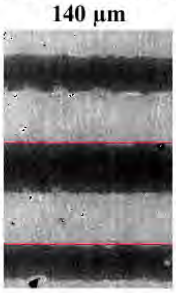

Printed background, PGBK, 140 µm

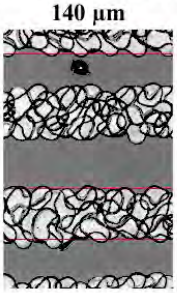

Printed bars, BK, 140 µm

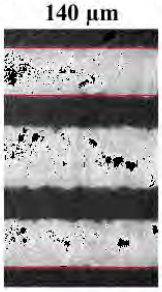

Printed bars, PGBK, 140 µm

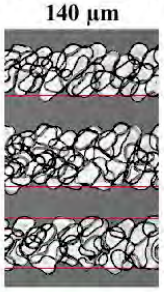

Printed background, BK, 142.5 µm

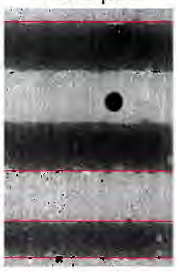

Printed background, PGBK 142.5 µm

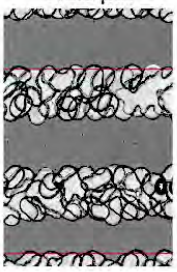

Printed bars, BK, 142.5 µm

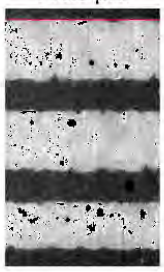

Printed bars, PGBK, 142.5 µm

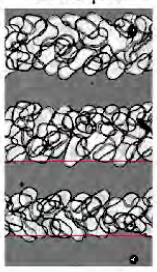

Printed background, BK, 145 µm

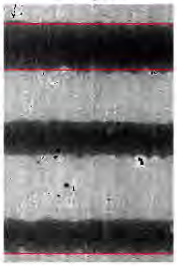

Printed background, PGBK, 145 µm

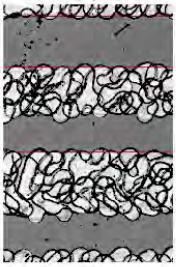

Printed bars, BK, 145 µm

Printed bars, PGBK, 145 µm

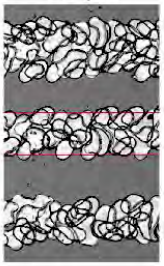

Printed background, BK, 147.5 µm

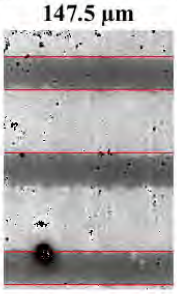

Printed background, PGBK, 147.5 µm

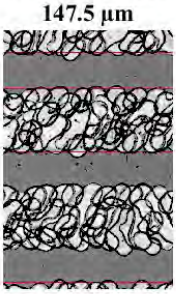

Printed bars, BK, 147.5 µm

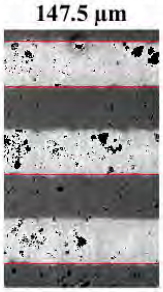

Printed bars, PGBK, 147.5 µm

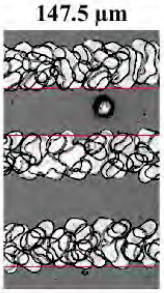

Printed background, BK, 150 µm

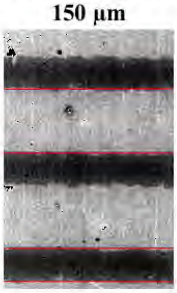

Printed background, PGBK, 150 µm

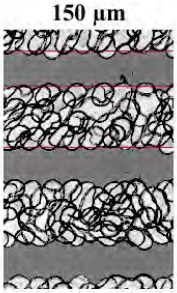

Printed bars, BK, 150 µm

Printed bars, PGBK, 150 µm

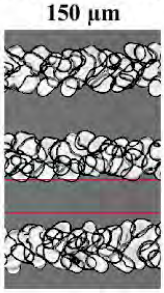

Printed background, BK, 152.5 µm

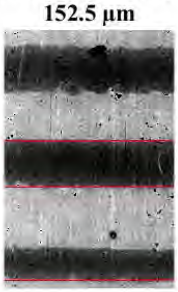

Printed background, PGBK 152.5 µm

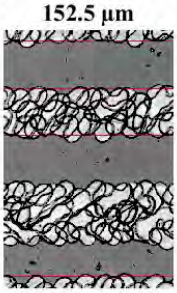

Printed bars, BK, 152.5 µm

Printed bars, PGBK, 152.5 µm

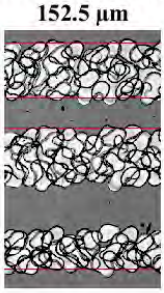

Printed background, BK, 155 µm

Printed background, PGBK, 155 µm

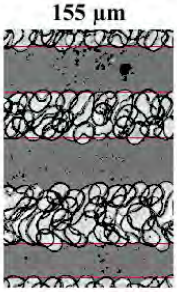

Printed bars, BK, 155 µm

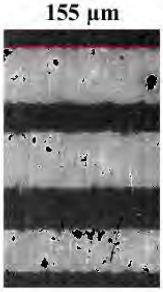

Printed bars, PGBK, 155 µm

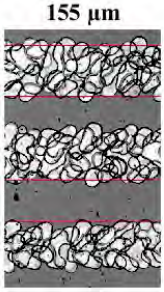

Printed background, BK, 157.5 µm

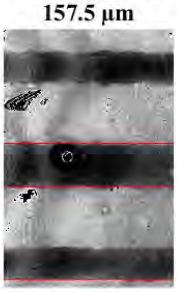

Printed background, PGBK, 157.5 µm

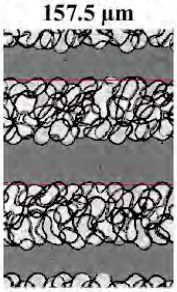

Printed bars, BK, 157.5 µm

Printed bars, PGBK, 157.5 µm

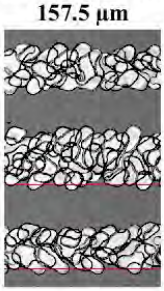

Printed background, BK, 160 µm

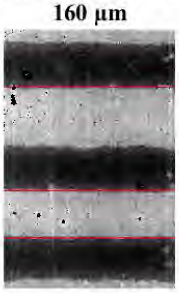

Printed background, PGBK, 160 µm

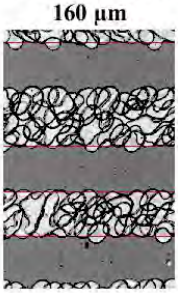

Printed bars, BK, 160 µm

Printed bars, PGBK, 160 µm

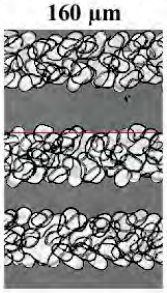

Printed background, BK, 162.5 µm

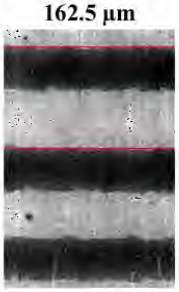

Printed background, PGBK 162.5 µm

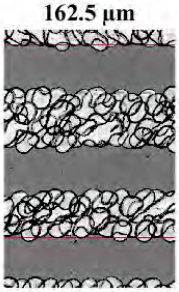

Printed bars, BK, 162.5 µm

Printed bars, PGBK, 162.5 µm

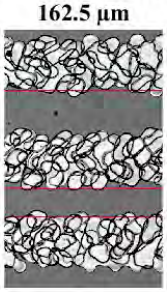

Printed background, BK, 165 µm

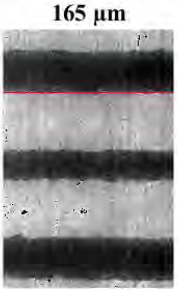

Printed background, PGBK, 165 µm

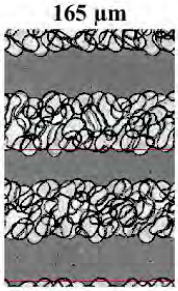

Printed bars, BK, 165 µm

Printed bars, PGBK, 165 µm

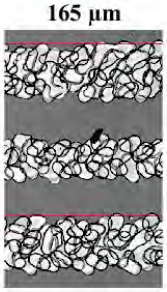

Printed background, BK, 167.5 µm

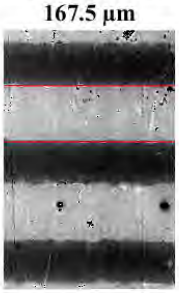

Printed background, PGBK, 167.5 µm

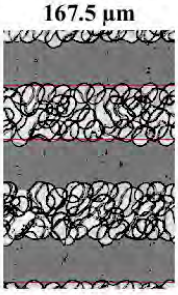

Printed bars, BK, 167.5 µm

Printed bars, PGBK, 167.5 µm

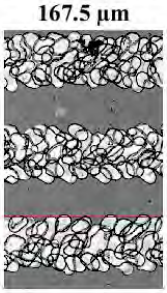

Printed background, BK, 170 µm

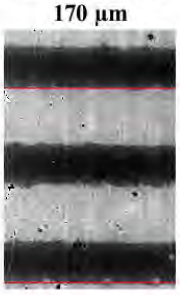

Printed background, PGBK, 170 µm

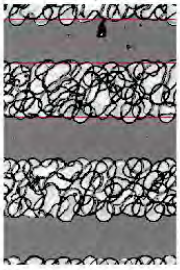

Printed bars, BK, 170 µm

Printed bars, PGBK, 170 µm

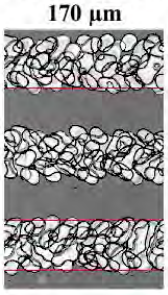

Printed background, BK, 172.5 µm

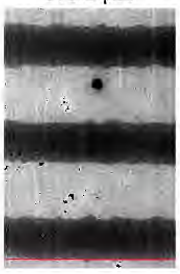

Printed background, PGBK 172.5 µm

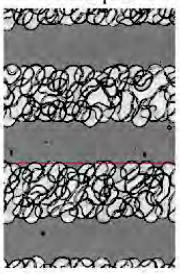

Printed bars, BK, 172.5 µm

Printed bars, PGBK, 172.5 µm

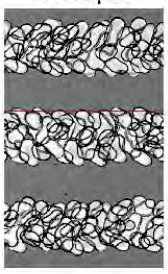

Printed background, BK, 175 µm

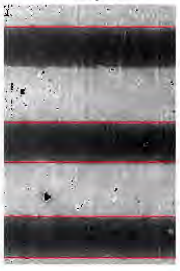

Printed background, PGBK, 175 µm

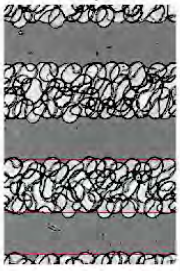

Printed bars, BK, 175 µm

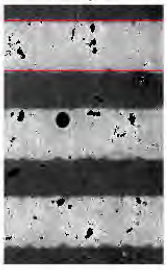

Printed bars, PGBK, 175 µm

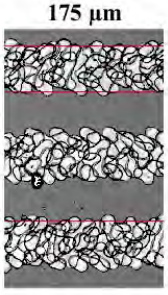

Printed background, BK, 177.5 µm

Printed background, PGBK, 177.5 µm

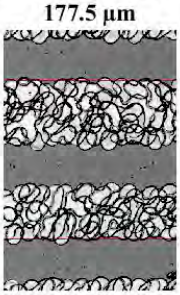

Printed bars, BK, 177.5 µm

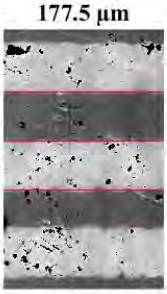

Printed bars, PGBK, 177.5 µm

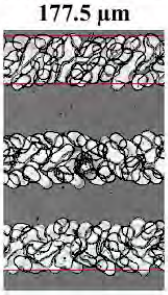

Printed background, BK, 180 µm

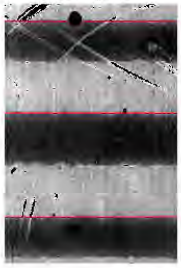

Printed background, PGBK, 180 µm

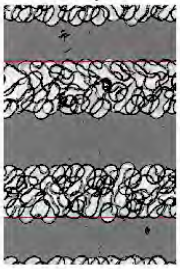

Printed bars, BK, 180 µm

Printed bars, PGBK, 180 µm

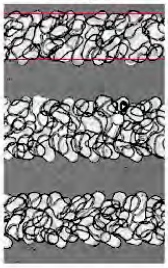

Printed background, BK, 182.5 µm

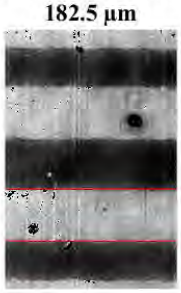

Printed background, PGBK 182.5 µm

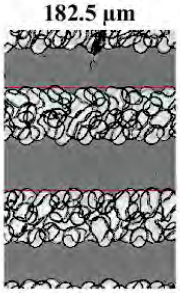

Printed bars, BK, 182.5 µm

Printed bars, PGBK, 182.5 µm

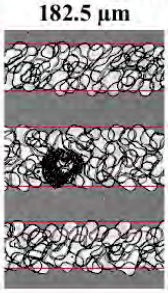

Printed background, BK, 185 µm

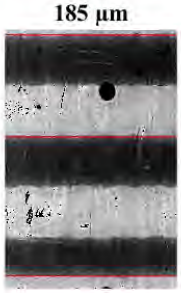

Printed background, PGBK, 185 µm

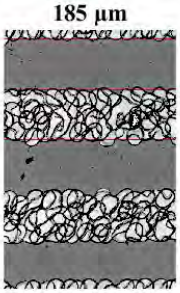

Printed bars, BK, 185 µm

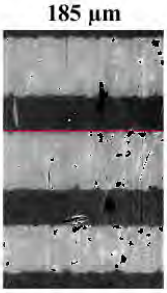

Printed bars, PGBK, 185 µm

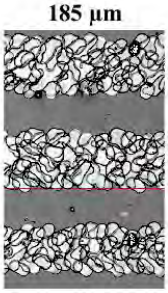

Printed background, BK, 187.5 µm

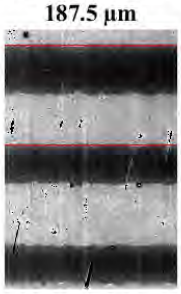

Printed background, PGBK, 187.5 µm

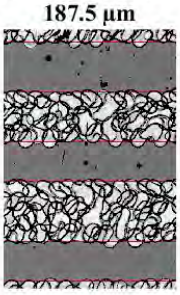

Printed bars, BK, 187.5 µm

Printed bars, PGBK, 187.5 µm

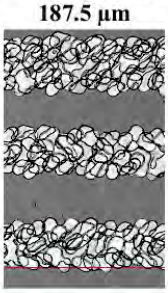

Printed background, BK, 190 µm

Printed background, PGBK, 190 µm

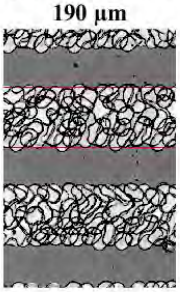

Printed bars, BK, 190 µm

Printed bars, PGBK, 190 µm

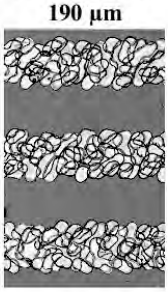

Printed background, BK, 192.5 µm

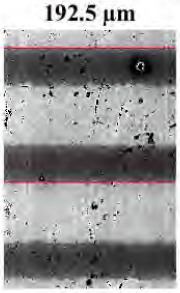

Printed background, PGBK 192.5 µm

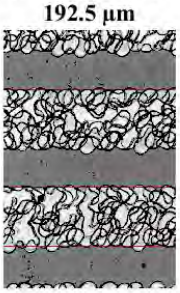

Printed bars, BK, 192.5 µm

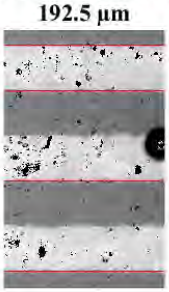

Printed bars, PGBK, 192.5 µm

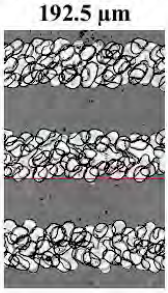

Printed background, BK, 195 µm

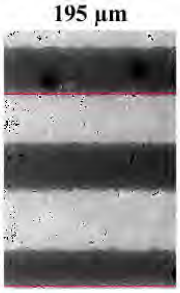

Printed background, PGBK, 195 µm

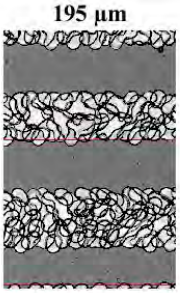

Printed bars, BK, 195 µm

Printed bars, PGBK, 195 µm

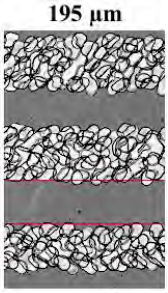

Printed background, BK, 197.5 µm

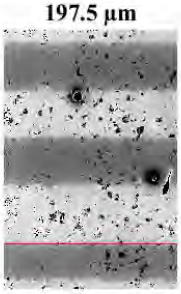

Printed background, PGBK, 197.5 µm

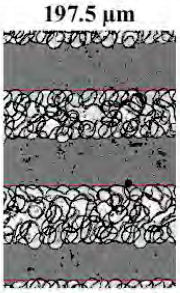

Printed bars, BK, 197.5 µm

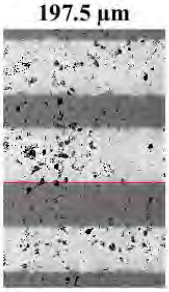

Printed bars, PGBK, 197.5 µm

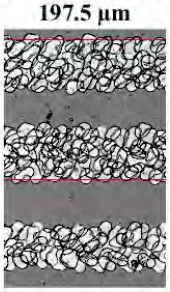

B MTF Analysis Results of the Applied Macro Lens Settings

The resolution, which is measured based on Macro lens' MTF analysis, and the calculated FOV are summarized in Table 1.

Table 1: Resolution and FOV of different macro lens' settings

Field stop f1- f3	Working distance f_w [mm]	Zoom z1-z12	Resolution [lp/mm]	FOV [mm]
1	148	1	14.10	77.78
1	148	2	16.50	70.07
1	148	3	21.64	62.73
1	148	4	22.50	56.36
1	148	5	18.57	48.01
1	148	6	37.65	41.37
1	148	7	35.68	34.42
1	148	8	48.53	29.02
1	148	9	67.22	22.74
1	148	10	91.95	18.66
1	148	11	84.43	15.65
1	148	12	97.72	13.86
1	173	1	9.32	98.46
1	173	2	13.18	89.40
1	173	3	13.79	79.37
1	173	4	22.05	70.71
1	173	5	25.35	59.38
1	173	6	13.68	50.84
1	173	7	32.72	43.45
1	173	8	28.71	35.36
1	173	9	42.19	28.60
1	173	10	61.48	22.55
1	173	11	53.99	18.92
1	173	12	67.27	17.48
1	198	1	9.05	117.85
1	198	2	8.70	106.55
1	198	3	9.17	94.86
1	198	4	15.03	82.75
1	198	5	18.72	72.69
1	198	6	24.70	61.25
1	198	7	26.34	51.17
1	198	8	31.63	42.74
1	198	9	37.18	33.53
1	198	10	35.15	26.91
1	198	11	34.30	22.81
1	198	12	22.92	20.58
1	223	1	7.24	136.46
1	223	2	6.91	123.46
1	223	3	10.97	111.12
1	223	4	10.56	98.46
1	223	5	15.75	82.75

1	223	6	17.18	71.36
1	223	7	16.61	59.83
1	223	8	18.86	49.23
1	223	9	20.19	38.89
1	223	10	26.42	31.24
1	223	11	31.43	26.55
1	223	12	23.88	23.95
1	248	1	5.85	158.74
1	248	2	9.11	138.90
1	248	3	8.98	125.45
1	248	4	11.13	111.12
1	248	5	14.98	96.03
1	248	6	17.64	81.02
1	248	7	19.91	67.64
1	248	8	11.64	55.56
1	248	9	35.77	44.70
1	248	10	30.90	35.52
1	248	11	26.28	30.03
1	248	12	35.43	27.20
1	273	1	4.73	176.78
1	273	2	7.02	155.56
1	273	3	6.50	138.90
1	273	4	9.50	123.46
1	273	5	12.18	106.55
1	273	6	12.60	90.44
1	273	7	18.96	75.52
1	273	8	20.83	62.23
1	273	9	31.67	49.86
1	273	10	35.62	39.28
1	273	11	35.92	33.67
1	273	12	35.10	30.38
1	298	1	4.10	185.19
1	298	2	4.92	165.49
1	298	3	7.57	149.58
1	298	4	6.91	129.64
1	298	5	5.43	114.38
1	298	6	4.16	96.03
1	298	7	4.09	79.37
1	298	8	2.26	65.36
1	298	9	3.62	51.51
1	298	10	3.14	40.51
1	298	11	3.57	34.27
1	298	12	3.35	31.62
2	148	1	22.92	80.19
2	148	2	24.61	74.08
2	148	3	28.00	63.24
2	148	4	38.51	56.36

2	148	5	40.94	48.61
2	148	6	44.75	41.37
2	148	7	50.78	34.57
2	148	8	33.39	28.81
2	148	9	64.50	22.88
2	148	10	101.75	18.13
2	148	11	78.10	15.16
2	148	12	90.42	13.86
2	173	1	17.65	99.72
2	173	2	21.28	89.40
2	173	3	20.82	80.19
2	173	4	28.20	69.45
2	173	5	21.16	59.83
2	173	6	44.45	52.20
2	173	7	42.55	43.45
2	173	8	29.45	35.84
2	173	9	43.76	28.39
2	173	10	62.77	22.74
2	173	11	50.49	19.21
2	173	12	55.37	17.32
2	198	1	16.08	123.46
2	198	2	17.23	108.03
2	198	3	28.34	97.23
2	198	4	21.82	85.47
2	198	5	33.44	73.38
2	198	6	28.58	63.24
2	198	7	31.06	51.85
2	198	8	31.03	42.97
2	198	9	33.68	34.11
2	198	10	25.80	27.58
2	198	11	69.91	22.56
2	198	12	26.21	20.74
2	223	1	11.88	141.42
2	223	2	17.81	125.45
2	223	3	14.41	111.12
2	223	4	21.20	98.46
2	223	5	30.09	84.55
2	223	6	27.01	72.02
2	223	7	33.69	59.83
2	223	8	45.26	49.54
2	223	9	38.95	39.89
2	223	10	34.57	31.36
2	223	11	35.80	26.73
2	223	12	33.13	24.01
2	248	1	12.20	158.74
2	248	2	13.55	141.42
2	248	3	11.34	127.51

2	248	4	22.01	111.12
2	248	5	20.16	93.71
2	248	6	23.17	81.02
2	248	7	27.05	68.23
2	248	8	31.09	54.78
2	248	9	36.54	44.19
2	248	10	31.35	35.52
2	248	11	30.51	30.15
2	248	12	30.83	27.20
2	273	1	10.98	172.85
2	273	2	13.03	158.74
2	273	3	9.96	138.90
2	273	4	16.56	121.53
2	273	5	12.53	105.11
2	273	6	17.22	91.51
2	273	7	31.15	75.52
2	273	8	28.40	62.23
2	273	9	33.45	49.54
2	273	10	32.70	39.09
2	273	11	36.33	33.24
2	273	12	34.04	30.38
2	298	1	10.03	194.45
2	298	2	10.33	172.85
2	298	3	7.02	152.51
2	298	4	6.45	129.64
2	298	5	5.37	112.73
2	298	6	4.99	96.03
2	298	7	5.44	79.37
2	298	8	4.73	65.36
2	298	9	4.58	53.28
2	298	10	4.61	41.59
2	298	11	4.24	35.04
2	298	12	3.68	30.87
3	148	1	20.51	80.19
3	148	2	20.28	74.08
3	148	3	23.92	65.36
3	148	4	29.73	55.96
3	148	5	26.38	49.23
3	148	6	39.66	41.37
3	148	7	45.15	34.88
3	148	9	53.38	22.83
3	148	10	138.30	18.30
3	148	11	144.92	15.28
3	148	12	144.92	14.06
3	173	1	46.51	528.58
3	173	2	19.74	92.60
3	173	3	23.22	79.37

3	173	4	23.11	71.36
3	173	5	30.79	61.25
3	173	6	36.48	51.85
3	173	7	37.35	44.70
3	173	8	45.38	36.35
3	173	9	29.78	29.40
3	173	10	46.67	22.56
3	173	11	38.80	19.02
3	173	12	82.81	17.64
3	198	1	9.40	123.46
3	198	2	12.52	109.55
3	198	3	13.11	97.23
3	198	4	12.04	87.40
3	198	5	22.26	72.69
3	198	6	32.25	61.25
3	198	7	24.98	50.51
3	198	8	20.66	42.50
3	198	9	43.44	33.97
3	198	10	42.65	26.73
3	198	11	34.97	23.38
3	198	12	66.29	20.86
3	223	1	7.92	136.46
3	223	2	9.91	127.51
3	223	3	11.76	112.73
3	223	4	24.08	97.23
3	223	5	17.46	85.47
3	223	6	18.66	71.36
3	223	7	29.07	61.73
3	223	8	24.00	48.92
3	223	9	38.25	39.68
3	223	10	41.63	31.36
3	223	11	40.60	26.58
3	223	12	37.44	23.95
3	248	1	9.69	152.51
3	248	2	14.53	144.04
3	248	3	12.52	127.51
3	248	4	18.21	112.73
3	248	5	16.99	94.86
3	248	6	19.46	86.42
3	248	7	20.83	68.23
3	248	8	28.29	55.56
3	248	9	34.84	44.45
3	248	10	27.35	35.20
3	273	1	7.83	180.89
3	273	2	8.54	155.56
3	273	3	10.11	141.42
3	273	4	14.20	121.53

3	273	5	15.90	106.55
3	273	6	15.40	91.51
3	273	7	20.61	74.79
3	273	8	23.80	62.23
3	273	9	20.65	49.54
3	273	10	36.77	39.48
3	273	11	20.46	33.24
3	273	12	13.38	29.24
3	298	1	7.57	194.45
3	298	2	9.48	172.85
3	298	4	12.11	149.58
3	298	5	13.64	131.83
3	298	6	12.50	114.38
3	298	7	12.75	97.23
3	298	8	9.16	80.19
3	298	9	11.28	66.48
3	298	10	8.64	53.28
3	298	11	6.74	35.04

C WFS Measurement of the Tube Lens' Positioning

The shape of wavefront sample 4, which is measured by the WFS, is shown in Figure 1. The color map indicates the shape of the wavefront.

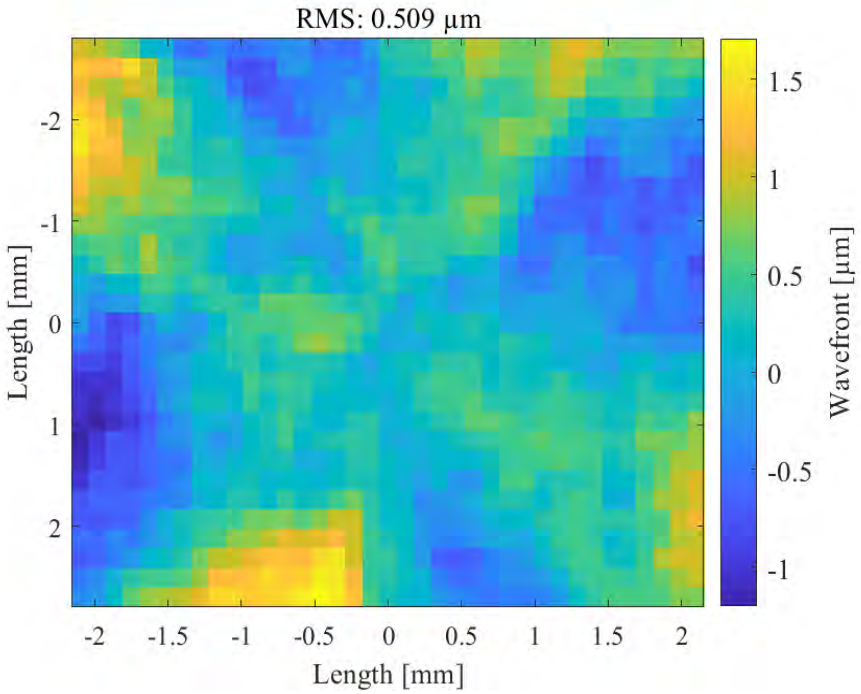

Figure 1: The wavefront's shape of wavefront sample 4 is imaged by the scaled color. The measured RMS of this wavefront is 0.509 µm.

The mean RMS error using the final tube lens position is measured by 20 samples. The measurement data is plotted in Figure 2.

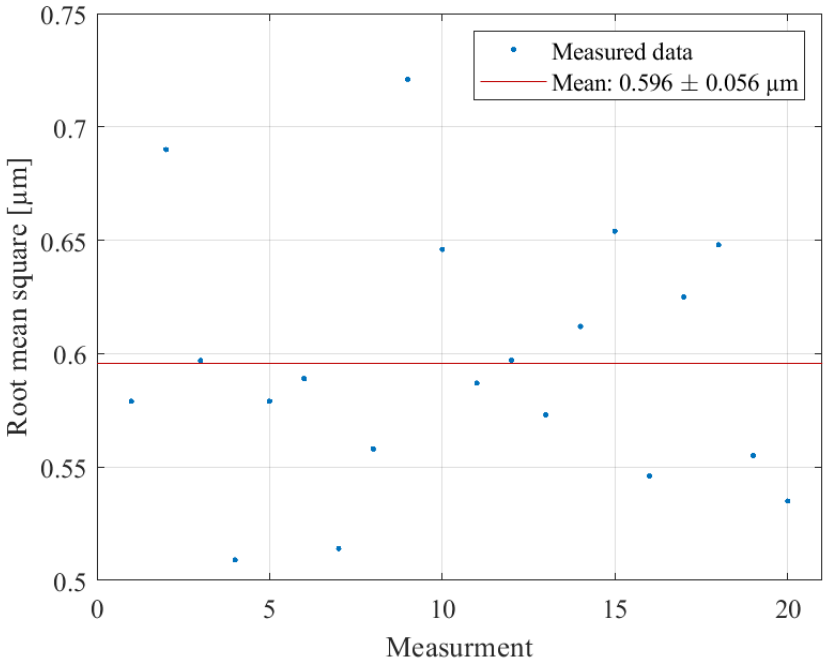

Figure 2: On average, the RMS error of the wavefronts is 0.596 ± 0.056 µm using the final tube lens position.

D Captured Spot Areas of Different Applied LED Distances

During the illumination adjustment of the lithography system, the distance d between the LED housing and the mask plane is enlarged from 18.8 mm up to 93.8 mm in a step size of 5 mm. The respective illumination distribution in the spot area is captured by a camera in the substrate plane. The camera image and the respective histogram of the illumination distribution in the spot area are shown in Figures 1 to 16.

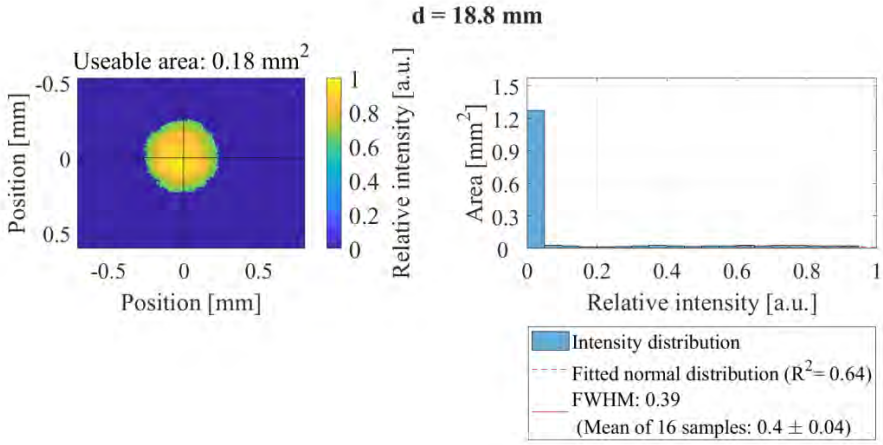

Figure 1: The homogeneity of the illumination in the substrate plane is evaluated according to the intensity distribution (left) and the respective histogram (right). The set distance d between the LED housing and the mask plane is 18.8 mm.

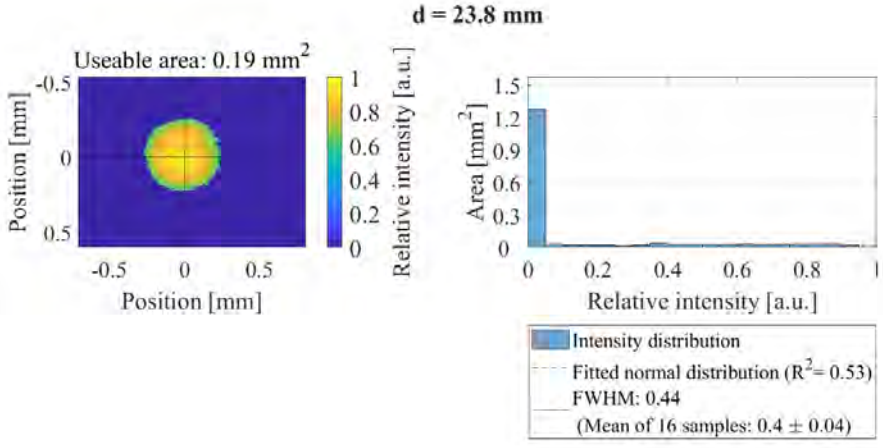

Figure 2: The homogeneity of the illumination in the substrate plane is evaluated according to the intensity distribution (left) and the respective histogram (right). The set distance d between the LED housing and the mask plane is 23.8 mm.

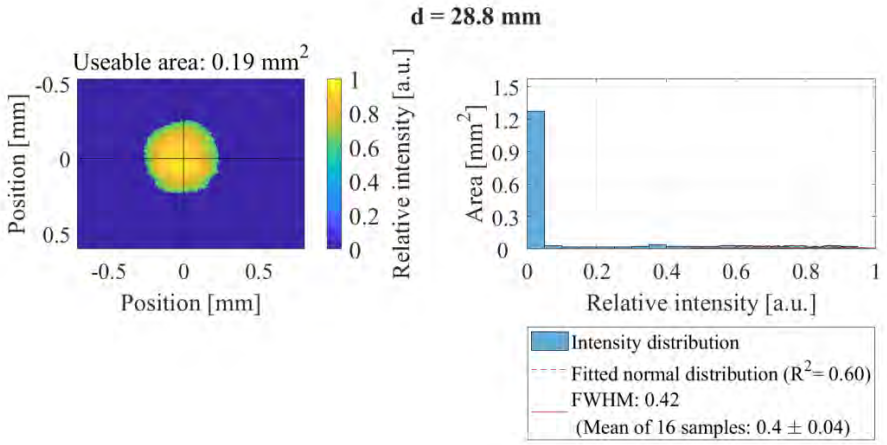

Figure 3: The homogeneity of the illumination in the substrate plane is evaluated according to the intensity distribution (left) and the respective histogram (right). The set distance d between the LED housing and the mask plane is 28.8 mm.

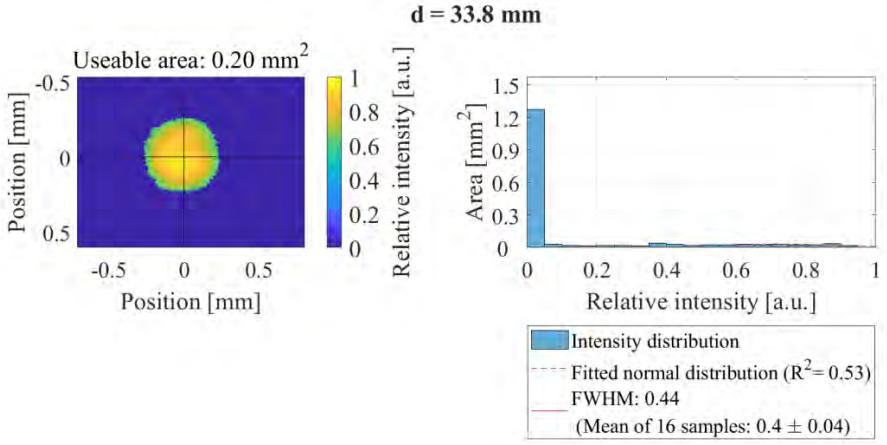

Figure 4: The homogeneity of the illumination in the substrate plane is evaluated according to the intensity distribution (left) and the respective histogram (right). The set distance d between the LED housing and the mask plane is 33.8 mm.

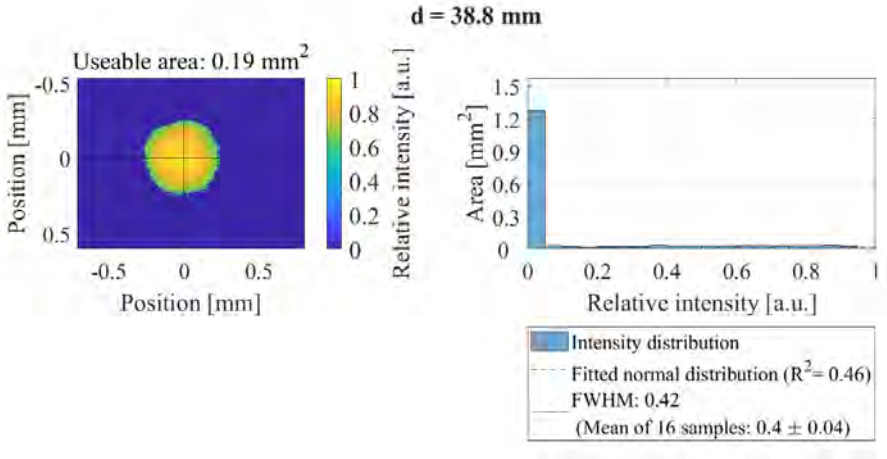

Figure 5: The homogeneity of the illumination in the substrate plane is evaluated according to the intensity distribution (left) and the respective histogram (right). The set distance d between the LED housing and the mask plane is 38.8 mm.

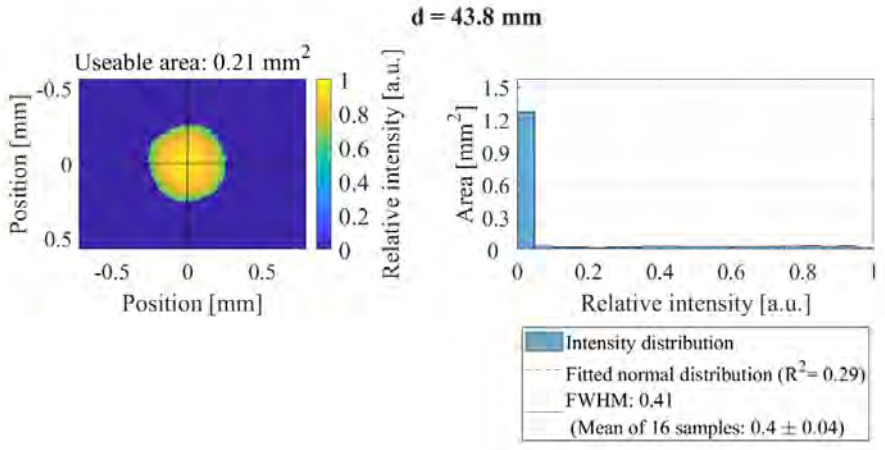

Figure 6: The homogeneity of the illumination in the substrate plane is evaluated according to the intensity distribution (left) and the respective histogram (right). The set distance d between the LED housing and the mask plane is 43.8 mm.

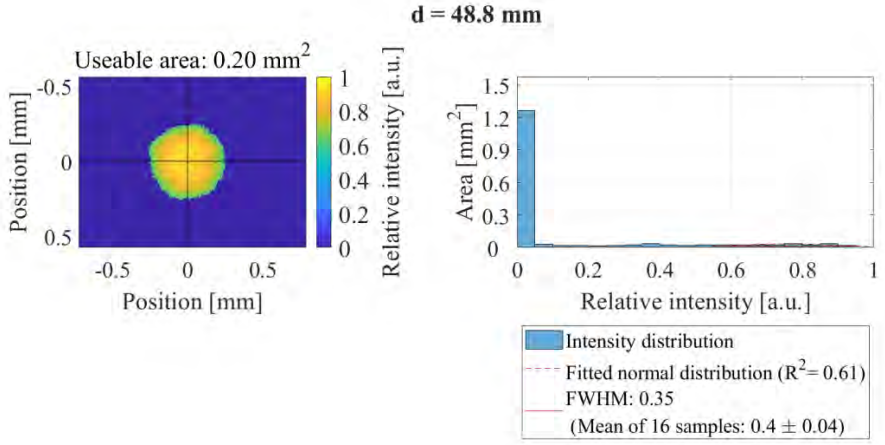

Figure 7: The homogeneity of the illumination in the substrate plane is evaluated according to the intensity distribution (left) and the respective histogram (right). The set distance d between the LED housing and the mask plane is 48.8 mm.

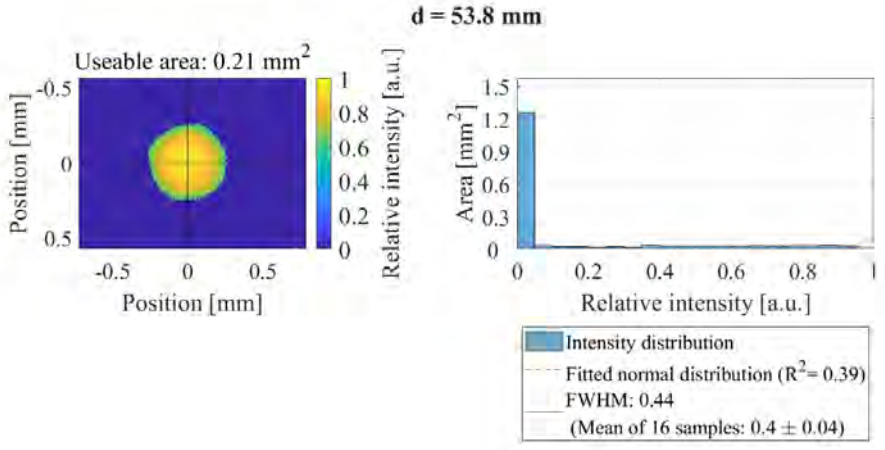

Figure 8: The homogeneity of the illumination in the substrate plane is evaluated according to the intensity distribution (left) and the respective histogram (right). The set distance d between the LED housing and the mask plane is 53.8 mm.

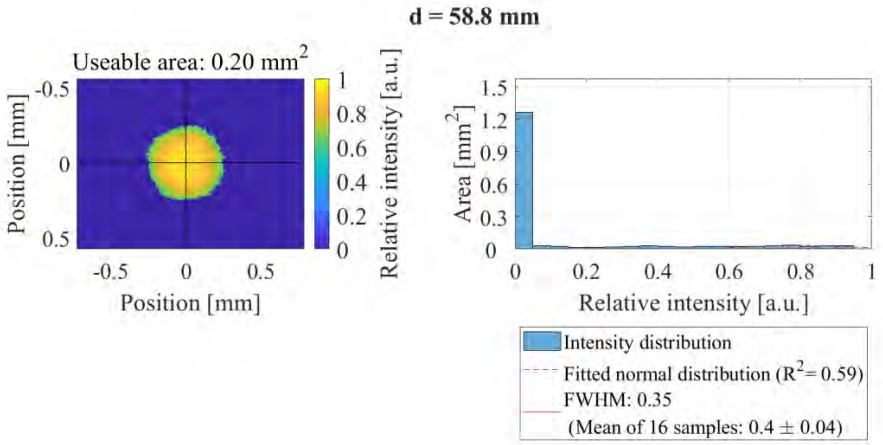

Figure 9: The homogeneity of the illumination in the substrate plane is evaluated according to the intensity distribution (left) and the respective histogram (right). The set distance d between the LED housing and the mask plane is 58.8 mm.

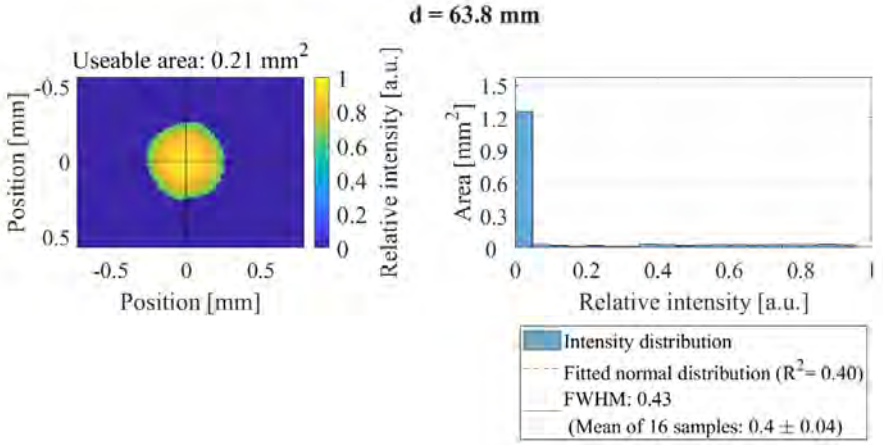

Figure 10: The homogeneity of the illumination in the substrate plane is evaluated according to the intensity distribution (left) and the respective histogram (right). The set distance d between the LED housing and the mask plane is 63.8 mm.

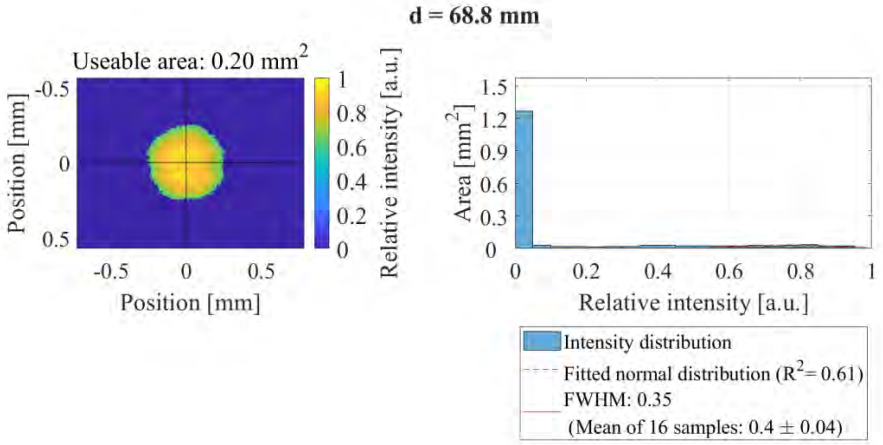

Figure 11: The homogeneity of the illumination in the substrate plane is evaluated according to the intensity distribution (left) and the respective histogram (right). The set distance d between the LED housing and the mask plane is 68.8 mm.

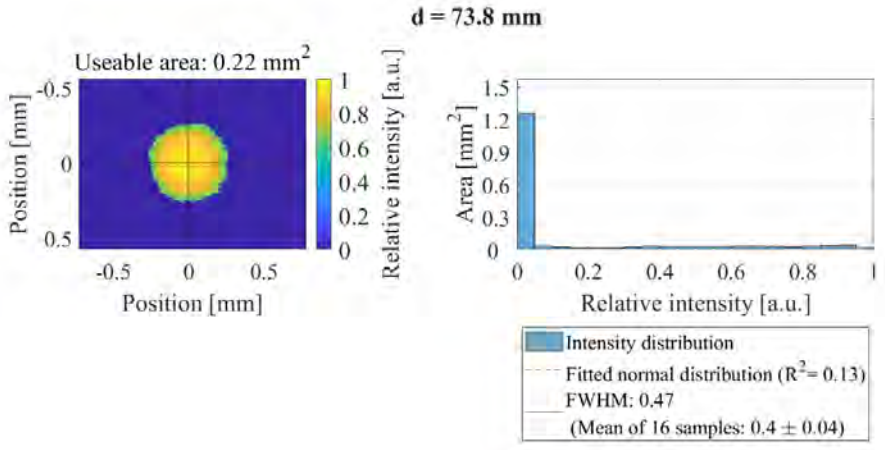

Figure 12: The homogeneity of the illumination in the substrate plane is evaluated according to the intensity distribution (left) and the respective histogram (right). The set distance d between the LED housing and the mask plane is 73.8 mm.

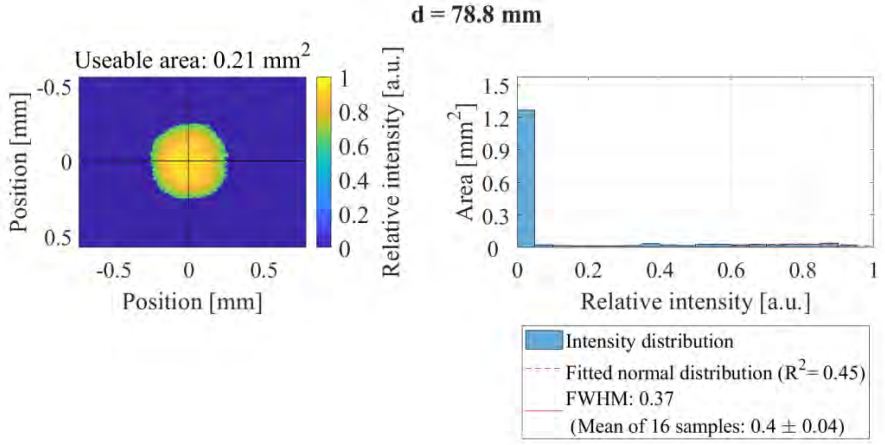

Figure 13: The homogeneity of the illumination in the substrate plane is evaluated according to the intensity distribution (left) and the respective histogram (right). The set distance d between the LED housing and the mask plane is 78.8 mm.

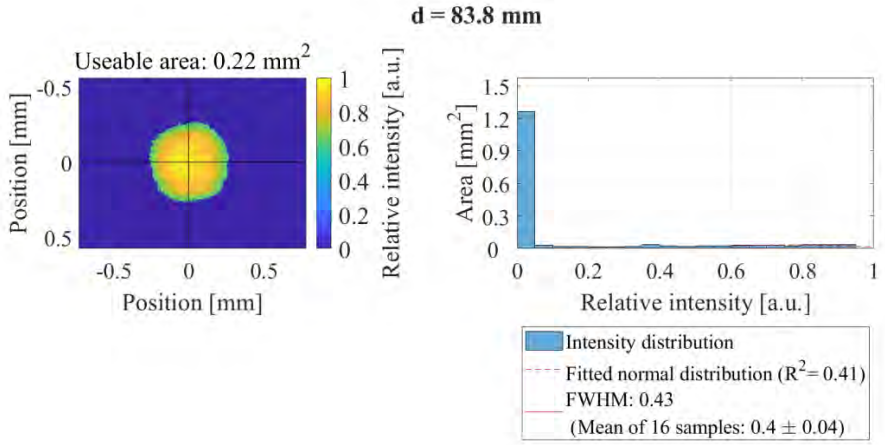

Figure 14: The homogeneity of the illumination in the substrate plane is evaluated according to the intensity distribution (left) and the respective histogram (right). The set distance d between the LED housing and the mask plane is 83.8 mm.

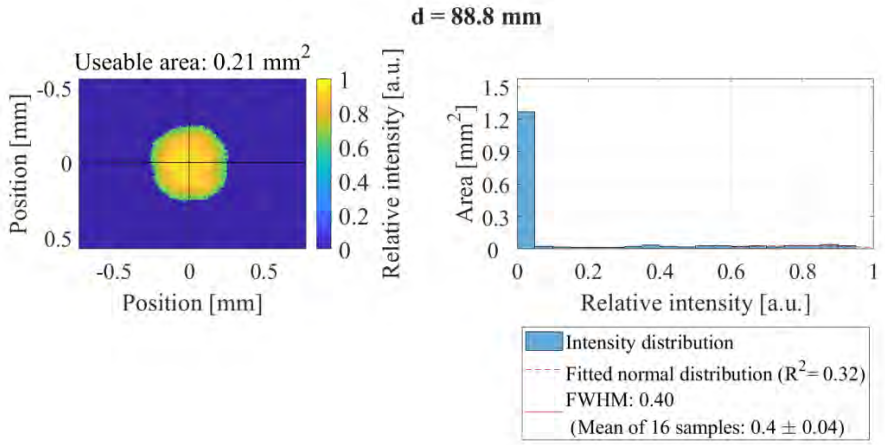

Figure 15: The homogeneity of the illumination in the substrate plane is evaluated according to the intensity distribution (left) and the respective histogram (right). The set distance d between the LED housing and the mask plane is 88.8 mm.

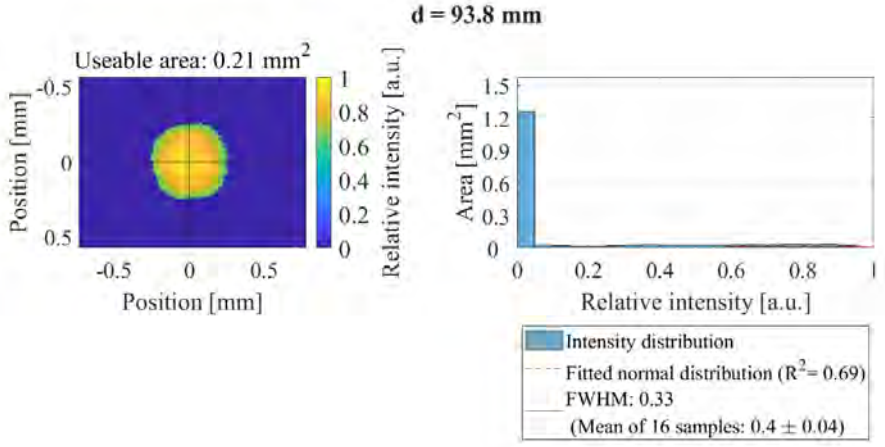

Figure 16: The homogeneity of the illumination in the substrate plane is evaluated according to the intensity distribution (left) and the respective histogram (right). The set distance d between the LED housing and the mask plane is 93.8 mm.

E Spot Areas Using a Kepler Telescope in the Illumination Unit

The intensity distribution in the spot area using the final Kepler illumination is captured by a camera sensor in the substrate plane. Since the camera sensor noise causes invalid High Dynamic Range Image images, the standard deviation of FWHM is based on 16 random samples.

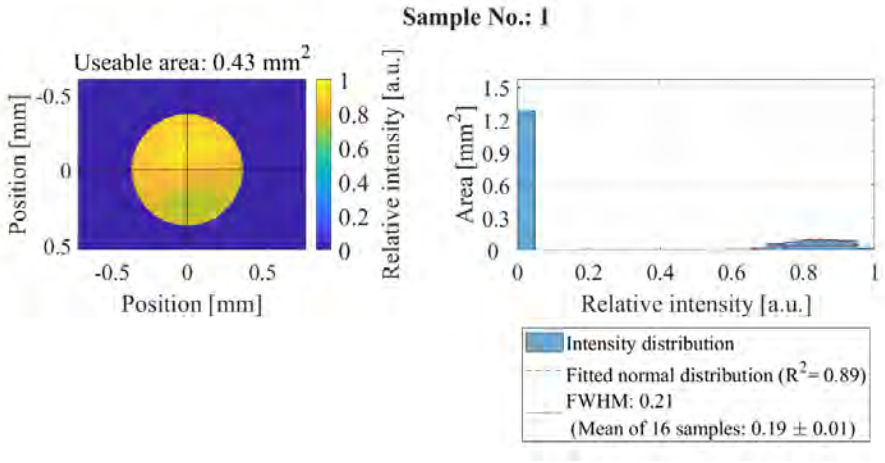

Figure 1: The homogeneity of the illumination in the substrate plane is evaluated according to the intensity distribution (left) and the respective histogram (right). The shown sample is the first one of 16 samples.

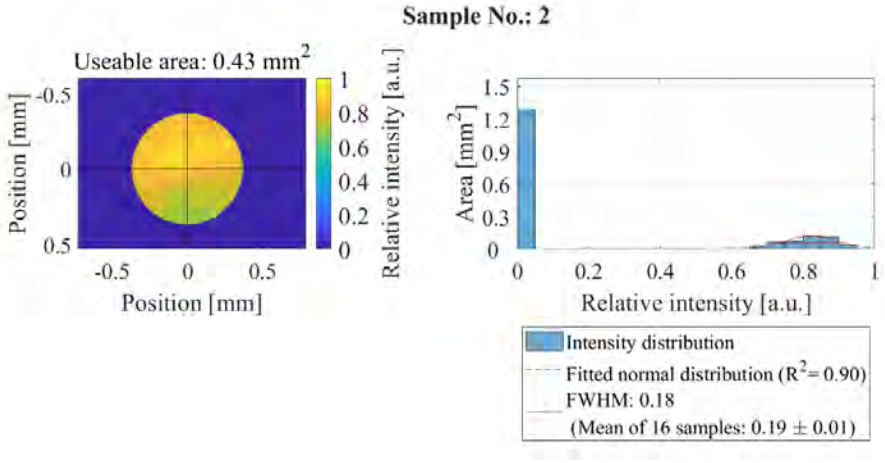

Figure 2: The homogeneity of the illumination in the substrate plane is evaluated according to the intensity distribution (left) and the respective histogram (right). The shown sample is the second one of 16 samples.

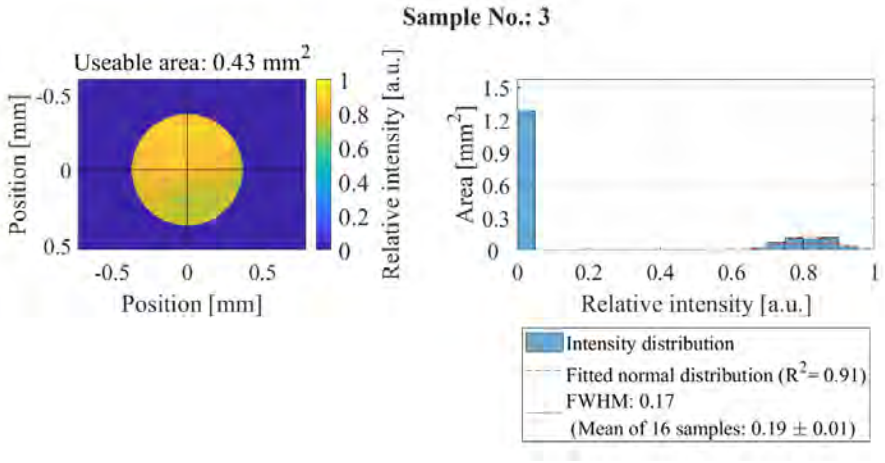

Figure 3: The homogeneity of the illumination in the substrate plane is evaluated according to the intensity distribution (left) and the respective histogram (right). The shown sample is the third one of 16 samples.

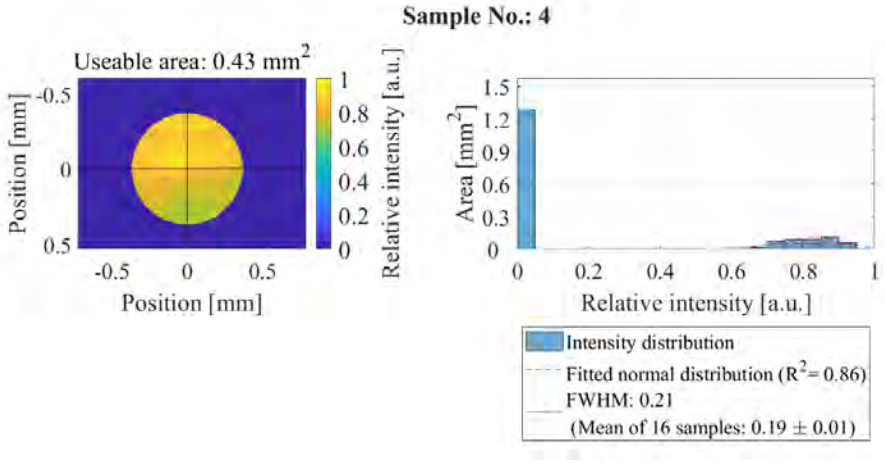

Figure 4: The homogeneity of the illumination in the substrate plane is evaluated according to the intensity distribution (left) and the respective histogram (right). The shown sample is the fourth one of 16 samples.

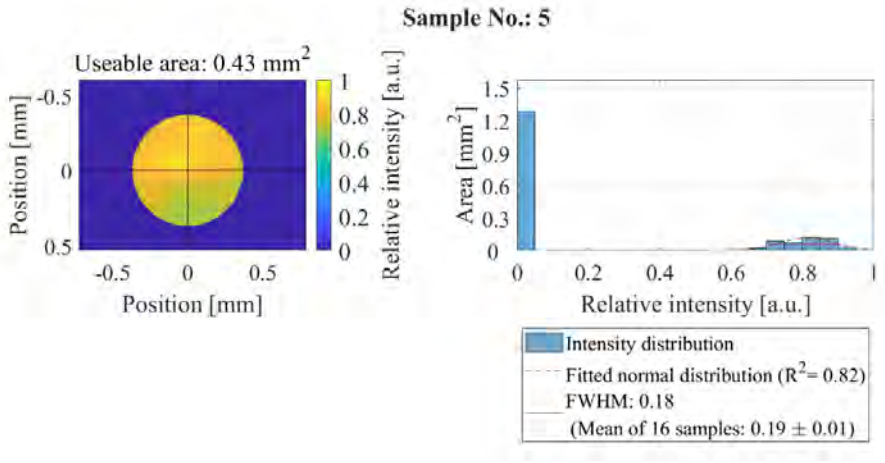

Figure 5: The homogeneity of the illumination in the substrate plane is evaluated according to the intensity distribution (left) and the respective histogram (right). The shown sample is the fifth one of 16 samples.

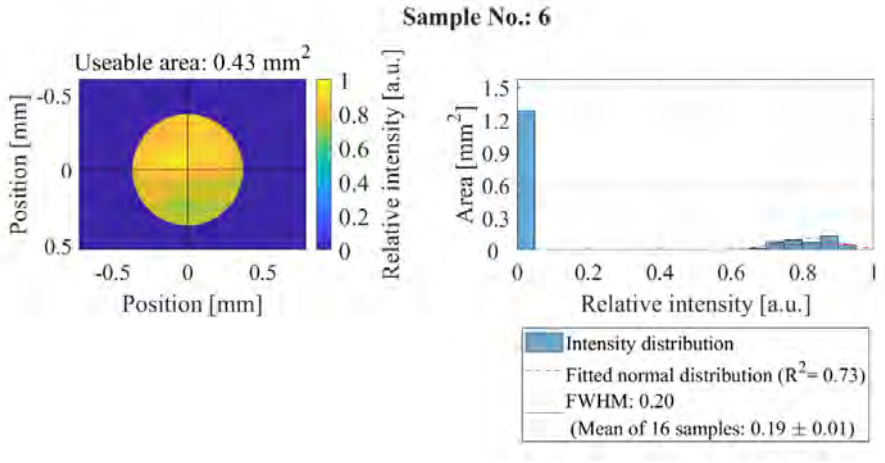

Figure 6: The homogeneity of the illumination in the substrate plane is evaluated according to the intensity distribution (left) and the respective histogram (right). The shown sample is the sixth one of 16 samples.

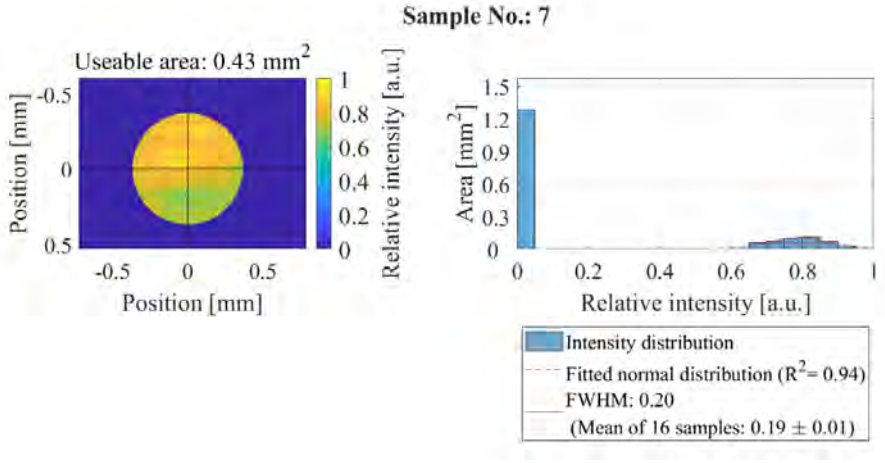

Figure 7: The homogeneity of the illumination in the substrate plane is evaluated according to the intensity distribution (left) and the respective histogram (right). The shown sample is the seventh one of 16 samples.

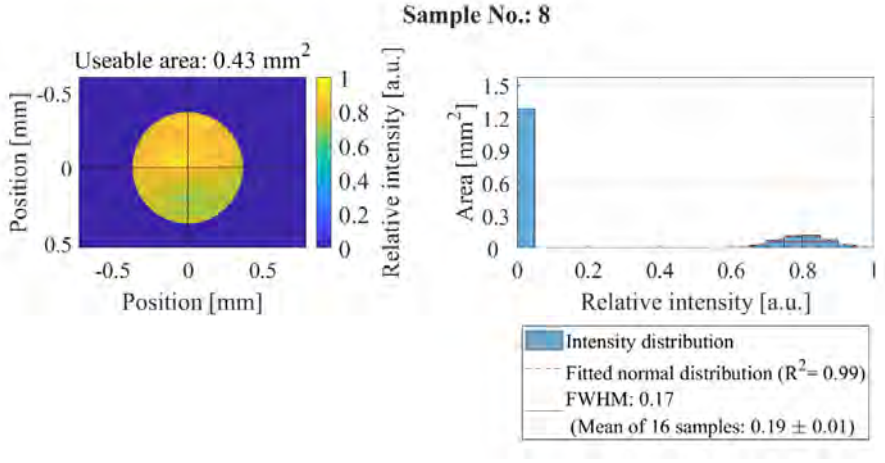

Figure 8: The homogeneity of the illumination in the substrate plane is evaluated according to the intensity distribution (left) and the respective histogram (right). The shown sample is the eighth one of 16 samples.

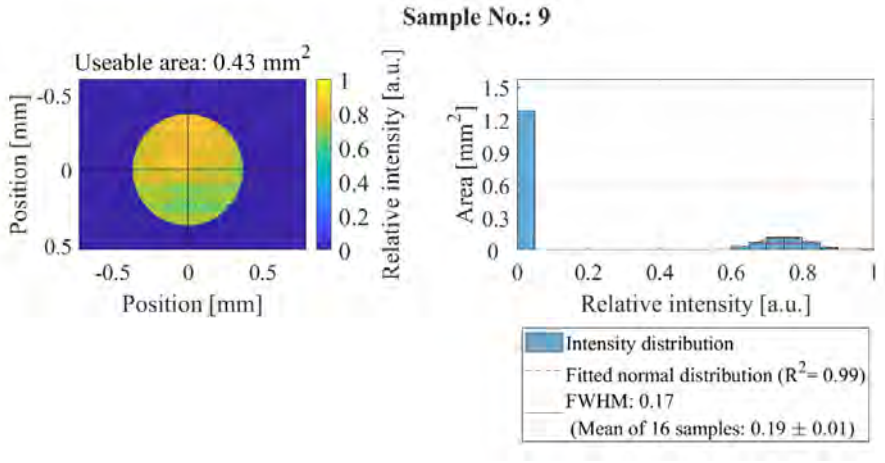

Figure 9: The homogeneity of the illumination in the substrate plane is evaluated according to the intensity distribution (left) and the respective histogram (right). The shown sample is the ninth one of 16 samples.

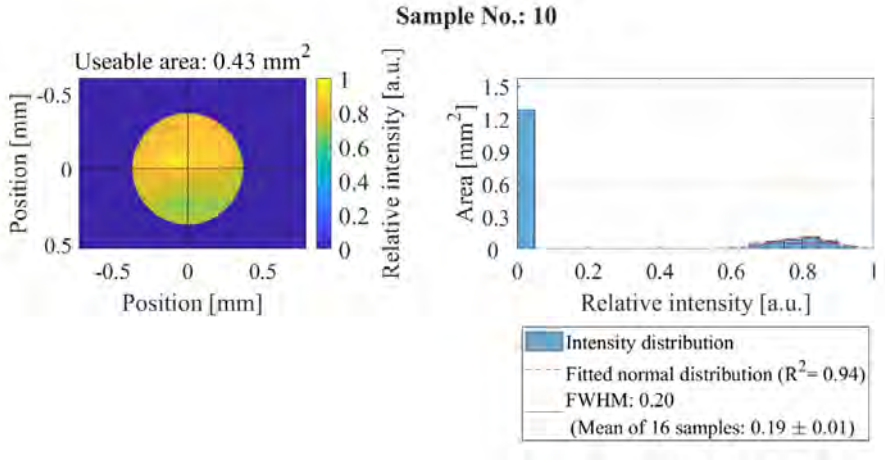

Figure 10: The homogeneity of the illumination in the substrate plane is evaluated according to the intensity distribution (left) and the respective histogram (right). The shown sample is the tenth one of 16 samples.

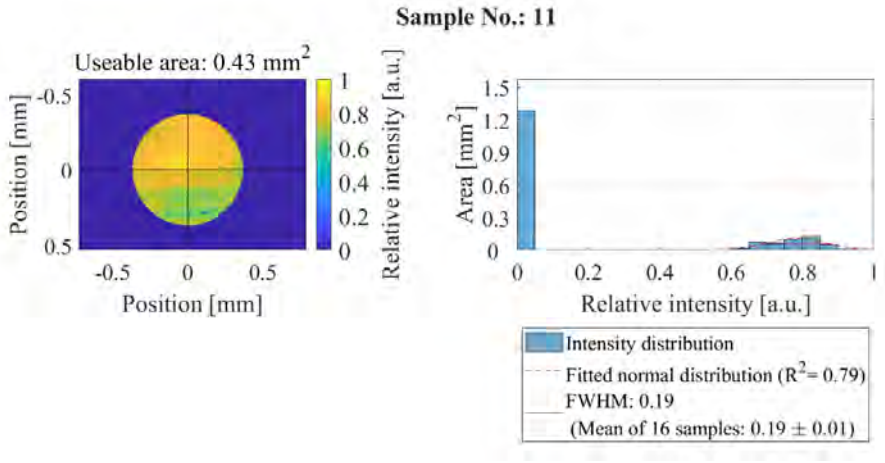

Figure 11: The homogeneity of the illumination in the substrate plane is evaluated according to the intensity distribution (left) and the respective histogram (right). The shown sample is the eleventh one of 16 samples.

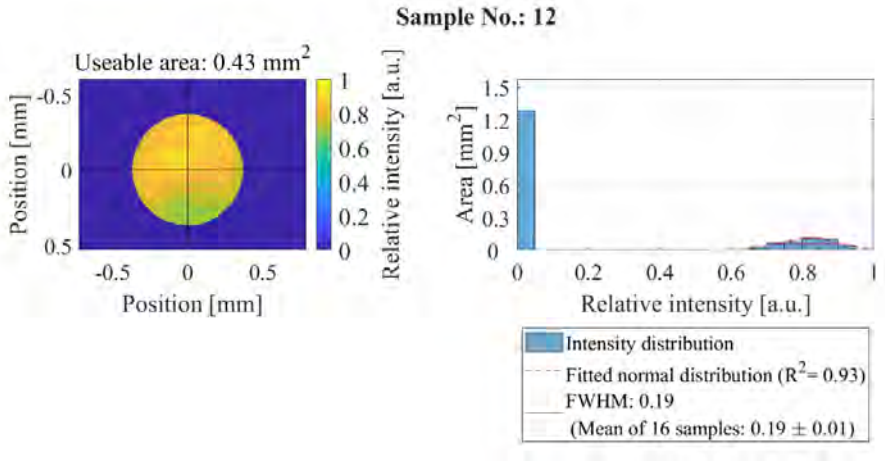

Figure 12: The homogeneity of the illumination in the substrate plane is evaluated according to the intensity distribution (left) and the respective histogram (right). The shown sample is the 12th one of 16 samples.

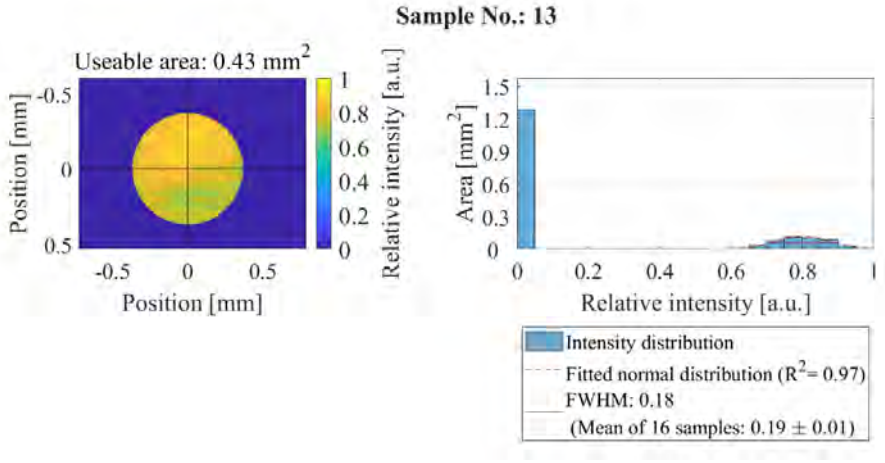

Figure 13: The homogeneity of the illumination in the substrate plane is evaluated according to the intensity distribution (left) and the respective histogram (right). The shown sample is the 13th one of 16 samples.

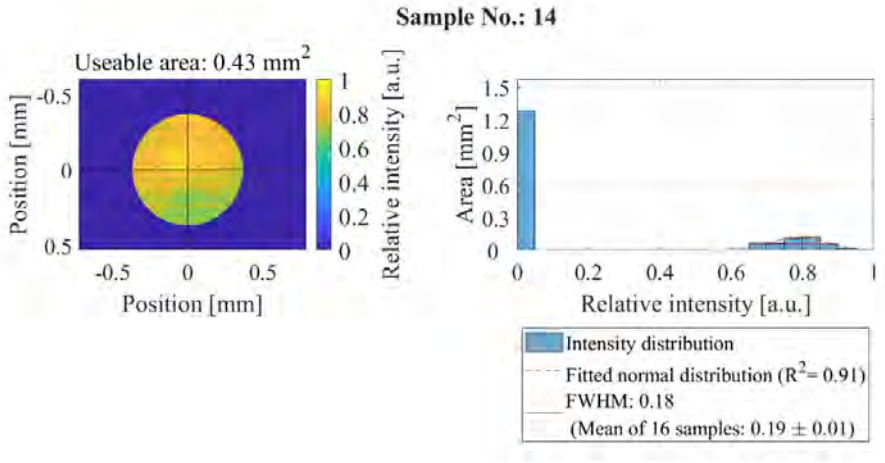

Figure 14: The homogeneity of the illumination in the substrate plane is evaluated according to the intensity distribution (left) and the respective histogram (right). The shown sample is the 14th one of 16 samples.

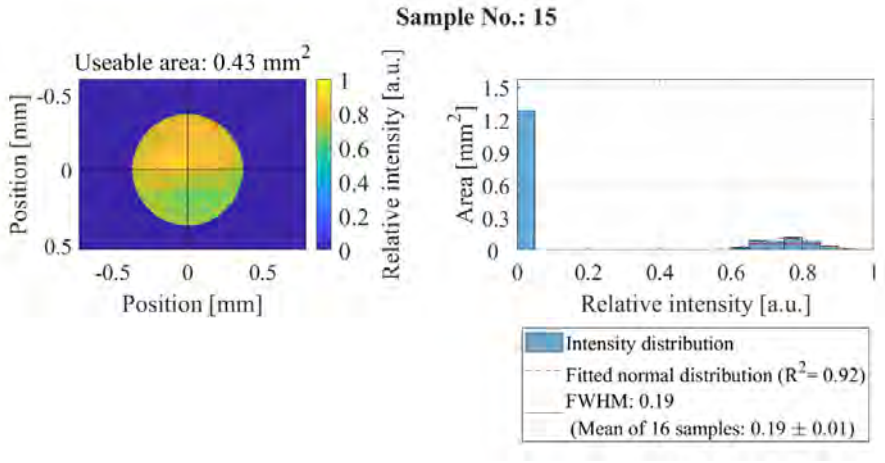

Figure 15: The homogeneity of the illumination in the substrate plane is evaluated according to the intensity distribution (left) and the respective histogram (right). The shown sample is the 15th one of 16 samples.

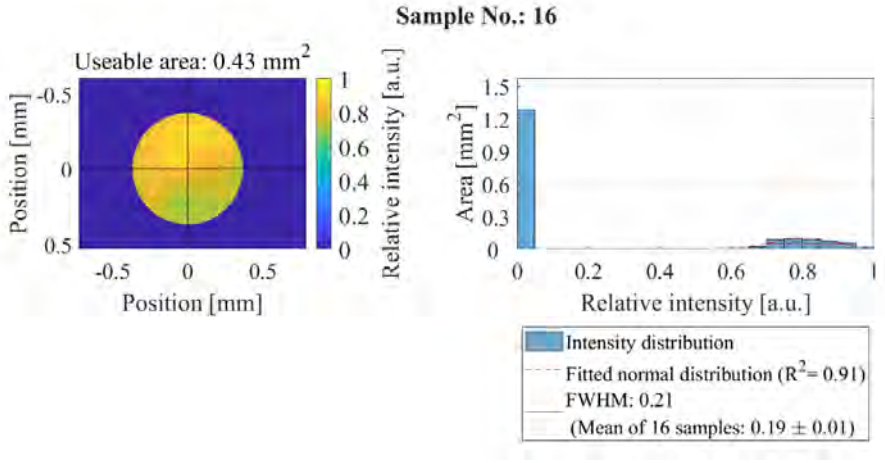

Figure 16: The homogeneity of the illumination in the substrate plane is evaluated according to the intensity distribution (left) and the respective histogram (right). The shown sample is the 16th one of 16 samples.

F Illumination Check After the Movement of the Tube Lens

The measurement results of the illumination check after the tube lens' adjustment are shown in Figure 1. The illumination's homogeneity in the substrate plane corresponds to a FWHM of 0.19. Since the difference from 0.19 to the previously calculated 0.17 is lower than the measurement uncertainty, it is assumed that the impact of the system's change is negligible.

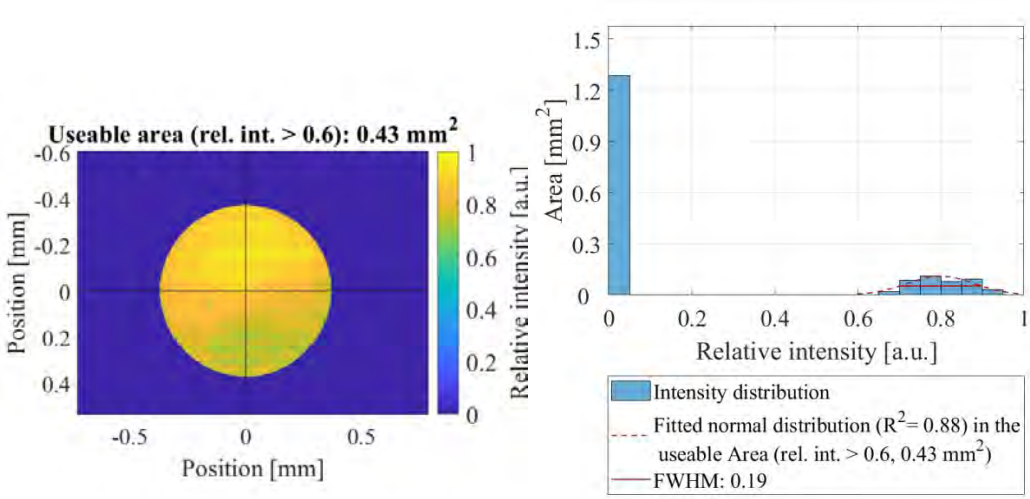

Figure 1: The homogeneity of the illumination in the substrate plane is evaluated according to the intensity distribution (left) and the respective histogram (right).

G Power Measurement of Different LED Settings

In the power analysis, the current is set to 0.7 A as well as 1.2 A. In addition, the aperture is altered and the LED controller is replaced. Since a power jump occurs in each setting, the LED controller and the current setting are excluded as an error source of the power jumps.

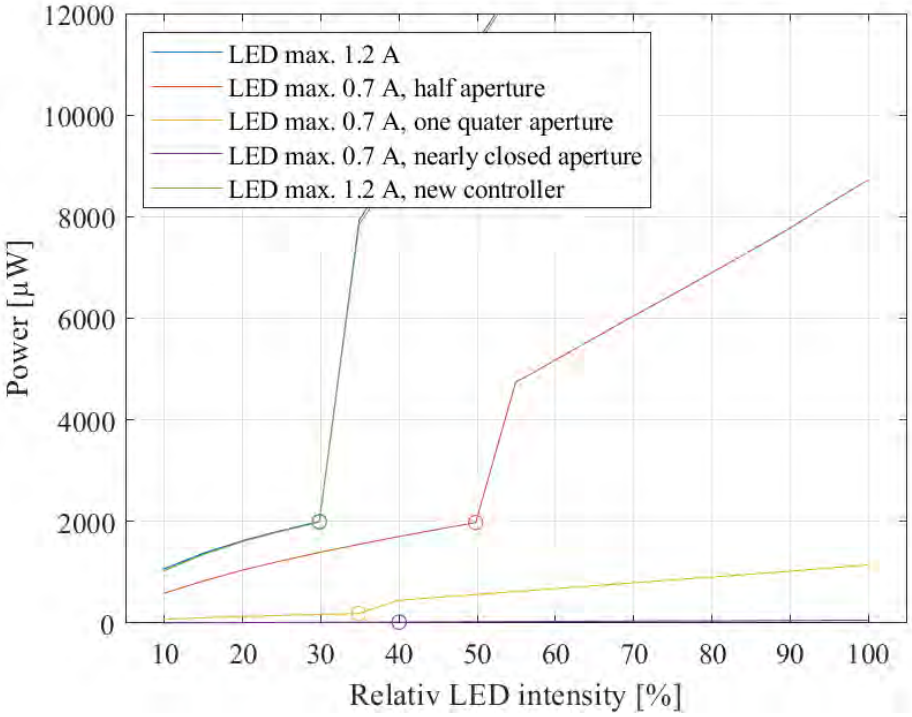

Figure 1: In the analysis of the exposure power, the current is set to 0.7 A as well as 1.2 A, the aperture is altered, and the LED controller is replaced. A power jump occurs in the measured power curve of each setting.

H Look-up Table of Possible Exposure Power And Time Settings

A look-up table is generated based on the measured power in the substrate plane. For example, possible exposure power and time settings for an exposure dose of 110 mJ/cm² are shown in Table 1.

Table 1: Look-up table for possible exposure power and time settings.

Intensity with filter [%]	Mean [µW]	Mean [µW]	Mean [µW]	Mean	Std
60	370,8	370,7	370,8	370,7666667	0,047140452
64,71	400,3	400,1	400,1	400,1666667	0,094280904
69,8	432,3	431,8	432,1	432,0666667	0,205480467
74,9	464,1	463,5	463,7	463,7666667	0,249443826
80	495,9	495,2	495,4	495,5	0,294392029
84,71	524,6	524,5	524,4	524,5	0,081649658
89,8	557,4	557,4	557,1	557,3	0,141421356
94,9	594,1	595,2	593,7	594,3333333	0,63420992
100	627,4	627,8	627,6	627,6	0,163299316
Area [mm²]	0,43				
	Dose [mW/mm²]	Dose [mW/mm²]	Dose [mW/mm²]	Mean	Std
	0,862325581	0,862093023	0,862325581	0,862248062	0,000109629
	0,930930233	0,930465116	0,930465116	0,930620155	0,000219258
	1,005348837	1,004186047	1,004883721	1,004806202	0,000477862
	1,079302326	1,077906977	1,078372093	1,078527132	0,000580102
	1,153255814	1,151627907	1,152093023	1,152325581	0,000684633
	1,22	1,219767442	1,219534884	1,219767442	0,000189883
	1,29627907	1,29627907	1,295581395	1,296046512	0,000328887
	1,381627907	1,384186047	1,380697674	1,382170543	0,001474907
	1,459069767	1,46	1,459534884	1,459534884	0,000379766
What is needed? [mJ/cm²]	110				
		Intensity [%]	Time [s]	Dose [mJ/cm²]	Std
		60	1,275734964	110	0,01398575
		64,71	1,182007497	110	0,02591645
		69,8	1,094738466	110	0,052313342
		74,9	1,019909437	110	0,059165142
		80	0,954591322	110	0,065354436
		84,71	0,901811249	110	0,017123856
		89,8	0,848734972	110	0,027913779
		94,9	0,795849692	110	0,117380411
		100	0,753664755	110	0,028621614